WestVirginiaUniversity
THE RESEARCH REPOSITORY @ WVU

Graduate Theses, Dissertations, and Problem Reports

2010

Conceptual and Preliminary Design of a Stowable Ruggedized Micro Air Vehicle

Shanti D. Hamburg
West Virginia University

Follow this and additional works at: https://researchrepository.wvu.edu/etd

Recommended Citation

Hamburg, Shanti D., "Conceptual and Preliminary Design of a Stowable Ruggedized Micro Air Vehicle" (2010). *Graduate Theses, Dissertations, and Problem Reports*. 4600.
https://researchrepository.wvu.edu/etd/4600

This Thesis is protected by copyright and/or related rights. It has been brought to you by the The Research Repository @ WVU with permission from the rights-holder(s). You are free to use this Thesis in any way that is permitted by the copyright and related rights legislation that applies to your use. For other uses you must obtain permission from the rights-holder(s) directly, unless additional rights are indicated by a Creative Commons license in the record and/ or on the work itself. This Thesis has been accepted for inclusion in WVU Graduate Theses, Dissertations, and Problem Reports collection by an authorized administrator of The Research Repository @ WVU. For more information, please contact researchrepository@mail.wvu.edu.

Conceptual and Preliminary Design of a Stowable Ruggedized Micro Air Vehicle

Shanti D. Hamburg

Thesis submitted to the
College of Engineering and Mineral Resources
at West Virginia University
in partial fulfillment of the requirements for the degree of

Master of Science
In
Aerospace Engineering

Wade W. Huebsch, Ph.D., Chair
Mridul Gautam, Ph.D.
John M. Kuhlman, Ph.D.

Department of Mechanical and Aerospace Engineering

Morgantown, West Virginia
2010

Keywords: Micro Air Vehicle; Unmanned Air Vehicle; Low Reynolds Number Flight; Stowable Aircraft; Numerical Simulation; Aircraft Design; Fluent; Gambit; TGrid; Computational Fluid Dynamics

Copyright 2010 Shanti D. Hamburg

Abstract

Conceptual and Preliminary Design of a Stowable Ruggedized Micro Air Vehicle

Shanti D. Hamburg

This study presents both feasibility and preliminary design studies of a ruggedized, stowable, ballistically launched Micro Air Vehicle (MAV). A vehicle capable of being stored within a 40 *mm* diameter, 133 *mm* long cylinder and able to withstand a significantly rough environment when stowed was desired. Minimum performance specifications were a 20% range increase from a 450 *m* range, 45^o launch angle ballistic trajectory and a gliding time of 30 *s* from the apex of said trajectory. To this end, a study of comparable MAV systems, available control and communication electronics, low Reynolds number flight, ballistic flight, and advanced projectiles was conducted. It was found that the concept was possible using current electronics, however, these would require a large majority of the available volume necessitating the novel, compact, wing stowage systems discussed within. While aerodynamically feasible the transition between ballistic and aircraft flight will necessitate significant sensor and control logic design. The small scales of this project necessitated consideration of the vagaries of low Reynolds number flight. Despite the final design proposals maintaining chordwise Reynolds numbers greater than 100,000 several key trends were found to be significantly different than those encountered in classical aerodynamic theory; particularly the existence of an optimum aspect ratio for maximum lift to drag ratio of the wing alone. For a fixed wing area and velocity increasing the aspect ratio, thereby reducing induced drag, also reduced the chordwise Reynolds number which reduced the efficiency of the airfoil. At the optimum benefits from reducing induced drag balanced with the penalties of reduced airfoil performance. The feasibility study focused primarily on volumetric concerns; minimizing stowed wing volume was the main goal. Several design iterations were constructed in SolidWorks prior to the development of two concepts ready for prototyping and testing. Design optimization was performed with both classical semi-empirical methods using Missile DATCOM and a custom in-house Matlab code as well as the Fluent CFD package. Significant work was done to find a suite of solver settings and mesh generation parameters capable of predicting 2D and 3D low Reynolds number airfoil performance with sufficient quality for preliminary design work. Optimization studies found that achieving both initial performance goals with a single aircraft would be highly inefficient. This effort concluded with a pair of designs, one high-speed cruise-to-target version capable of 700 *m* range and 9 *s* gliding time optimized for rapid-response, and a long-endurance glider with a flight time greater than 60 *s* optimized for surveillance purposes.

Acknowledgements

To my mother and father for giving me the freedom, confidence, and encouragement to follow and begin to fulfill my childhood dream. To both of you and Aunt Diane for supporting my hobbies and harebrained schemes, and for being there when things did not go as planned.

To my brother for keeping me grounded. Seriously, thank you for "Design-Build-Crash & Burn".

To Doctors John Loth and Richard Guiler for their advice and support in Design/Build/Fly. Thank you both for the opportunity to learn so much of design, management, and responsibility.

To my committee, Dr. Mridul Gautam, Dr. John Kuhlman, and especially Dr. Wade Huebsch for the incredible confidence and trust that was placed in me. New masters students do not often get the opportunity to lay the groundwork for such an important project.

Sincerely;

Shanti D. Hamburg

Table of Contents

Abstract ..... **ii**
Acknowledgements ..... **iii**
List of Figures ..... **v**
List of Tables ..... **ix**
Chapter 1 Problem Statement **1**
1.1 Problem Description 1
1.2 Solution and Overview of Work 2
Chapter 2 Mission Description and Prior Art **4**
2.1 Current Man-Portable UAVs and MAVs 4
2.2 MAV Electronics 7
2.3 Low Reynolds Number Aerodynamics 11
2.3.1 Two Dimensional Flow: Separation Bubbles and Transition *12*
2.3.2 Three Dimensional Low Aspect Ratio Aerodynamics *14*
2.4 Ballistics 16
2.5 Thesis Outline 17
Chapter 3 Concept Development **19**
3.1 Structural Concept Modeling 19
3.1.1 Cargo Stowage Concepts *22*
3.1.2 Wrapped Membrane Structure Detail *25*
3.1.3 Transformer Stowage Concepts *30*
3.1.4 Leaf Spring Structure Detail *34*
3.2 Control Surface Actuation Concepts 37
3.2.1 Torsion Rod System *37*
3.2.2 Collapsible Flapped Surface *38*
3.3 De-Spin and Orientation Methods 39
Chapter 4 Initial Surface Sizing Calculations **43**
Chapter 5 Preliminary CFD Analysis **47**
5.1 Stowed Geometry Mesh Generation 47
5.2 Deployed Configuration Simulation 50
Chapter 6 Classical Aerodynamic Optimization Analysis **52**
Chapter 7 Component CFD Analysis **59**
7.1 Fuselage Analysis 59
7.2 Two Dimensional Low Reynolds Number Airfoil Analysis 61
7.2.1 NACA 0009 Validation *64*
7.2.2 Two Dimensional Airfoil Comparison *75*
7.3 Preliminary Three Dimensional Main Wing Analysis 79
Chapter 8 Recommended Preliminary Designs **85**
8.1 High Speed Cruise Configuration 85
8.2 Long Endurance Configuration 88
Chapter 9 Summary and Recommendations **92**
References **95**
Appendix A Missile DATCOM Input and Output Files **97**
Appendix B Grid Generation Details **102**
Appendix C Analysis Program Code **105**
Appendix D Fluent Configuration Details **120**
Appendix E Curriculum Vitae **123**

List of Figures

Figure 1-1: Stowed Configuration Geometry 1
Figure 1-2: Ballistic Launch Trajectory with Minimum Range Increase Specified 2
Figure 2-1: Collage of Current UAV and MAVs, Number and Sources as Listed in Table 2-1 5
Figure 2-2: Flight Mass Plotted Versus Main Wing Span 6
Figure 2-3: Cruise Velocity Plotted Versus Main Wing Span 6
Figure 2-4: Image from 100 *m* Altitude at 45^{o} Angle from Aircraft, 40^{o}x40^{o} Field of View, 1,000x1,000 Pixel Camera(Davis, Kosicki, Boroson, & Kostishack, 1996) 7
Figure 2-5: Effect of Pitch Oscillation on Camera View (Morris, Design of Micro Air Vehicles and Flight Test Validation, 2000) 8
Figure 2-6: Twin Camera System from AeroVironment's Wasp MAV(Grabowsky, 2007) 8
Figure 2-7: 20 *cm* Trochoid Planform MAV from MLB Company (Morris, Design of Micro Air Vehicles and Flight Test Validation, 2000) 9
Figure 2-8: Micro Video Camera and Transmitter (Torres & Mueller, 2001) 9
Figure 2-9: Circuitry Required for Optical Flow Velocity and Altitude Measurement System (Ruffier, Viollet, Amic, & Franeschini, 2003) 10
Figure 2-10: Paparazzi MAV Autopilot System 10
Figure 2-11: Ground Stations for MLB Bat MAV System (Morris, Design of Micro Air Vehicles and Flight Test Validation, 2000) 11
Figure 2-12: Reduction in Smooth Airfoil Performance with Falling Reynolds Number (Lissman, 1983) 12
Figure 2-13: Schematic of Low Re Separation Bubble Transition (Roberts, 1980) 12
Figure 2-14: Hysteresis Behavior of a Wing at Low Reynolds Number (Simons, 1999) 13
Figure 2-15: Drag Polars of an Eppler E374 Airfoil at Low Reynolds Numbers (Shyy, Lian, Tang, Viieru, & Liu, 2008) 14
Figure 2-16: Lift Coefficient Versus Angle of Attack for Low Aspect Ratio Rectangular Planforms at Re=10^{5} (Mueller, Torres, & Srull, Elements of Aerodynamics, Propulsion, and Design, 2006) .. 15
Figure 2-17: Characteristic Gyroscopically Stabilized Body Showing CG Location and Axis for Polar and Transverse Moments of Inertia 16
Figure 2-18: Increasing Dispersion and Developing Instability of a Slowly De-Spinning Round (Carlucci & Jacobson, 2008) 17
Figure 3-1: Cargo Type Design: Draper Lab's Flyer (Martorana, et al., 2003) 19
Figure 3-2: Design Progression of WVU Cargo Work and Opening Sequence 20
Figure 3-3: Transformer Type Sonotube, Missile Tube, and Naval Gun Designs (Woodland, 2000) (Bourlett, 1997) (Palmer, 2001) 20
Figure 3-4: WVU Transformer Design Progression and Transformer Deployment Process 21
Figure 3-5: Membrane Wings Concepts, a) WVU Wrapped, b) WVU Leaf Spring, c) Batten Reinforced (Stanford, Abdulrahim, Lind, & Ifju, 2007), d) Titanium-Mylar Insect Scale (Pornsin-sirirak, Tai, & Ho, 2001), e) Small Scale Batten Reinforced (Fleming, Bartram, Waszak, & Jenkins, 2001) . 21
Figure 3-6: Initial Switchblade Concept 22
Figure 3-7: Deploy Process for Wrapped Solid Wing Cargo Designs 23
Figure 3-8: Solid Wrapped Wing Design Progression 23
Figure 3-9: Wrapped Membrane Wing Concept 24
Figure 3-10: Cambered Plate MAV With Wrappable Wings (Shyy, Ifju, & Vieru, Membrane Wing-based Micro Air Vehicles, 2005) 25
Figure 3-11: Slot For Inner Wrapped Wing Pass-Through 26
Figure 3-12: Inflatable or Expandable Lower Surface Profile on Membrane Wing 26
Figure 3-13: Batten Reinforcement and Adaptive Washout Detail (Stanford, Abdulrahim, Lind, & Ifju, 2007), (Ifju, Ettinger, Jenkins, & Martinez, 2001) 27
Figure 3-14: "Feathered" Wing Morphing System for WVU Horten Flying Wing (Guiler, 2007) 28

Figure 3-15: Potential Biomemetic Membrane Wing Configuration Diversity (Sachs, 2007) 29
Figure 3-16: Correlation Mass and Required Yaw Stability with Behavior of a Clean Swept Biomemetic Planform(Sachs, 2007) 29
Figure 3-17: Sponsor Telescopic Transformer Concept, (dimensions in *cm*) 30
Figure 3-18: Switchblade Transformer Structural Concept, (dimensions in *mm*) 31
Figure 3-19: Telescopic Transformer Structural Concept, (dimensions in *mm*) 32
Figure 3-20: Leaf Spring Transformer Structural Concept 33
Figure 3-21: Inverse Relationship Between Span and Tip Chord Length of Leaf Spring Structure for Wings with Equal Length Leading Edge Leaves 34
Figure 3-22: Method for Varying Leaf Spring Angle of Attack Relative to Fuselage; Gray) Fuselage With Slot for Membrane and Leaves, Blue) Rotating Mount for Leaves, Yellow) Leaf Spring Elements, Tan) Membrane Bonded to Leaf Upper and Lower Surfaces 35
Figure 3-23: Rotated Leaves for Control Surface Actuation and Camber Modifications; Fixed Leaves and Fuselage (Gray), Outboard Surface Rotation Point and Leaves (Red), Inboard Rotation Point and Leaves (Blue) 35
Figure 3-24: Staged Wing Deployment for Stabilization and De-spin; Red) Initial Deployment for De-spin and Orientation, Blue) Secondary Deployment of Main Wings 36
Figure 3-25: Illustration of Bounding Flight for Increased Cruising Speed (Morris, Design and Flight Test Results for Micro-Sized Fixed-Wing and VTOL Aircraft, 1997) 36
Figure 3-26: Torsion Rod Control System on Batten Reinforced Wing, Multiple Actuation Point Configuration (Stanford, Abdulrahim, Lind, & Ifju, 2007) 37
Figure 3-27: Effective Flapped Control Surface for Membrane Wings; Black) Carbon Laminate Structure, Tan) Membrane Surface, Dark Gray) Rigid Elements Bonded to Membrane, Light Gray) Control Horns and Cables for Pull-Pull Control 38
Figure 3-28: Instability and Dispersion Caused by Slowly Decreasing Spin Rate(Carlucci & Jacobson, 2008) 39
Figure 3-29: Paparazzi Autopilot Infrared Aerodynamic Angle Sensor System for Spin Orientation (Krashanitsa, Platanits, & Silin, 2006) 40
Figure 3-30: Cruciform Planform and Tri Planforms for Active Control Surface De-spin 40
Figure 3-31: Multi-Stage Fin Deployment Schematic; a) Stabilizer Fins Deploy Further as Lifting Surfaces, b) Additional Lifting Surface Deploy, c) Stabilizers Deploy, De-Spin, and Discard Prior to Main Wing Deploy 41
Figure 3-32: Casing Ejection in Spin Direction with High Rotation Rate to Reduce MAV Rotation Rate 42
Figure 4-1: Fuselage and Tail Configuration Studied with MDCOM, Dimensions in *mm* 44
Figure 4-2: Tail Sizing Sensitivity Study with Three CG Locations 45
Figure 4-3: Complete Planform Studied with MDCOM, Dimensions in *mm* 45
Figure 4-4: Main Wing Sizing Sensitivity Study 46
Figure 5-1: Stowed Geometry 47
Figure 5-2: Solution Domain, Sliced on Longitudinal Centerline 49
Figure 5-3: Convergence Plot for Stowed Geometry, Mesh Converged at $2.7x10^6$ Cells 49
Figure 5-4: Initial Deployed Geometry Surface Meshes, Identical Vertical Tail Area and Main Wing Area, Identical Fuselages 50
Figure 5-5: Comparison of Flow at Tails of Conventional and Delta Planforms, Pathlines Colored by Velocity, (*m/s*), Jagged Black Lines Are Artifacts From Geometry Contour Display 51
Figure 6-1: Effect of Varying Launch Angle for AR = 2 Wing on Cruise Velocity and Initial Gliding Altitude 53
Figure 6-2: Optimization Code Flowchart 54
Figure 6-3: Comparison of High Speed, Low Angle Launch and Low Speed, High Angle Launch Missions 55
Figure 6-4: Comparison of Alternate Mission Plan Required Wing Areas, Dimensions in *mm* 56

Figure 6-5: Comparison of Required Wing Area for High-Speed Cruise (Wing Loading (*W/S*) = 700 N/m^2, V_{cr} = 48 *m/s*, *S* = 2,523 mm^2) and Long Endurance Missions (Wing Loading (*W/S*) = 150 N/m^2, V_{cr} = 20 *m/s*, *S* = 11,772 mm^2) Relative to Stowed Geometry 56
Figure 6-6: Comparison of WVU Stowable UAV Flight Regimes for High-Speed and Long-Endurance Missions to Current UAV and MAV aircraft 57
Figure 6-7: Lift-to-drag Ratio Sensitivity to Fuselage Drag Coefficient 58
Figure 7-1: Various Ogive Tail Cones Applied to Stowed Geometry for Fuselage Study, Dimensions in *mm* 59
Figure 7-2: Mesh Independence Study for 45 *mm* Center Body Fuselage 60
Figure 7-3: Component Mesh For Fuselage Analysis, 45 *mm* Center Body 60
Figure 7-4: Correlation Between Fuselage Volume and Fuselage Drag Coefficient, Stowed Geometry is Far Right Value, Length of Tail Cone Increases to Left 61
Figure 7-5: Smoke Visualization of Transition Bubble on a Smooth Airfoil at Re - 40,000 (Mueller & Batill, 1982) 62
Figure 7-6: Turbulent Boundary Layer Measurements at Reynolds Numbers Under $0.5x10^5$, Airfoil Chord = 180 *mm*, $\alpha=3^o$ (Kim, Yang, Chang, & Chung, 2009) 63
Figure 7-7: Comparison Between y+>30 Mesh Results and Experimental Data for a NACA 0009 Airfoil at $Re=1.5x10^5$. NACA 0009 Experimental Data, (Selig, Donovan, & Fraser, 1989) 64
Figure 7-8: Mesh Regions for 2D Airfoil Studies, Labels as in Table 7-1 65
Figure 7-9: Lift and Drag Coefficient Plot Showing Mesh Independence for NACA 0009 2D Airfoil, Standard k-ω Turbulence Model 66
Figure 7-10: Comparison of Blunt and Sharp Trailing Edge Mesh Geometries, Dimensions in *m* 67
Figure 7-11: Comparison of Blunt and Sharp Trailing Edge Mesh Results, Standard k-ω Turbulence Model 68
Figure 7-12: Lift-to-drag Ratios for Selected Turbulence Models at a Reynolds Number of $3x10^5$ 70
Figure 7-13: Lift-to-drag Ratios for Final Turbulence Model Down-Select at Reynolds Number of $0.6x10^5$ 70
Figure 7-14: Drag Polar Using K-ω SST Turbulence Model for a NACA 0009 at a Reynolds Number of $3.0x10^5$, Markers at 2^o α Increments from 0^o 71
Figure 7-15: Drag Polar Using K-ω SST Turbulence Model for a NACA 0009 at a Reynolds Number of $1.5x10^5$, Markers at 2^o α Increments from 0^o 72
Figure 7-16: Drag Polar Using K-ω SST Turbulence Model for a NACA 0009 at a Reynolds Number of $1.0x10^5$, Markers at 2^o α Increments from 0^o 72
Figure 7-17: Drag Polar Using K-ω SST Turbulence Model for a NACA 0009 at a Reynolds Number of $0.6x10^5$, Markers at 2^o α Increments from 0^o 73
Figure 7-18: Velocity Pathlines (*m/s*) Showing Prediction of Recirculating Separation Bubble, 6^o α, $Re=0.6x10^5$ 74
Figure 7-19: Pressure Coefficient Around NACA 0009 Showing Separation Bubble "plateau", 6^o α, $Re=0.6x10^5$ 74
Figure 7-20: MA 409 Drag Polar with Experimental and CFD Data 76
Figure 7-21: S 2048Drag Polar with Experimental and CFD Data 76
Figure 7-22: DF 102 Drag Polar with Experimental and CFD Data 77
Figure 7-23: NACA 0009 Drag Polar with Experimental and CFD Data 77
Figure 7-24: S 3010 Drag Polar with Experimental and CFD Data 78
Figure 7-25: MH 22 Drag Polar 78
Figure 7-26: S 5020 Drag Polar 79
Figure 7-27: Surface and Centerline Volume Mesh for Initial 3D Wing Modeling 80
Figure 7-28: Mesh Independence Plot for Initial 3D Wing Modeling 80
Figure 7-29: Pathlines Colored by Velocity (*m/s*) Around Reference Wing (Angle of Attack = 4^o) 81
Figure 7-30: Inverse Correlation Between Aspect Ratio and Lift-to-drag Ratio and Direct Correlation Between Lift-to-drag Ratio and Mean Aerodynamic Chord Reynolds Number 82

Figure 7-31: Lift-to-drag Ratio Improving Towards Optimum As Wing Loading Increases in Initial Study 83
Figure 7-32: Lift-to-drag Ratio Insensitive to Leading Edge Sweep Angle 84
Figure 7-33: Inverse Correlation Between Taper Ratio and Lift-to-drag Ratio 84
Figure 8-1: Flow Chart of Proposed Optimization Process 85
Figure 8-2: High Speed To Target Configuration, (dimensions in *mm*) 86
Figure 8-3: High Speed Cruise Mission Profile 86
Figure 8-4: High Speed Leaf Spring Structure Concept, Partially Deployed (Left) and Fully Deployed (Right) 87
Figure 8-5: High Speed Membrane Wing Structure Concept, Partially Deployed (Left) and Fully Deployed (Right) 87
Figure 8-6: Long Endurance Concept, Dimensions in mm 89
Figure 8-7: Long Endurance Configuration Leaf Spring Structure, Top Left Front Quarter (Left), Bottom Right Rear Quarter (Right) 89
Figure 8-8: Long Endurance Configuration Wrapped Membrane Structure 90
Figure 8-9: Schematic of Long Endurance Mission Profile 91

List of Tables

Table 2-1: Collected UAV and MAV System Data 4
Table 2-2: Thesis Outline Summary 18
Table 5-1: Sponsor Recommended Solver Settings and Domain Sizes With WVU Selected Solver Settings 48
Table 6-1: Given Stowed Trajectory Data and Calculated Launch Velocity 52
Table 6-2: Results of Optimization Code for an Array of Launch Angles 54
Table 7-1 Mesh Region Specifications for Figure 7-8, C=Chord Length, 0.1 *m* for this Study 65
Table 7-2: Summary of Fluent 12 Turbulence Models Applied to NACA 0009 at 6^{o} Angle of Attack and Reynolds Number of $3x10^{5}$, Errors Less than 10% Highlighted in Green 69
Table 7-3: Selected Airfoil Profiles and Details 75
Table 7-4: Flow Parameters, Lift Coefficient, and Geometric Parameters Varied for Three Dimensional Planform Study 81
Table 8-1: Sizes and Expected Performance of High Speed MAV 88
Table 8-2: Sizes and Expected Performance of Long Endurance MAV 91

Chapter 1 Problem Statement

1.1 Problem Description

A micro aerial vehicle (MAV) was to be deployed from a compact, rugged, stowed configuration. This aircraft was intended to launch on a ballistic trajectory in a cylindrical stowed configuration and deploy aerodynamic surfaces to increase range and provide maneuvering and guidance capability. This document discusses the conceptual and preliminary design, paying particular attention to the problems created by the transition between ballistic and aircraft flight. The proposed size of the stowed configuration imposed significant geometric constraints that required a thorough modeling process and forced the design into unusual flight regimes.

The stowed configuration was specified as a 40 *mm* diameter cylindrical body with a hemispherical nose 133 *mm* in total length, as shown in Figure 1-1. The center of gravity was fixed at 50% along the body length in the stowed configuration. Launch conditions were specified as a ballistic trajectory with 450*m* range on the ballistic arc with a 40*m/s* apex velocity at a launch angle of 45^o (Figure 1-2). A minimum 20% range increase was specified, as well as a fight mass of 180*g*. Note that the flight profiles sketched in Figure 1-2 are for illustration only and do not represent the actual profile. In reality the flight plan would form a ballistic arc up to apex and a straight-line gliding decent afterwards.

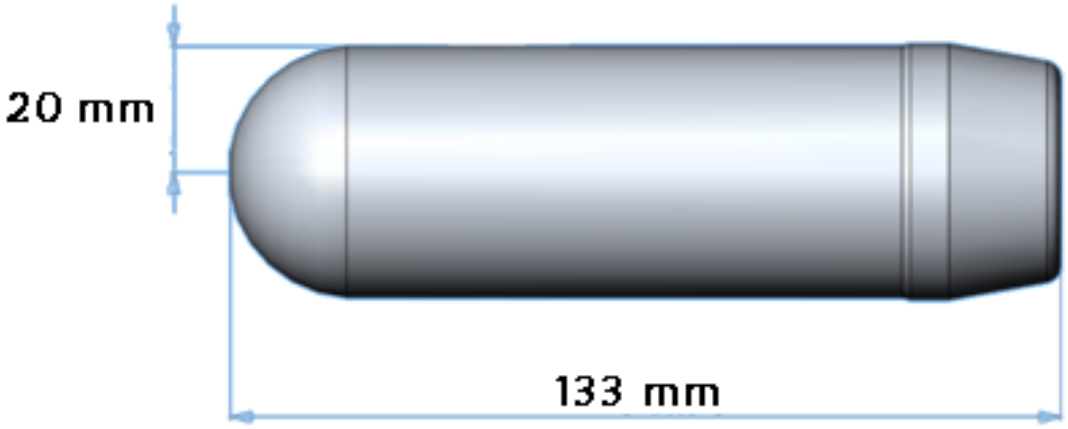

Figure 1-1: Stowed Configuration Geometry

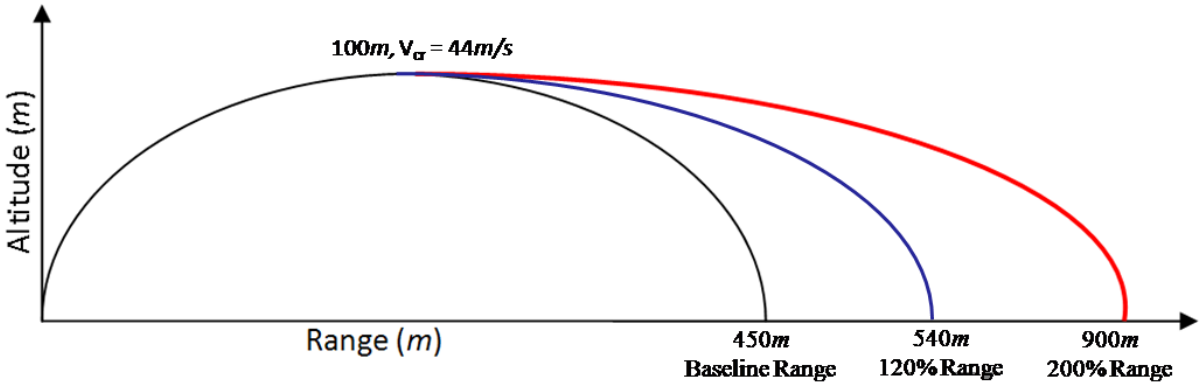

Figure 1-2: Ballistic Launch Trajectory with Minimum Range Increase Specified

Concepts for lifting and stabilizing surface planforms as well as stowable structures were required. The primary goal was to prove the aerodynamic feasibility of this stowed MAV concept. This included preliminary recommendation on lifting and stabilizing surface sizing and location for acceptable gliding range and stable flight. Proving volumetric feasibility was also a major consideration. Stowed aerodynamic surfaces had to leave sufficient volume for future sensor, control, and payload systems.

Due to International Traffic in Arms Regulations and other security considerations some work done on this project has been omitted from this document. These omissions do not seriously impact the new information presented here as they deal with a specific application rather than the general preliminary design work which is the primary focus of this document.

1.2 Solution and Overview of Work

Few options exist to extend the range of an object on a ballistic trajectory. Drag can be reduced by modifying external geometry, but work in this document will show that body drag can only be reduced by approximately 1/3 at a significant loss of useful volume. The most effective way to extend the range of a ballistic object was to increase its lift-to-drag ratio by the addition of lifting surfaces. This placed concept development in the region between ballistics and micro aerial vehicle design.

Design work began with brainstorming stowable wing structure concepts. Development of these concepts provided maximum area and extreme fore and aft location limits for the wings and tails. A semi-empirical code was used to generate first-cut wing and tail sizes within these limits. According to these semi-empirical methods performance goals were surprisingly easy to meet.

With initial sizing completed the stowed geometry was simulated in Fluent to verify prediction capability and develop flexible, accurate solution settings. Two basic deployed planforms were then studied, a high aspect ratio conventional design, and a clipped-delta layout. At the low Reynolds numbers of this flight regime the clipped delta wing had twice the lift-to-drag ratio of the conventional layout. With such a clear and significant result all work was then focused on optimizing a delta, or other low aspect ratio, configuration.

Classical aerodynamic analysis methods were applied again in an optimization analysis of the main wing and launch angle. As expected, optimum wing loading varied significantly with the apex/cruise velocity. This led to two divergent designs; one focused on the specified range increase, the other on a longer, slower flight better suited to a surveillance mission. Long endurance missions required a wing area in the neighborhood of 10,000 mm^2 while the extended range mission only required 2,500 mm^2.

A numerical study of airfoils and planforms at low Reynolds numbers was then conducted to check classical theory predictions and converge on optimums. This led to the two final designs; a high wing-loading, high-speed, range-extended version, and a low-speed, long-endurance reconnaissance design.

Chapter 2 Mission Description and Prior Art

The project required combining the field of MAV design with basic ballistics as well as a preliminary study of available miniaturized electronics. While the deployed configuration is meant to function purely as a MAV with all associated ground equipment the launch concept required some basic knowledge of gyroscopically stabilized flight. Blending these two flight regimes necessitated a study of current unmanned aerial vehicles, micro air vehicles, gyroscopically stabilized ballistics, advanced projectiles, miniaturized electronics, and low speed aerodynamics.

2.1 Current Man-Portable UAVs and MAVs

A survey of current MAV and small UAV systems was conducted. Data collected included mass, size, velocity, and ground station type information. Table 2-1 presents this data and Figure 2-1 shows a collage of the vehicles. Unfortunately complete information was not available for all aircraft. Wing loadings would have been the preferred point of comparison rather than wing span and flight mass. Unfortunately wing area data was not available for the majority of the comparable aircraft.

Table 2-1: Collected UAV and MAV System Data

	Designation	Classification	Wing Span (*m*)	Maximum Mass (*kg*)	Cruise Speed (*m/s*)	Source
1	**MLB 15 *cm* Trochoid**	MAV[1]	0.150		13.400	Design of MAVs (MLB Co.)
2	**University of Floridia MAV**	MAV	0.152	0.055	11.170	Composite Materials for MAVs
3	**Black Widow**	MAV	0.152	0.050	12.630	defense-update.com
4	**MLB 20 *cm* Trochoid**	MAV	0.200		13.400	Design of MAVs (MLB Co.)
5	**Mosquito**	MAV	0.300	0.250	16.450	defense-update.com
6	**NRL MITE 2**	MAV	0.368	0.213	13.400	The NRL MITE Air Vehicle
7	**MLB Bat**	MPUAV[2]	0.600		13.400	Design of MAVs (MLB Co.)
8	**Wasp Block III**	MPUAV	0.723	6.530	13.410	USAF Fact Sheet
9	**BirdEye 100**	MPUAV	0.850	1.300		Israeli Aerospace Industries
10	**RQ-14B Dragon Eyes**	MPUAV	1.100	2.800	9.719	defense-update.com
11	**Desert Hawk**	MPUAV	1.320	3.200	16.662	defense-update.com
12	**RQ-11B Raven**	MPUAV	1.370	7.700	13.950	designation-systems.net
13	**BirdEye 500**	UAV[3]	2.000	5.000	18.000	defense-update.com
14	**Finder**	UAV	2.620	27.200	19.439	defense-update.com
15	**ScanEagle**	UAV	3.100	18.000	30.170	USAF Fact Sheet
16	**MQ-1 Predator**	UCAV[4]	14.800	1020.000	44.700	USAF Fact Sheet
17	**MP-9 Reaper**	UCAV	20.000	4750.000	102.800	USAF Fact Sheet
18	**RQ-4B Global Hawk**	HALE UAV[5]	39.800	14628.000	159.570	USAF Fact Sheet

[1] MAV: Micro Air Vehicle, [2] MPUAV: Man-Portable Air Vehicle, [3] UAV: Unmanned Air Vehicle, [4] UCAV: Unmanned Combat Air Vehicle, [5] HALE UAV: High-Altitude Long-Endurance UAV

Figure 2-1: Collage of Current UAV and MAVs, Number and Sources as Listed in Table 2-1

Plotting flight mass and cruise velocity as a function of main wing span shows surprisingly strong correlations as seen in Figure 2-2 and Figure 2-3. Note that some of the UAVs listed in Table 2-1 have been omitted from the figures for the sake of clarity. The flight wing span to flight mass correlation was very nearly linear across the entire size range, an excellent guideline for preliminary design work. Cruise velocity also displayed a strong correlation with wing span, though with more complex behavior. Velocity was seen to decrease with smaller size to a minimum of 10 *m/s*. At the very smallest sizes aircraft operated within a band between 10 *m/s* and 18 *m/s*. The lower limit was probably forced by the desire to avoid extremely low chordwise Reynolds numbers while maximum velocity was thought to be driven by mission constraints. For example, quality video reconnaissance from approximately 100 *m* altitude depends on a relatively slow moving platform [1]. Both Figure 2-2 and Figure 2-3 provide an initial estimate of the operating regime for the WVU stowable MAV (shaded red geometries) designs. Both designs were entirely outside the conventional regions. Innovative and application specific solutions were required.

[1] (Davis, Kosicki, Boroson, & Kostishack, 1996)

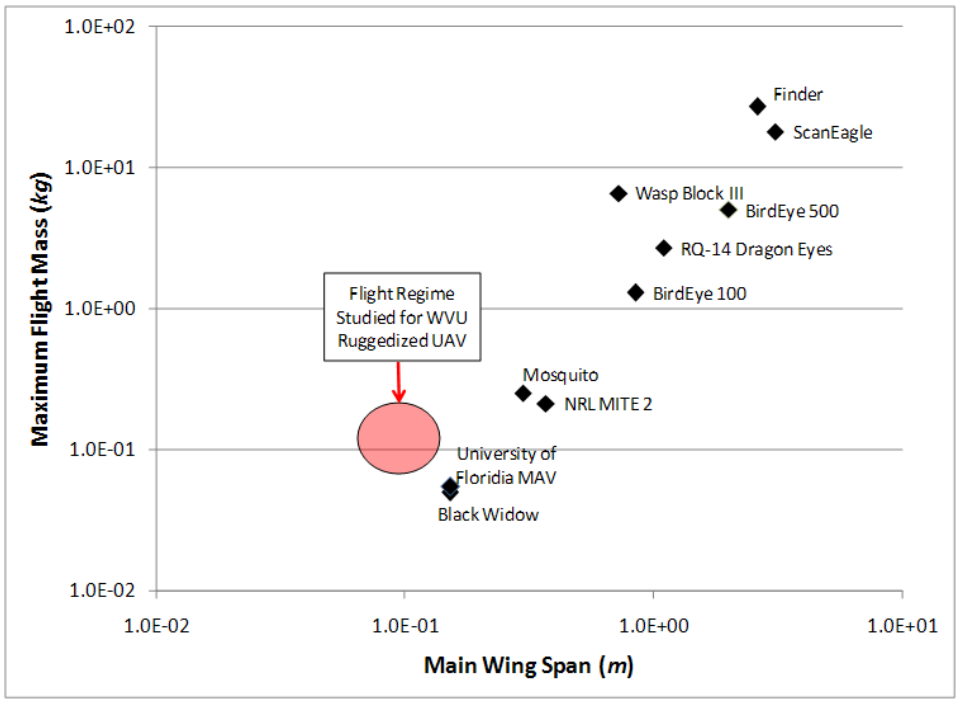

Figure 2-2: Flight Mass Plotted Versus Main Wing Span

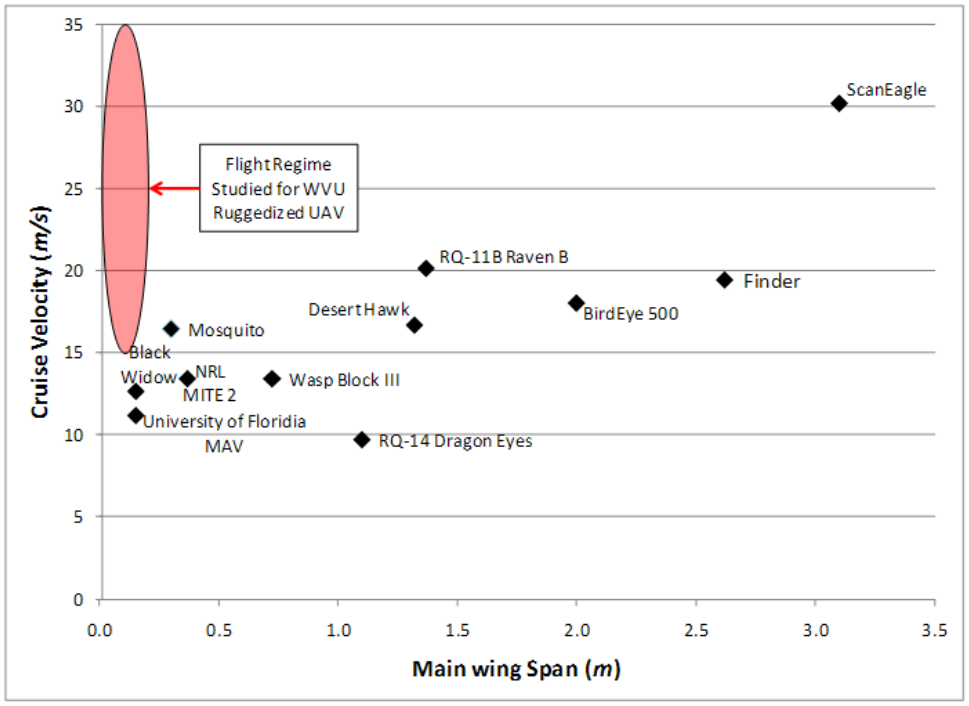

Figure 2-3: Cruise Velocity Plotted Versus Main Wing Span

2.2 MAV Electronics

This project has not yet progressed to full systems integration. However, having information on current camera, sensor, control, and communication systems available was useful when considering the practicality of structural and volumetric designs and for directing future work. Information presented here provided minimum limits and goals for available useable fuselage volume throughout the design process. This also provides a brief overview of the currently available technologies.

Figure 2-4 shows an image taken from a MAV flying at 100 *m* above ground level with the camera mounted at a 45^{o} downward angle from horizontal and a 1,000x1,000 pixel resolution and a 40x40 degree field of view. Even with images from such a high resolution micro camera, identifying intentions of personnel on the ground could be difficult. Image stabilization systems are almost required in addition to the high resolution due to the oscillations of the MAV about all axes. The effects of pitch oscillation on the camera target are shown in Figure 2-5. AeroVironment's Wasp vehicle, 72.3 *cm* span, incorporated the twin-camera system shown in Figure 2-6. Image stabilization and view steering were both incorporated by April 2007[2].

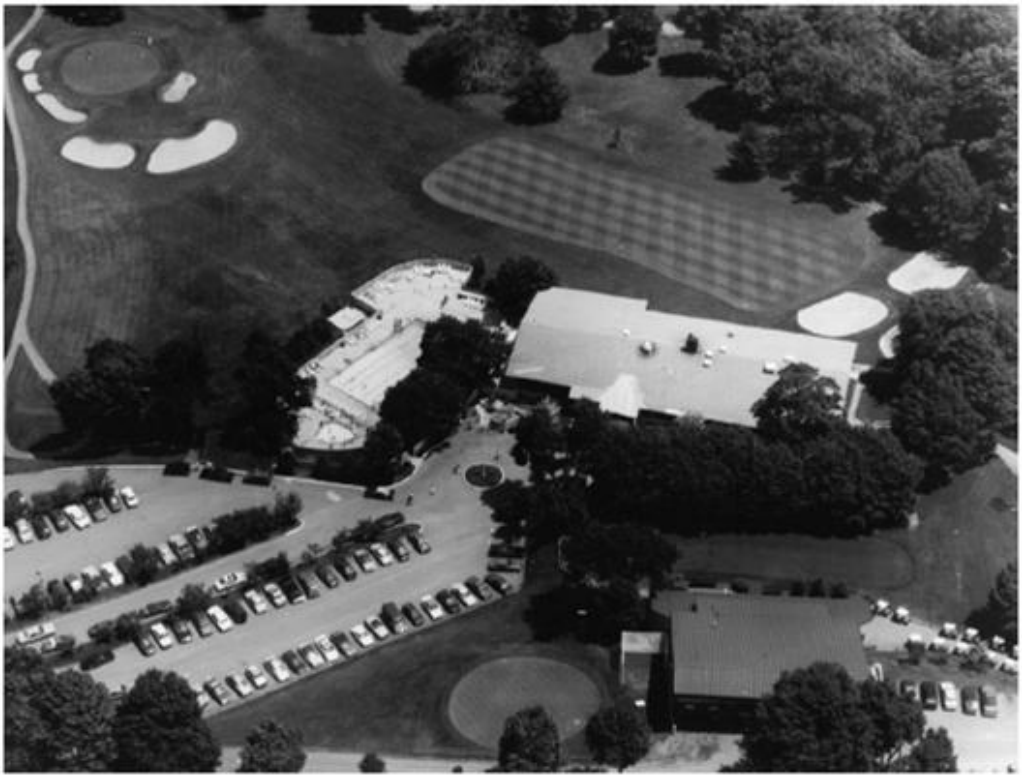

Figure 2-4: Image from 100 *m* Altitude at 45^{o} Angle from Aircraft, 40^{o}x40^{o} Field of View, 1,000x1,000 Pixel Camera(Davis, Kosicki, Boroson, & Kostishack, 1996)

[2] (Grabowsky, 2007)

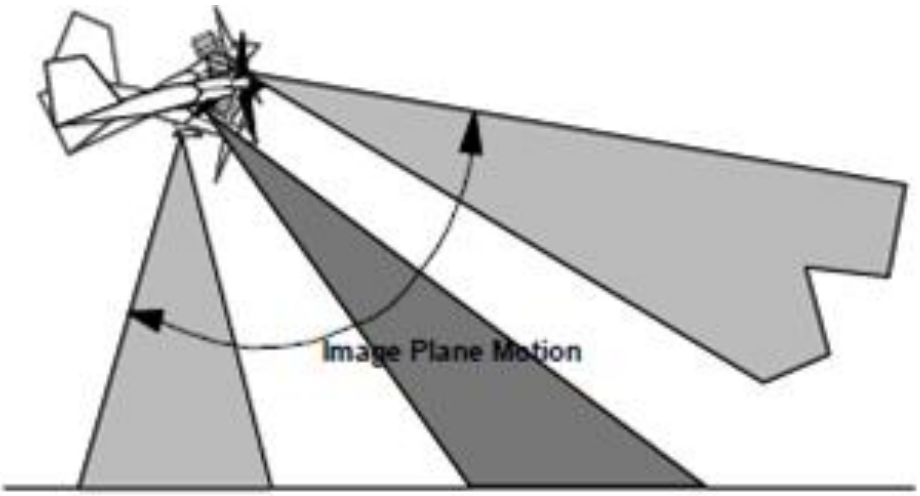

Figure 2-5: Effect of Pitch Oscillation on Camera View (Morris, Design of Micro Air Vehicles and Flight Test Validation, 2000)

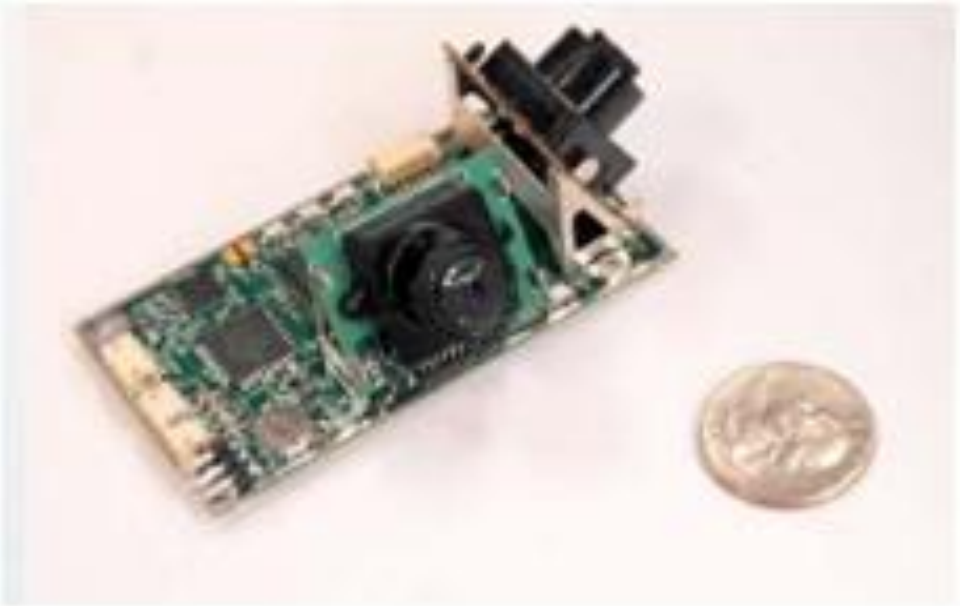

Figure 2-6: Twin Camera System from AeroVironment's Wasp MAV(Grabowsky, 2007)

Onboard electronics have been miniaturized sufficiently to make this type of project feasible. Figure 2-7 provides details of a small flying-wing MAV produced by MLB Company with major internal components visible through a transparent skin [3]. This design, developed by Morris et al., incorporated all control and communication systems in addition to propulsion. Focusing exclusively on gliding flight in the current project has freed a large amount of volume for wing stowage and more powerful transmitter systems.

[3] (Morris, Design and Flight Test Results for Micro-Sized Fixed-Wing and VTOL Aircraft, 1997)

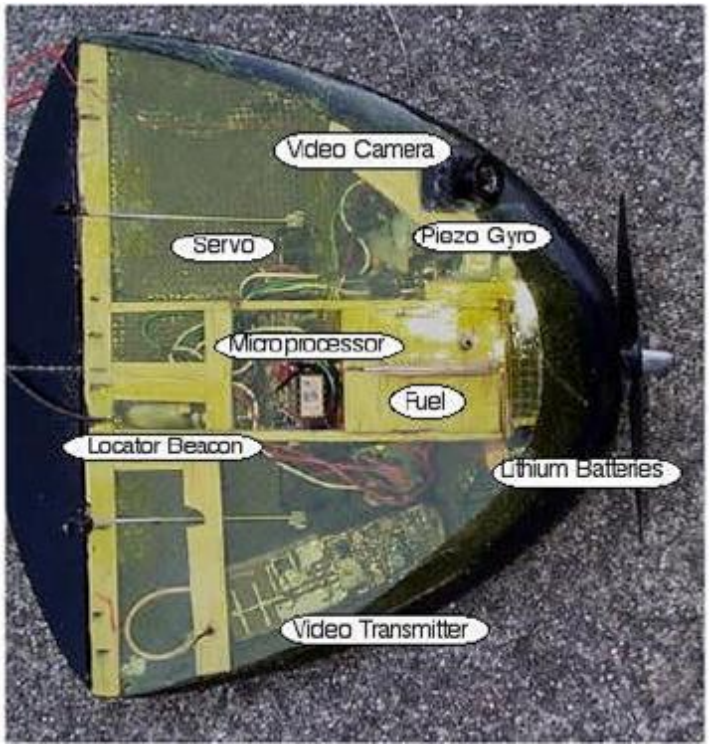

Figure 2-7: 20 *cm* Trochoid Planform MAV from MLB Company (Morris, Design of Micro Air Vehicles and Flight Test Validation, 2000)

In addition to the micro video cameras and transmitters such as those shown in Figure 2-8 several novel micro attitude sensors have been developed. An "optical flow" circuit designed by Ruffier, et al. can be used to determine both altitude and velocity. Rates of dilation and translation of separate objects in the video feed were used to collect velocity and climb rate information. The greatest advantage of this system was that it used the surveillance camera as a major component of the flight sensors and thus reduced system weight. An example is provided in Figure 2-9 [4].

Figure 2-8: Micro Video Camera and Transmitter (Torres & Mueller, 2001)

[4] (Ruffier, Viollet, Amic, & Franeschini, 2003)

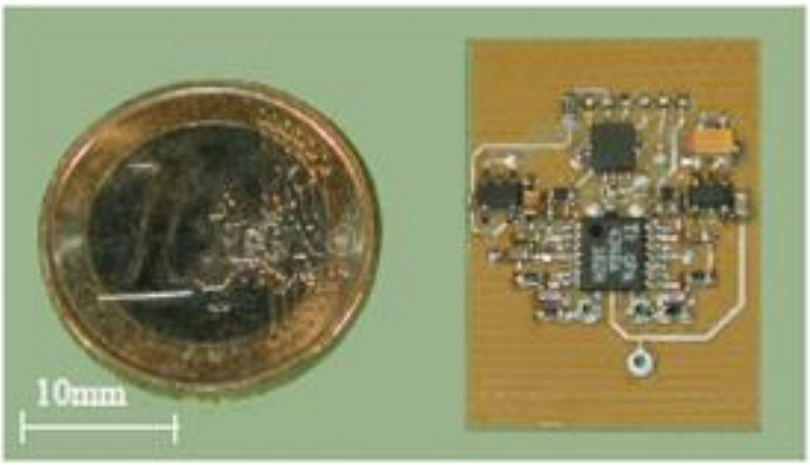

Figure 2-9: Circuitry Required for Optical Flow Velocity and Altitude Measurement System (Ruffier, Viollet, Amic, & Franeschini, 2003)

A MAV scale onboard autopilot has been created by Krashanitsa, et al., (2006) for use in the 180*g* 30 *cm* span Dragonfly MAV [5]. The Paparazzi system, shown in Figure 2-10, used a GPS receiver to obtain heading and altitude while a set of four infrared sensors collected pitch, roll, and yaw angles. The autopilot computer and sensor system weighed a mere 30*g* in 2006. Modern equipment would likely be capable of bringing this weight down even further.

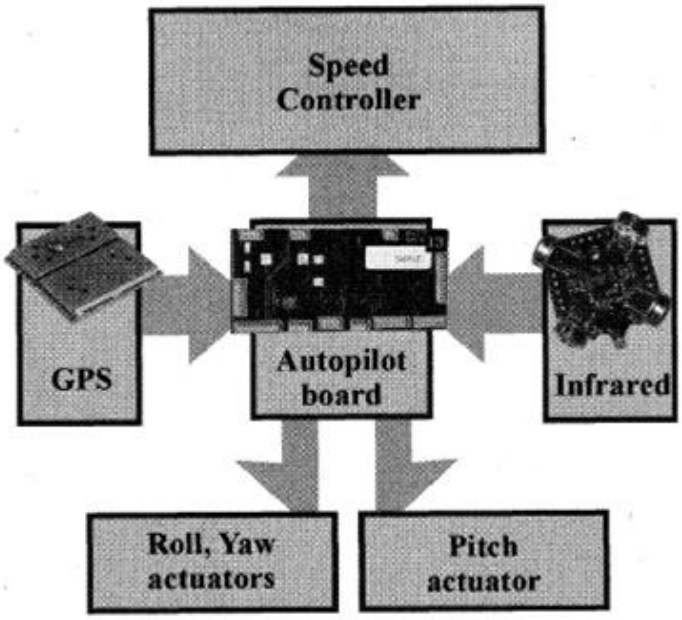

Figure 2-10: Paparazzi MAV Autopilot System

[5] (Krashanitsa, Platanits, & Silin, 2006)

Unfortunately the Achilles heel of all the small MAV/UAV designs has been the size of the ground station. Ground stations for the MLB Bat and AeroVironment's Switchblade are shown in Figure 2-11. Video display, manual controls, and high-power omnidirectional or gimbaled dish unidirectional transmitters and high-sensitivity gimbaled dish receivers have been required [6]. To achieve maximum potential the ground equipment for the current project would need to be significantly reduced in size.

Figure 2-11: Ground Stations for MLB Bat MAV System (Morris, Design of Micro Air Vehicles and Flight Test Validation, 2000)

2.3 Low Reynolds Number Aerodynamics

Initial study of the small scales and low velocities, 130 *mm* body length and 40 *m/s* maximum cruise speed, indicated that the aircraft would likely operate in a low Reynolds number (Re) regime, under 300,000 based on main wing chord. This required attention since flow behavior begins to change in significant and nonlinear manners as the Reynolds number is reduced. Such effects become more extreme as Re drops toward 75,000.

[6] (Davis, Kosicki, Boroson, & Kostishack, 1996)

2.3.1 Two Dimensional Flow: Separation Bubbles and Transition

At chordwise Re under approximately 150,000 the performance of smooth a airfoil section begins to degrade rapidly, as shown in Figure 2-12[7]. This is caused by the variable laminar/turbulent nature of the boundary layer. When operating at low angles of attack both upper and lower surfaces maintain attached laminar flow. As angle of attack increases a leading edge separation bubble forms on the upper surface and flow trips to turbulent [8]. The chordwise length of this separation bubble can vary from a few percent near the point of maximum velocity at the surface to more than 40% of the upper surface. A schematic of the transition is shown in Figure 2-13 along with approximate outlines of the upper and lower surface pressure distributions.

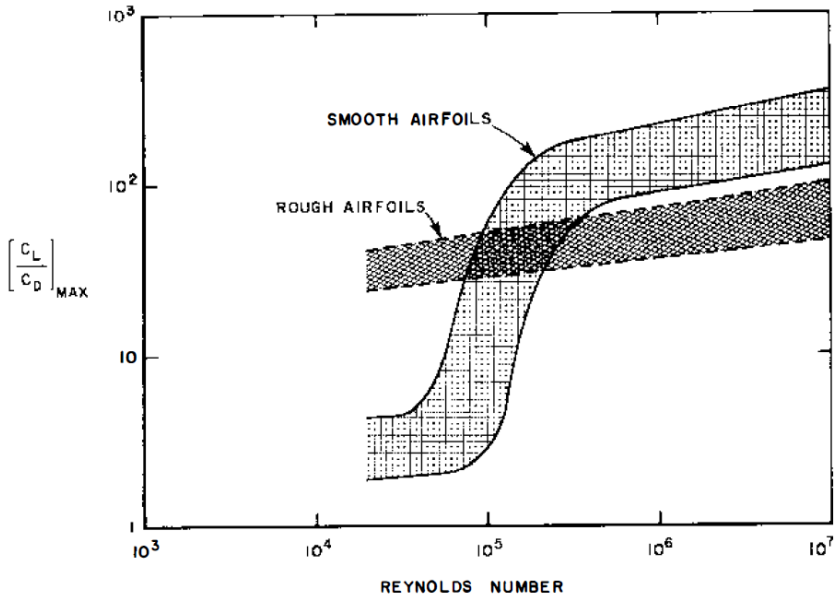

Figure 2-12: Reduction in Smooth Airfoil Performance with Falling Reynolds Number (Lissman, 1983)

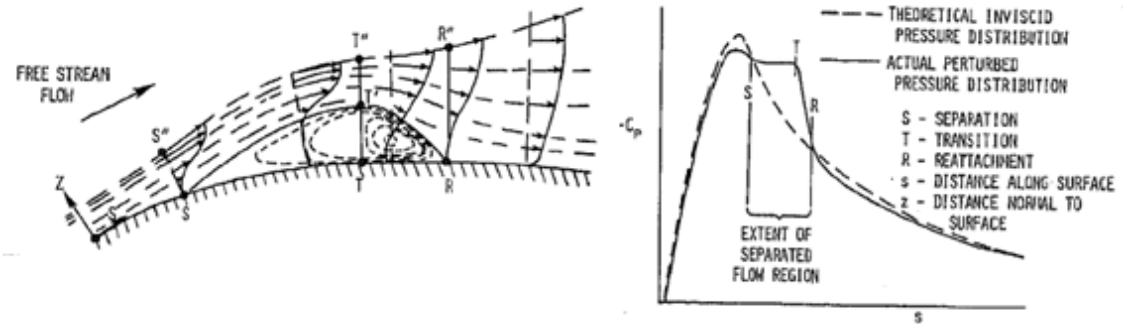

Figure 2-13: Schematic of Low Re Separation Bubble Transition (Roberts, 1980)

---

[7] (Lissman, 1983)
[8] (Mueller, Aerodynamic Measurments at Low Reynolds Numbers for Fixed Wing Micro Air Vehicles, 1999)

Hysteresis behavior is also encountered at these low Reynolds numbers [9]. Flow detaches from the wing at a high angle stall but does not re-attach until a much lower angle of attack is achieved as illustrated in Figure 2-14. This effect can make stall recovery difficult for MAVs but is fortunately uncommon for most airfoils above Reynolds numbers of 100,000 where flow reattaches at approximately the same angle of attack at which it separated.

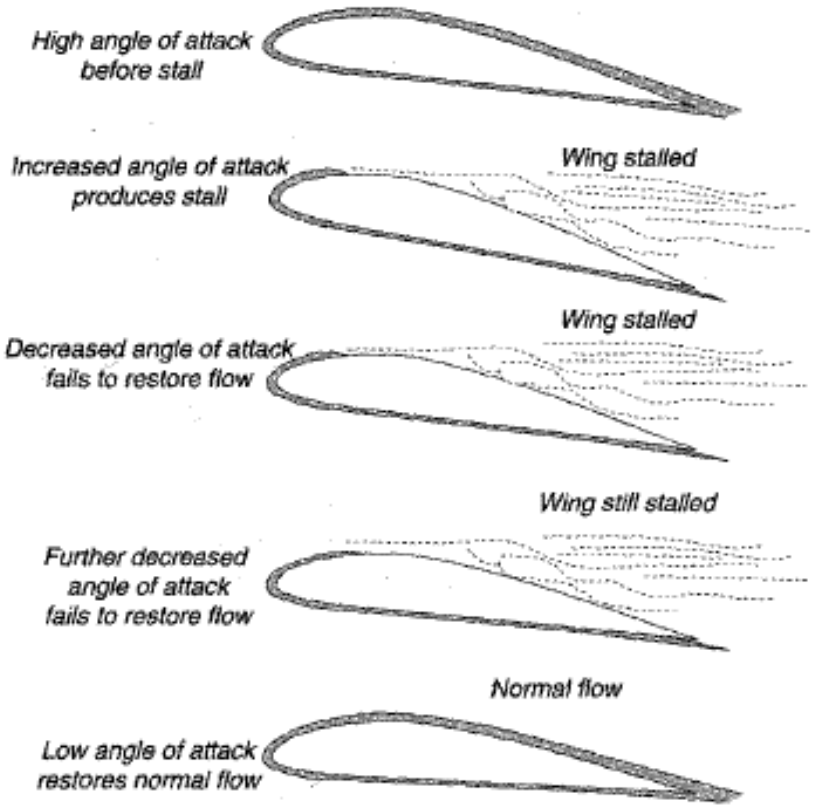

Hysteresis. At low Reynolds numbers, near the critical figure for the wing profile, a stall produced by increasing the angle of attack tends to persist until the angle of attack is much reduced. The normal expectation of a constant stalling angle tends to break down

Figure 2-14: Hysteresis Behavior of a Wing at Low Reynolds Number (Simons, 1999)

Due to these effects drag polars and moment coefficients become highly nonlinear and abnormal[10]. Figure 2-15 clearly illustrates this behavior; the lift-to-drag ratio increases with increasing lift coefficient to near the stall point for Reynolds numbers below 200,000 on this thick profile. Such behavior is highly dependent on the profile studied [11].

---

[9] (Simons, 1999)
[10] (Shyy, Lian, Tang, Viieru, & Liu, 2008)
[11] (Selig, Donovan, & Fraser, 1989)

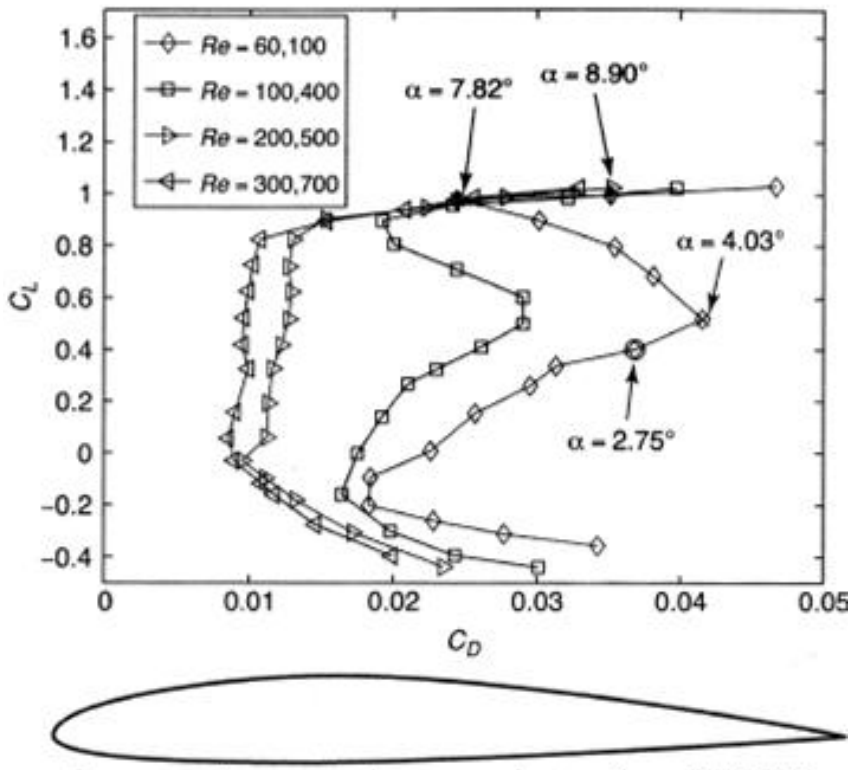

Figure 2-15: Drag Polars of an Eppler E374 Airfoil at Low Reynolds Numbers (Shyy, Lian, Tang, Viieru, & Liu, 2008)

2.3.2 Three Dimensional Low Aspect Ratio Aerodynamics

The large performance benefits to be gained by increasing Reynolds number above 75,000 suggested that reducing aspect ratio and increasing chord could provide performance benefits in this unique case. According to classical aerodynamics increasing main wing aspect ratio (b^2/s) increases efficiency by reducing induced drag. However, with poor airfoil performance at low Reynolds number and extreme sensitivity to increasing Reynolds number it appeared that an optimum balance would exist. Kellog, et al. (2001) working on the NRL MITE MAV derived an expression, Equation 2-1, for optimum rectangular planform chord length[12]. This would provide minimum wing drag at a given velocity and wing span. Since Equation 2-1 has a Reynolds number dependence in the calculation of K_1 based on two dimensional zero lift drag coefficient the solution is iterative.

[12] (Kellogg, et al., 2001)

$$c = \left[\frac{3}{\pi \times e \times b}\right]^{\frac{3}{4}}, K_1 = C_{d_o}(\mathrm{Re})^{\frac{1}{3}} \left[\frac{\mu}{K_1\left(\frac{\mu}{\rho V}\right)^{\frac{1}{3}}}\right] \quad \textbf{2-1}$$

Low aspect ratios also produce non-standard effects. Extremely low aspect rations can postpone stall to higher angles of attack. Rectangular planforms can maintain attached flow up to 35° as seen in Figure 2-16. This work was done with 2% thick 4% circular cambered flat plate airfoils [13]. Significant differences in performance would be realized by using other airfoil profiles and planforms.

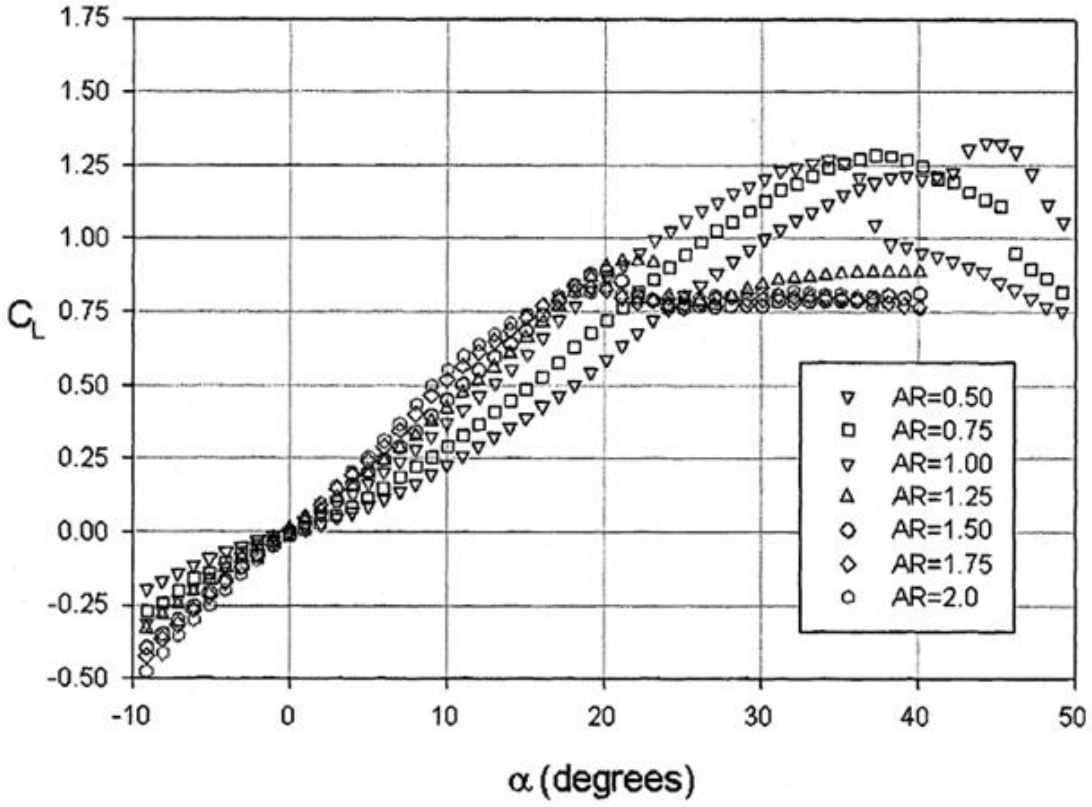

Figure 2-16: Lift Coefficient Versus Angle of Attack for Low Aspect Ratio Rectangular Planforms at Re=10^5 (Mueller, Torres, & Srull, Elements of Aerodynamics, Propulsion, and Design, 2006)

It is possible that the efficiency benefits from increased chordwise Reynolds number could outweigh the penalties incurred by a lower aspect ratio in these flight regimes. In addition, the increased angle of attack attainable before stall should make these aircraft more controllable since atmospheric gusts on the order of their flight speed would be less likely to stall the main wing.

[13] (Mueller, Torres, & Srull, Elements of Aerodynamics, Propulsion, and Design, 2006)

2.4 Ballistics

Due to the ballistic trajectory of launch and the necessity of gyroscopically stabilizing the stowed geometry some basic ballistics knowledge was required. Fin stabilized projectiles conveniently have a negative pitching moment coefficient. However, a gyroscopically stabilized body frequently has a positive pitching moment coefficient. This is due to the combination of a tapered nose and blunt aft body, characterized in Figure 2-17 and a near uniform density distribution forcing the center of gravity aft of the center of pressure.

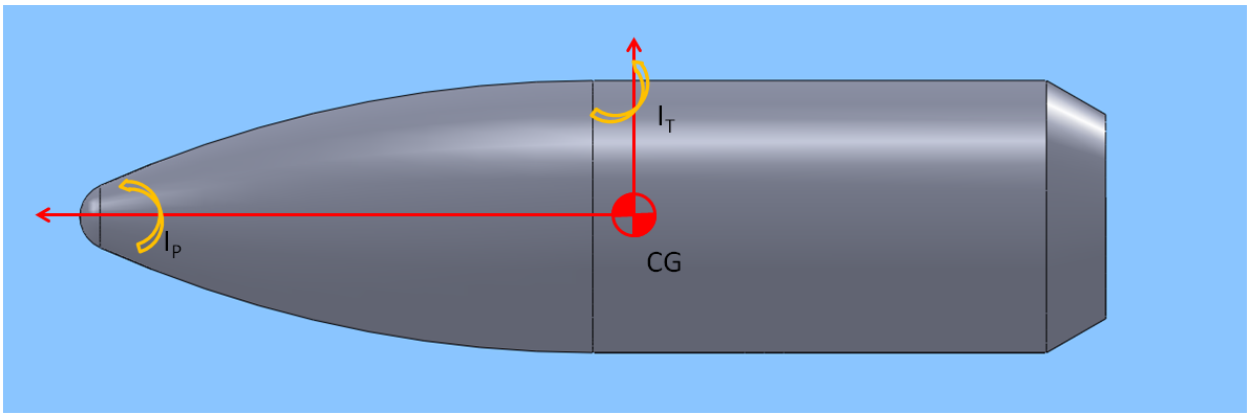

Figure 2-17: Characteristic Gyroscopically Stabilized Body Showing CG Location and Axis for Polar and Transverse Moments of Inertia

Information in *Ballistics: Theory and Design of Guns and Ammunition*[14], presents the static stability criterion for a gyroscopically stabilized projectile. Note that the pitching moment coefficient is the only value dependent on the relative locations of the center of pressure and center of mass. If this value is insufficiently negative then the projectile would be statically unstable. To compensate for an insufficient restoring moment a spin rate would be required. However, to deploy lifting wings and directly enter gliding equilibrium the spin must be stopped and the aircraft oriented within less than 90^o of upright. A slowly decreasing spin rate can cause tumbling as the spin rate approaches and drops below the threshold for stability. This is due to dynamic effects discussed in detail in Carlucci and Jacobson's text. To avoid the tumbling issue, illustrated in Figure 2-18, the stowed MAV must "jump" down in spin rate and rapidly transfer to aerodynamic stability.

[14] (Carlucci & Jacobson, 2008)

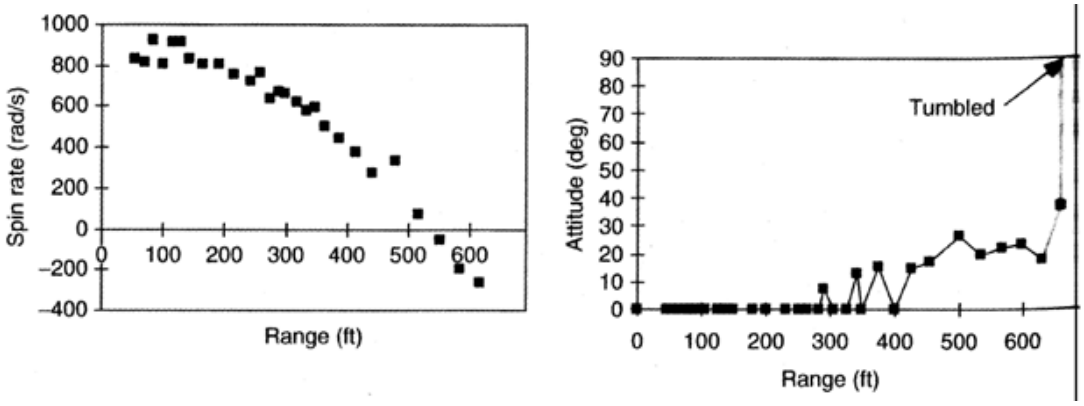

Figure 2-18: Increasing Dispersion and Developing Instability of a Slowly De-Spinning Round (Carlucci & Jacobson, 2008)

Non-rigid internal components can also cause significant problems with ballistic flight. Harmonics induced by any launch shocks and the high spin rates can cause large trajectory dispersion or even structural failure. The lag time to bring these components into equilibrium can be problematic even if the steady-state flight analysis proves acceptable[15].Significant structural analysis work will be required to characterize these effects.

2.5 Thesis Outline

While any design process is necessarily recursive a general trend was followed with this project and this thesis reflects the same order. Work began with structural stowage concepts. This provided the maximum aerodynamic surface limits and available fuselage volumes. Within these limits Missile DATCOM, discussed further in Chapter 4, was used to obtain initial main wing and tail sizes for a 200% range extension. This long-range capability dictated a moderate wing area and speed, 60 cm^2 and 33 *m/s*.

Preliminary computational work was then possible. CFD simulations of the stowed geometry were conducted since experimental results for a simple blunt cylinder were available. This experimental data was used to generate a suite of mesh and Fluent solver settings which were flexible enough to support the inclusion of wings. Two deployed geometries were considered, a conventional high aspect ratio layout and a truncated delta planform. The delta wing proved to have nearly twice the lift-to-drag ratio of the conventional layout. As discussed in Section 2.3 the benefits of increasing chordwise Reynolds number outweighed the benefits of increased aspect ratio. Therefore the delta wing was selected for all future work.

[15] (US Army Armament Ballistic Research Laboratory, 1984)

With the delta planform selected an optimization analysis was conducted using classical aerodynamic theory. Initially a range of launch angles was studied to see how wing area and range varied with apex/cruise velocity and apex altitude. This analysis showed that initial performance goals of both a flight time greater than thirty seconds and a 30% range increase were driving the design in opposite directions and a compromise would not perform well at either. A 30% range extension was possible with a direct, high-speed glide straight to the location at a high wing loading. However the surveillance option required a much lower flight velocity and greater range. Therefore the research was split to follow two tracks: one a small wing high-speed version for extended range to target, and the other a large wing, low speed, long endurance variant for surveillance purposes.

Parametric CFD studies were conducted in Fluent on all components with the goal of finding clear optimums or tradeoffs. An array of fuselages, airfoils, and wing planforms was studied. With this mass of data two final configurations were proposed. A summary of the process is provided in Table 2-2.

Table 2-2: Thesis Outline Summary

1) Structural Concept Modeling
2) Control Surface Actuation Concepts
3) De-Spin and Orientation Methods
4) Initial Surface Sizing Calculations
5) Stowed Geometry Mesh Generation
6) Deployed Configuration Simulation
7) Classical Aerodynamic Optimization Analysis
8) Fuselage Analysis
9) Two Dimensional Low Reynolds Number Airfoil Analysis
10) Preliminary Three Dimensional Main Wing Analysis
11) Recommended Preliminary Designs
12) Summary and Recommendations

Chapter 3 Concept Development

Initial work began with developing wing storage concepts. The entire project depended on developing a method to collapse sufficient wing and tail area into the stowed geometry leaving sufficient volume for sensors, controls, and other mission equipment. Multiple different methods were considered including completely encased MAVs and shells which transformed their exterior surface using either rigid structures or flexible components.

3.1 Structural Concept Modeling

Two fundamental stowage systems were proposed in the initial concepts provided by our research sponsors. "Cargo" type designs, as presented in Figure 3-1, shed a casing which fully surrounds the UAV and provides some support and cushioning from launch loads. These also permit flexibility of the fuselage shape within the limits of the discarded shroud. Figure 3-2 provides and outline of the progression of the Cargo designs developed at WVU and a schematic of their deployment sequence.

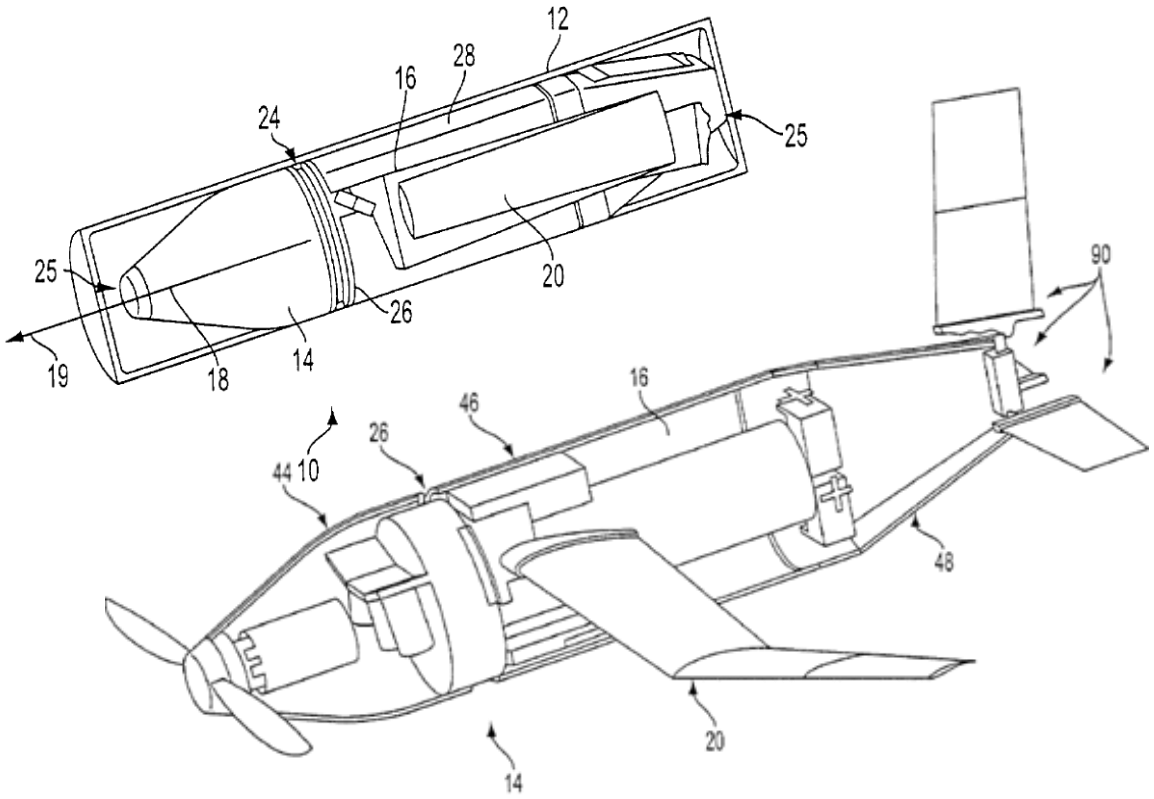

Figure 3-1: Cargo Type Design: Draper Lab's Flyer (Martorana, et al., 2003)

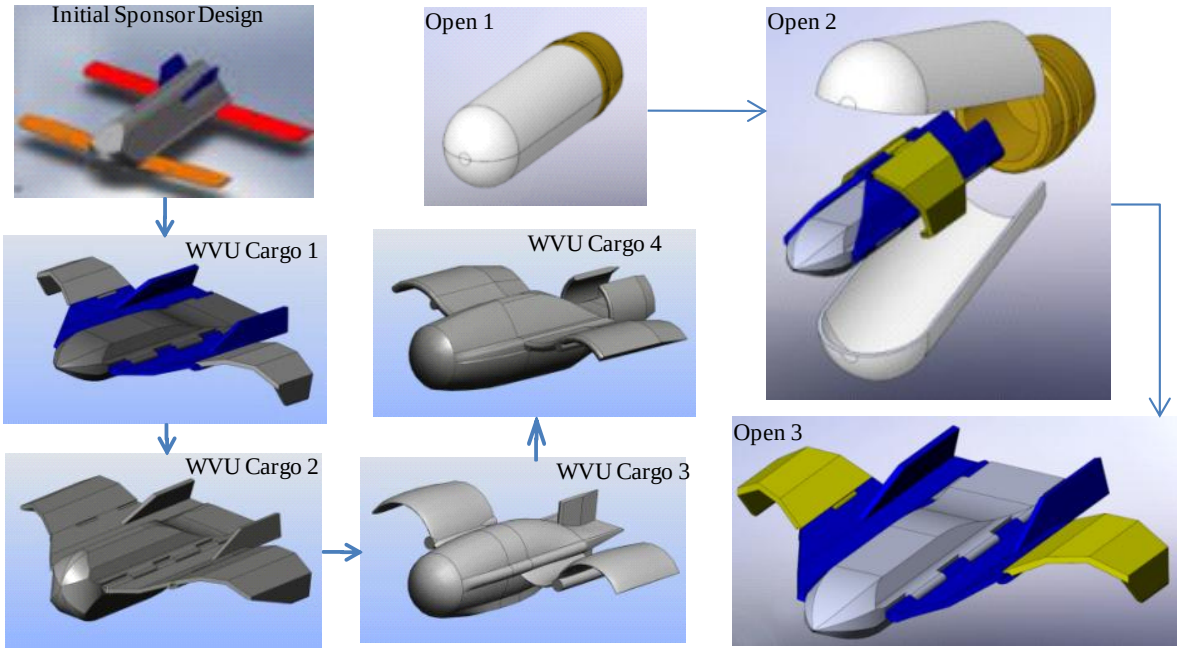

Figure 3-2: Design Progression of WVU Cargo Work and Opening Sequence

Alternately a "transformer" type configuration, Figure 3-3, could be used to increase the useable volume fraction of the stowed configuration. Only a thin shield or base support would be discarded, leaving the maximum possible volume available for the MAV. However, the fuselage design was far more constrained. Figure 3-4 provides a brief overview of the transformer type design progression and the deployment process of a transformer system.

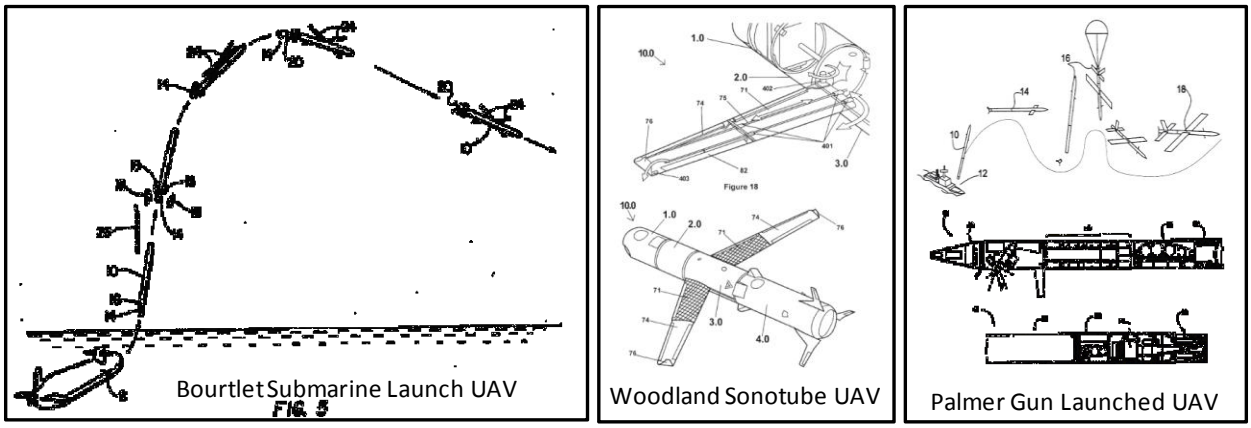

Figure 3-3: Transformer Type Sonotube, Missile Tube, and Naval Gun Designs (Woodland, 2000) (Bourlett, 1997) (Palmer, 2001)

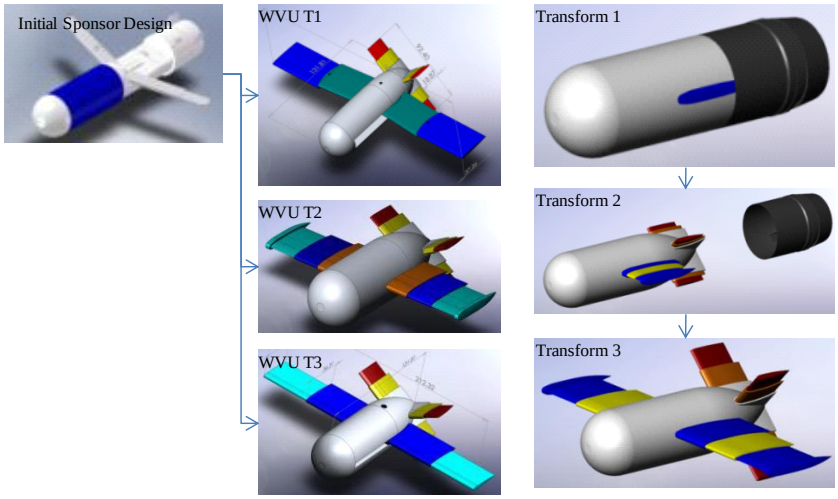

Figure 3-4: WVU Transformer Design Progression and Transformer Deployment Process

Two fundamental wing structures were also examined; solid segments which would swing or fold out to position, and membrane or other flexible segments which would un-wrap or expand. Figure 3-1 and Figure 3-3 illustrate the solid wing configurations while Figure 3-5 provides some examples of the flexible wings. Flexible wings included both composite thin plate airfoils and inflatable envelopes or durable, compressible foam to provide thick airfoil profiles.

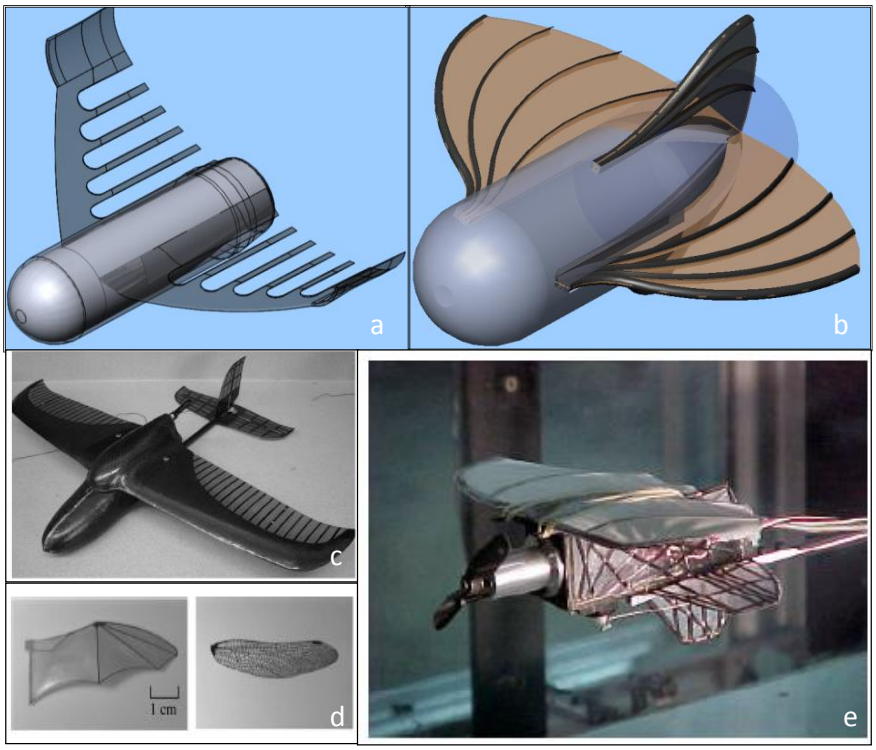

Figure 3-5: Membrane Wings Concepts, a) WVU Wrapped, b) WVU Leaf Spring, c) Batten Reinforced (Stanford, Abdulrahim, Lind, & Ifju, 2007), d) Titanium-Mylar Insect Scale (Pornsin-sirirak, Tai, & Ho, 2001), e) Small Scale Batten Reinforced (Fleming, Bartram, Waszak, & Jenkins, 2001)

3.1.1 Cargo Stowage Concepts

Cargo concepts are characterized by shedding a complete shell or casing from the stowed geometry and deploying a small MAV of arbitrary external geometry. This provides significant design freedom in both wing planform and fuselage shape but can waste large amounts of the available stowed volume.

3.1.1.1 Switchblade

The initial cargo concept was a "switchblade" configuration, very similar to a scaled version of AeroVironment's SOAR, which was provided by the research sponsors (Figure 3-6). This configuration was quickly discarded for two reasons. First, the thin wings would have operated at a chordwise Reynolds number under 50,000, severely compromising their efficiency. Second, the fuselage kept less than 22,000 mm^3 useable volume of the initial 160,000 mm^3 available in the stowed configuration, barely an eighth of the useable capacity. Note that for all cases only the fuselage volume was considered useable. The wing structures were all far too thin to contain anything but the smallest actuators and certainly no mission payload.

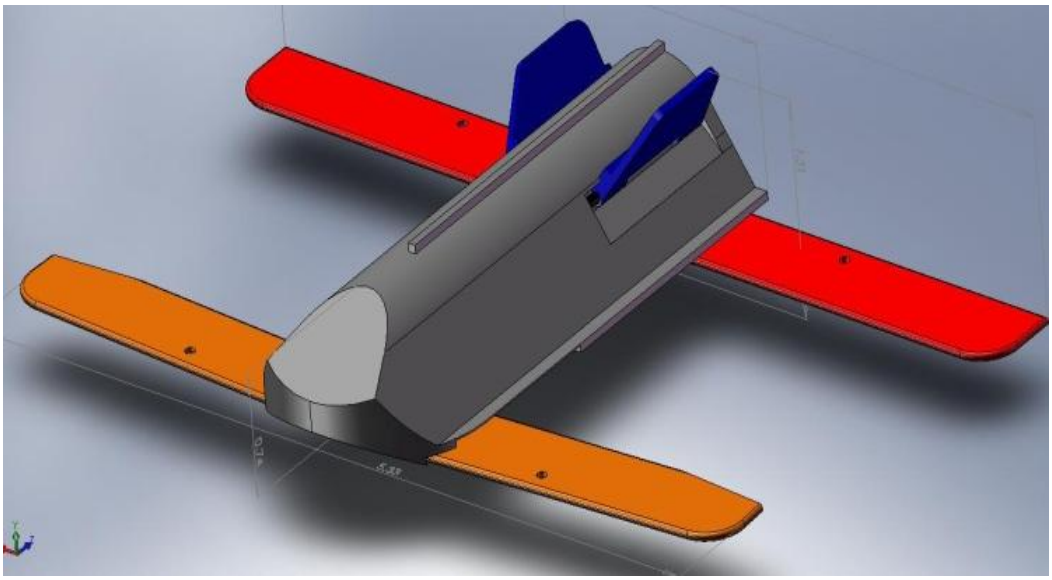

Figure 3-6: Initial Switchblade Concept

3.1.1.2 Wrapped Solid Wing

One of the first methods studied was a folding solid wing. A highly contoured wing with multiple chordwise hinge points modeled to "wrap" around the fuselage as shown in Figure 3-7.

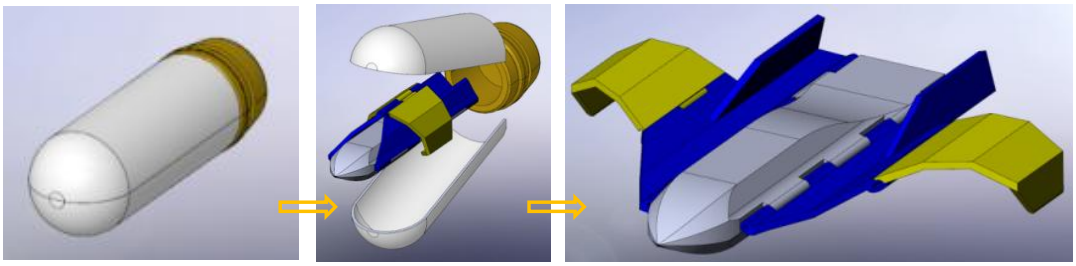

Figure 3-7: Deploy Process for Wrapped Solid Wing Cargo Designs

This permitted both a much higher chordwise Reynolds number, up to 100,000, and maintained far larger fractions of the useable capacity. Both the initial design and the four succeeding improvements of the solid structure configuration are shown in Figure 3-8. Available fuselage volume increased from 25,000 mm^3 to 57,000 mm^3.

Pros:

- Full airfoil profiles possible
- Simpler designs could use molded, cast, or "rolled" manufacturing to keep costs down

Cons:

- Complex wing stowage system
- Full discarded casing may interfere with deployment or de-stabilize MAV during opening
- Poor volumetric efficiency when compared to later WVU solutions
- Complex transformation process

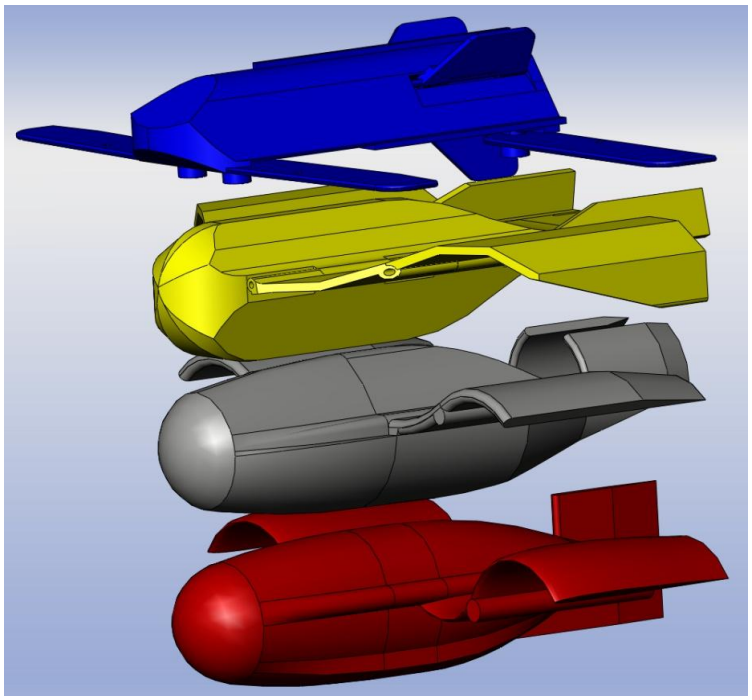

Figure 3-8: Solid Wrapped Wing Design Progression

3.1.1.3 Wrapped Membrane Wing

Initially it was thought that membrane wings would be impossible on this configuration for designs requiring wing half-spans greater than three fourths to seven eighths of the circumference of the fuselage. This was due to the fact that one wing would have to wrap under the other and would conflict with the fuselage-wing junction of its twin. A slot through the fuselage, or an off-set mounting, combined with a moderate rearward leading edge sweep near the root chord solved the problem as shown in the top right of Figure 3-9 and covered in more detail in Section 3.1.2. With this design the inner-wrapped wing could pass freely under the root chord of the outer wrap. Only the composite substructure of the membrane wing has been shown in the figures. Either a rubber or fabric skin would be stretched over the surface to provide the final airfoil shape.

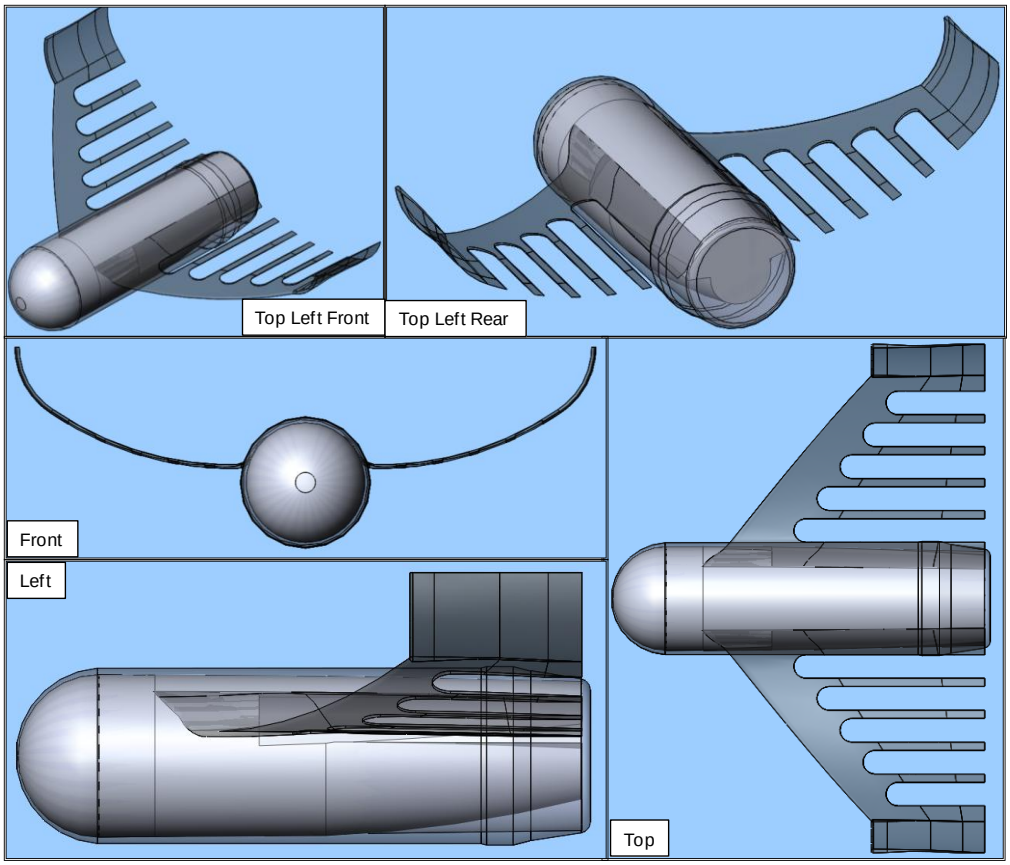

Figure 3-9: Wrapped Membrane Wing Concept

As Figure 3-9 shows, the wrapped membrane structure kept a far larger fraction of usable volume than any solid wing configuration, on the order of 100,000 mm^3. This design was also far more flexible in terms of planform and multi-purpose components. Further discussion of this design is presented in Section 3.1.2 since it was the first of two structural systems that showed the most promise for implementation.

Pros:

- Excellent volumetric efficiency
- Can provide thin-plate to full depth airfoil profiles as detailed in Section 3.1.2
- Design lends itself to dynamic wing morphing techniques such as adaptive washout
- Can imitate bird wing shapes to provide stealthier operation through misdirection

Cons:

- Wings may be difficult to deploy symmetrically

3.1.2 Wrapped Membrane Structure Detail

Composite membrane structure designs have been informed by the significant work done at the University of Florida. Figure 3-10 shows a MAV using a curved flat plate airfoil which relies on the cambered composite leading edge for spanwise rigidity. A more highly cambered wing could likely be made of a thinner, more flexible laminate as its cross-sectional moment of inertia would be greater.

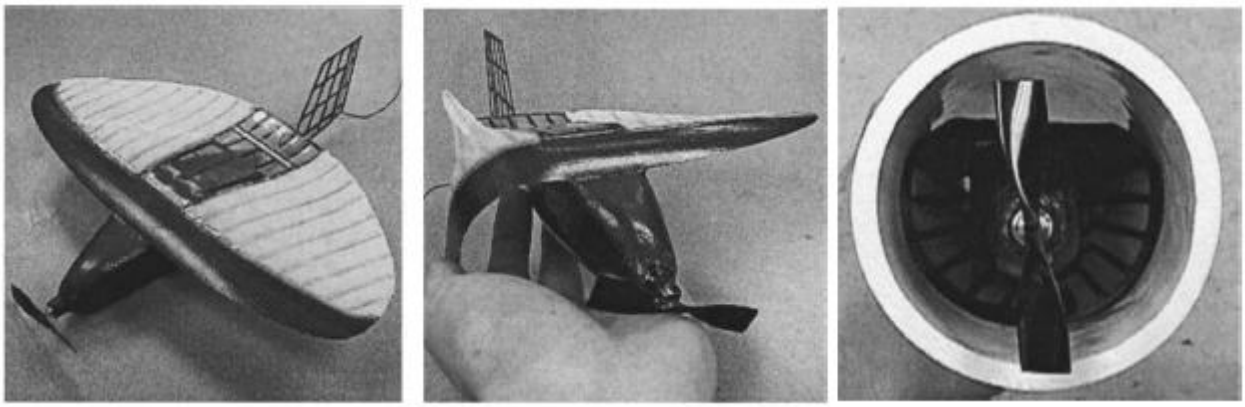

Figure 3-10: Cambered Plate MAV With Wrappable Wings (Shyy, Ifju, & Vieru, Membrane Wing-based Micro Air Vehicles, 2005)

Span limitation was an early concern with the wrapped wing designs. Since both wings would have to wrap down around the fuselage initial designs were limited to the arc length between one main wing root chord and the other. This was overcome, as shown in Figure 3-11, by incorporating a slot which first wrapped one wing through a slot under the main wing root. The second wing would then wrap around the outside. With this modification spans were limited only by the ability of the system to un-coil from the stowed configuration.

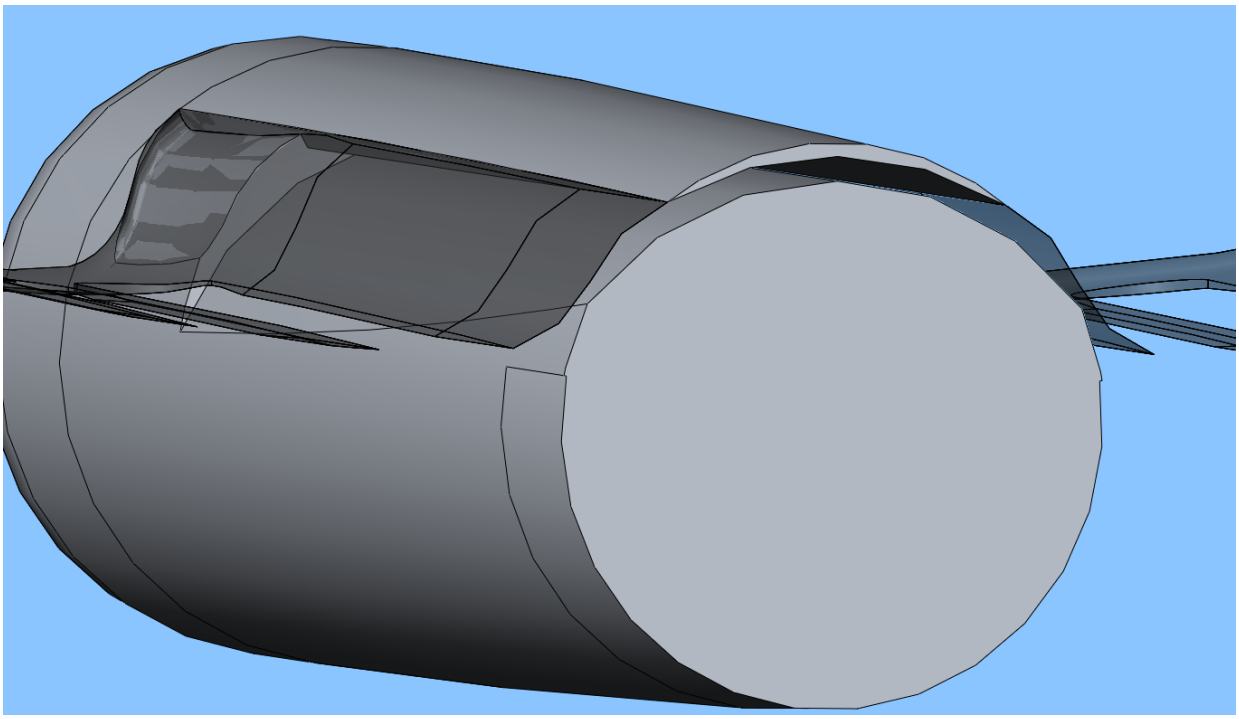

Figure 3-11: Slot For Inner Wrapped Wing Pass-Through

Full airfoil profiles could be created by using either highly compressible open cell foam rubber or inflatable envelopes as shown in Figure 3-12. A full airfoil profile could both increase efficiency and rigidity with the inclusion of tension fibers on the lower surface.

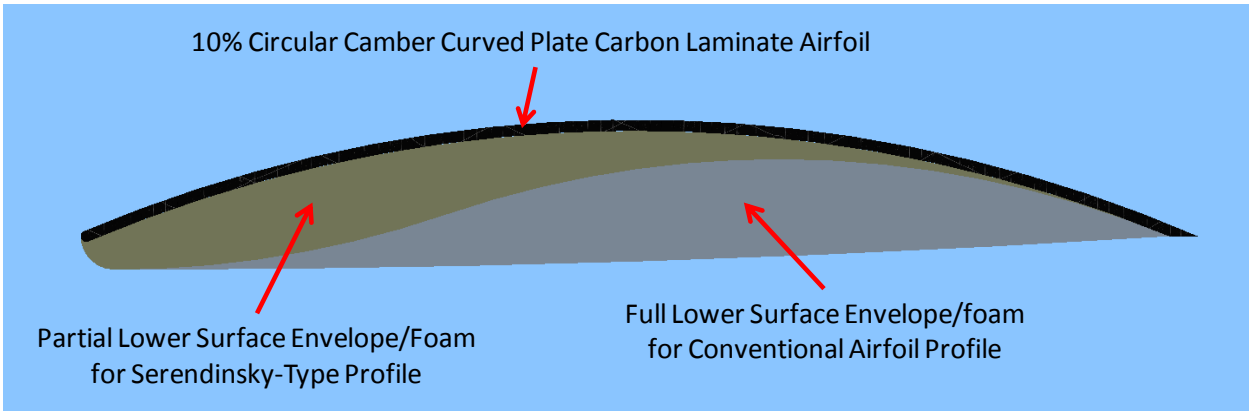

Figure 3-12: Inflatable or Expandable Lower Surface Profile on Membrane Wing

Each of these methods can be combined with a "batten reinforced" wing. Battens, in the terminology of Ifju, et al., are the composite ribs extending aft from the wing leading edge as shown in Figure 3-9. They allow the trailing edge of the wing to deflect into oncoming gusts and reduce the change in lift caused by atmospheric disturbances thereby enhancing stability.[16] Figure 3-13 shows a pair of batten reinforced structures. The left image is a high aspect ratio wing incorporating both adaptive washout and a torque rod for control purposes; the right is a much smaller MAV using only adaptive washout.

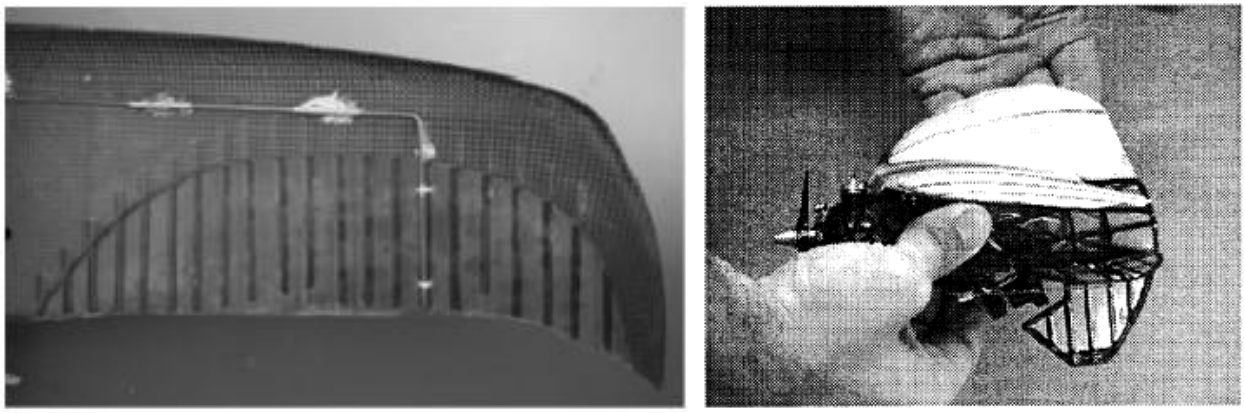

Figure 3-13: Batten Reinforcement and Adaptive Washout Detail (Stanford, Abdulrahim, Lind, & Ifju, 2007), (Ifju, Ettinger, Jenkins, & Martinez, 2001)

The usual method for creating a MAV wing with adaptive washout has been to create a composite laminate with a stiff leading edge structure and several trailing battens of unidirectional carbon fiber. A flexible, usually elastic, membrane is then bonded over the upper surface. This structure permits the wing chord to deform into an oncoming gust. Gust tolerance has been extremely important as flight speeds of MAVs are on the order of atmospheric gust velocities.

A previous wing morphing system developed at West Virginia University for the control of a tailless flying wing could be adapted for use on a membrane wing. The combination of a curved actuator rod, free-floating "feathers" and a common hinge line (Figure 3-14) allowed the creation of a continuous, smooth change in wingtip angle of attack. A latex and polypropylene skin has been omitted from the figure for additional clarity. Modifications to this system could incorporate more flexible feathers and multiple actuator rods to enable far more dynamic control input incorporating both angle of attack and camber changes.

[16] (Ifju, Ettinger, Jenkins, & Martinez, 2001)

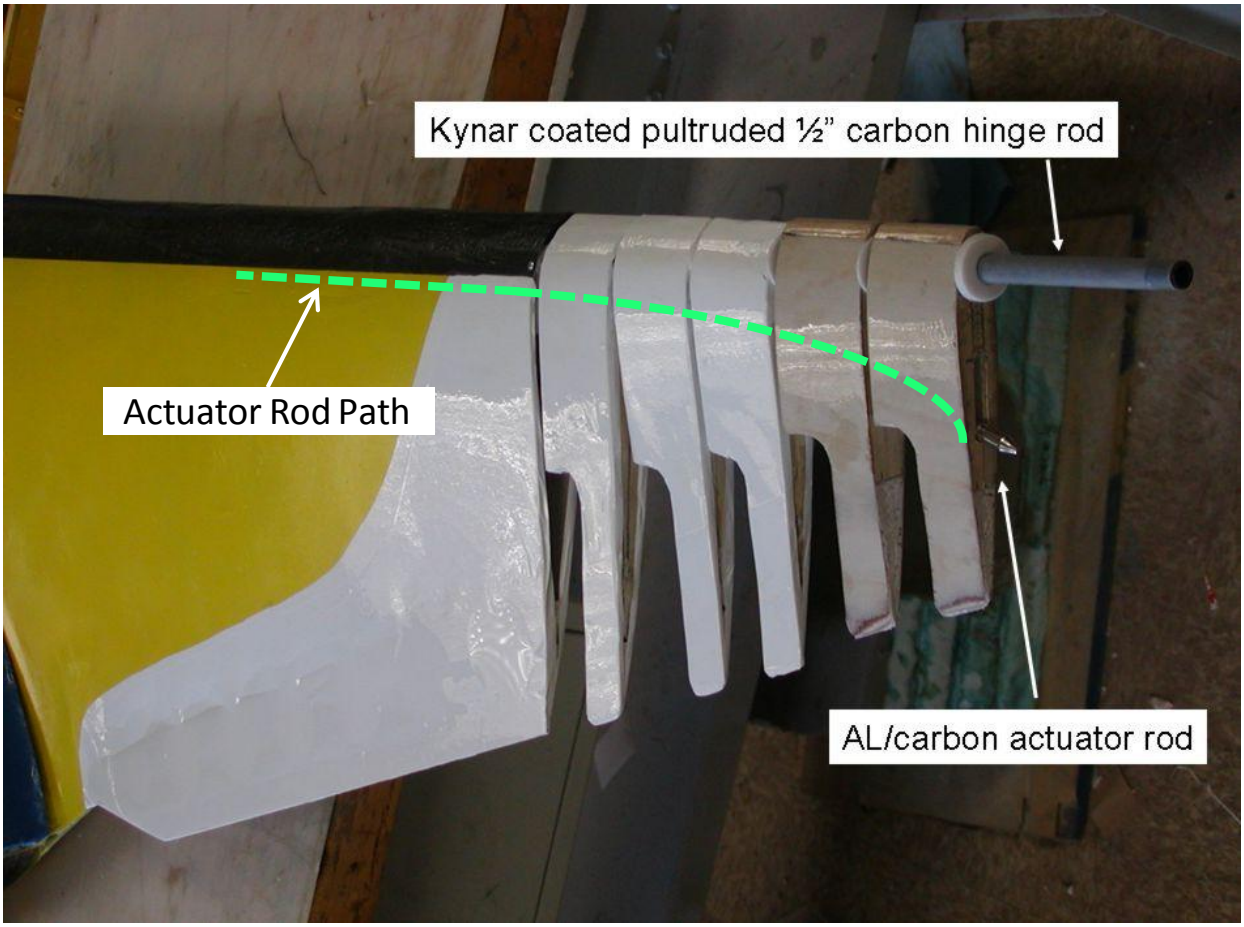

Figure 3-14: "Feathered" Wing Morphing System for WVU Horten Flying Wing (Guiler, 2007)

Membrane wings would give the maximum planform diversity. Blended vertical surfaces could be incorporated at the wing tips, or a biomimetic planform could be used. Figure 3-15 shows an array of possible layouts. Bird like planforms can provide stability without vertical surfaces at these scales as shown by Sachs, 2007. The rearward swept tips generate an induced drag imbalance when encountering a side-gust. Focusing attention on the Frigatebird in Figure 3-15 it can be seen that a side-gust from the right will increase lift and drag on the outboard right wing and inboard left wing while reducing both on the outboard left and inboard right wings. The forward swept inboard wing keeps the total amount of lift nearly constant while the reduced drag on the left tip and increased drag on the right tip act to rotate the bird into the oncoming gust.

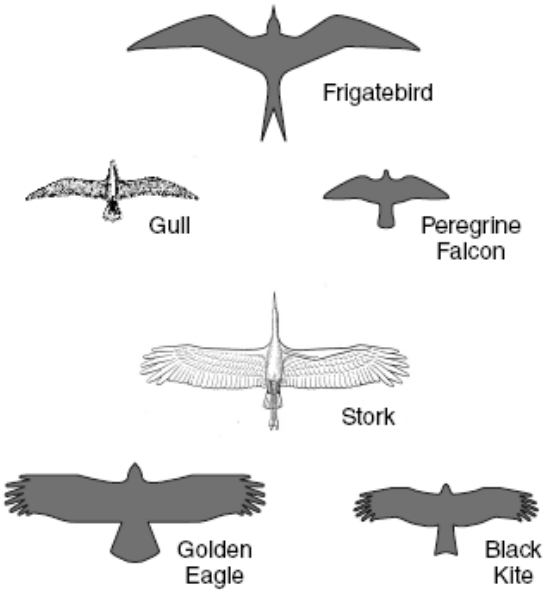

Figure 3-15: Potential Biomemetic Membrane Wing Configuration Diversity (Sachs, 2007)

Figure 3-16 provides Sach's scale analysis showing a reduced required yawing moment for stability as mass is reduced. Smaller birds require a proportionally smaller restoring moment and their planforms can therefore be simpler. It appears that these same planforms should provide acceptable performance for the MAVs designed in this project. The hawk-like swept wings which provide these acceptable stability characteristics would be easy to manufacture with the methods discussed in this section. Using a cylindrical body, a biomemetic wing, and no vertical surfaces the visual signature of the MAV would be quickly discounted by observers.

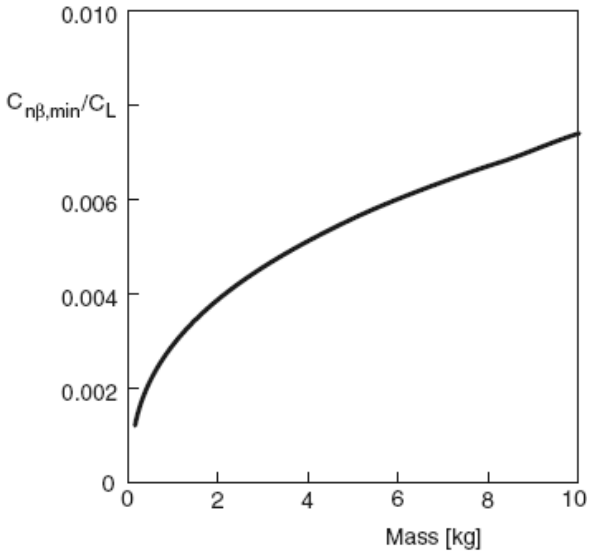

Figure 3-16: Correlation Mass and Required Yaw Stability with Behavior of a Clean Swept Biomemetic Planform(Sachs, 2007)

3.1.3 Transformer Stowage Concepts

Three transformer concepts were developed. The first two incorporated solid wing and tail structures. A novel "leaf-spring" system was conceived third. Transformer designs, initially stemming from the "telescopic" system (Figure 3-17) developed by the sponsor, quickly proved to be more than worth the additional design difficulty. Initial designs kept 100,000 mm^3 of useable fuselage volume, nearly 66% of the stowed configuration. The best solid-wing cargo designs kept barely 25%.

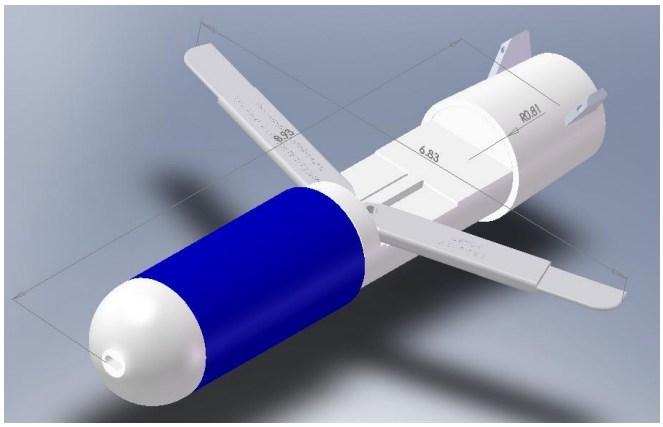

Figure 3-17: Sponsor Telescopic Transformer Concept, (dimensions in *cm*)

3.1.3.1 WVU Switchblade Transformer

All WVU transformer concepts significantly reduced the complexity of the sponsor's initial work. In all cases the fuselage was a monolithic volume rather than the multiple sliding elements shown in Figure 3-17.

The switchblade transformer system was the simplest system. Sets of single or multiple "fan" blade elements would be mounted on torsion springs as shown in Figure 3-18. These simple solid components could be easily and cheaply rolled or stamped for low cost. However, to conserve space only thin airfoils or cambered flat plates would be practical. An advantage of multiple wing elements was that they could be deployed at separate times to de-spin, stabilize, and orient prior to deploying lifting surfaces. This could be done by having multiple, staged wing deployments with separate sets of fins or fins which deploy further at a later point in the flight.

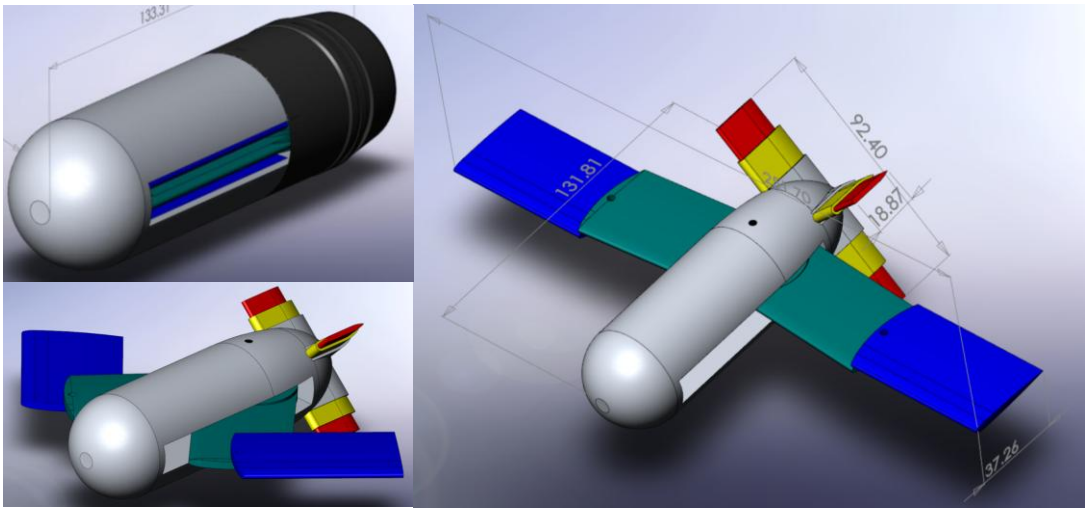

Figure 3-18: Switchblade Transformer Structural Concept, (dimensions in *mm*)

Unfortunately this design sacrificed large blocks of volume extending into the center of the fuselage. It is anticipated that there will be difficulty in the miniaturization of the electronics and payload without the structural design sub-dividing the available volume. In addition, most useful configurations opened slots through the center of the body. Air bleed through these gaps could cause significant instabilities which would be extremely hard to model and predict.[17]

Pros:

- Simple design
- Rugged torsion springs
- Full thin airfoil profile possible
- Can provide thin plate airfoil profiles

Cons:

- Open slot through center of fuselage
- Large block of central fuselage volume sacrificed

3.1.3.2 Telescopic Transformer

The telescopic transformer system increased complexity of both design and construction, but was able to increase both planform diversity and available internal volume. Figure 3-19 shows how a set of wing elements could telescope into one another creating both a small stowage volume and a complex planform. Note that there is no particular significance to the different colors in the figure other than ease of viewing.

[17] (Appich & Wittmeyer, 2001)

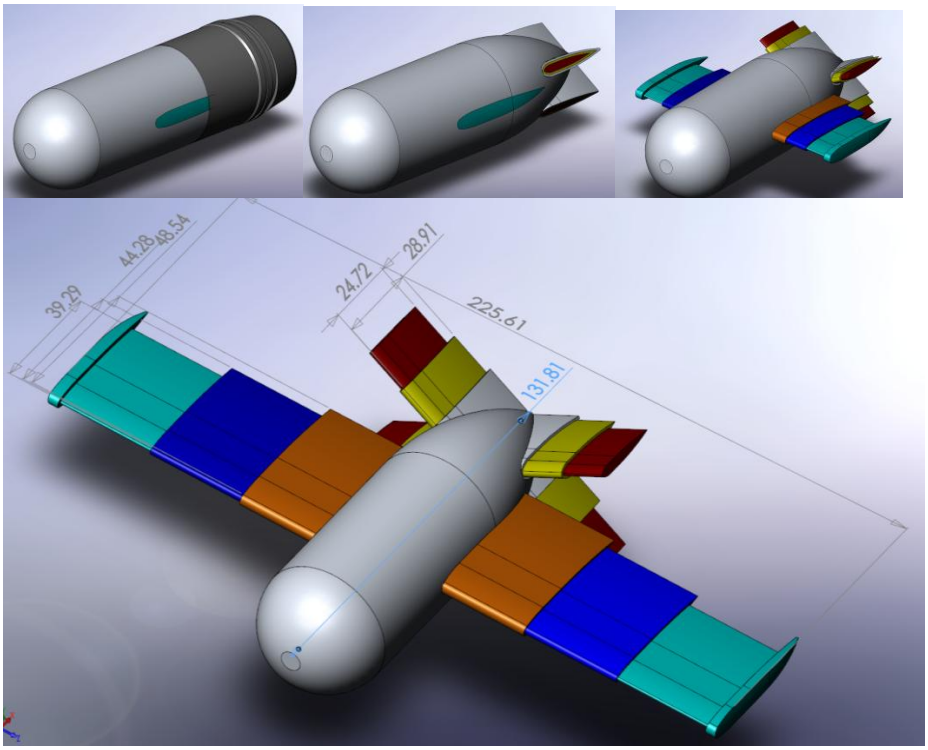

Figure 3-19: Telescopic Transformer Structural Concept, (dimensions in *mm*)

The large blocks on the wing tips served as both the surface seal of the stowed configuration and masses to increase the MAV's rolling moment of inertia. This was an important consideration in all designs since the extremely small moments of inertia of standard MAVs produce responses similar to fighter aircraft instead of the more desirable general aviation or transport aircraft dynamic characteristics.[18]

Again, like the Switchblade transformer, a large block of fuselage volume would be sacrificed. In addition, manufacturing and g-load problems may be encountered with the thin shell structures the wing requires.

Pros:

- High AR possible
- Sacrifices less volume than WVU switchblade
- Full thin airfoil profile possible

Cons:

- Sacrifices large block of useful volume
- Delicate manufacturing process for "shell" wing segments, prone to deformation

[18] (Morris, Design and Flight Test Results for Micro-Sized Fixed-Wing and VTOL Aircraft, 1997)

- Cannot provide curved plate airfoil profiles
- Cannot provide thick airfoil profiles

3.1.3.3 Leaf Spring Transformer

An elegant structural solution for a stowed-wing MAV was finally developed with the Leaf Spring system, shown in Figure 3-20. Elastic elements would be pinned together at the leading edge root and spread out in a fan when in the relaxed, deployed state. A membrane, either elastic rubber or taut fabric, would be stretched over at least the upper surface. When properly contoured, and with a taut membrane skin the leaf elements could support any thick airfoil contour by covering both upper and lower surfaces.

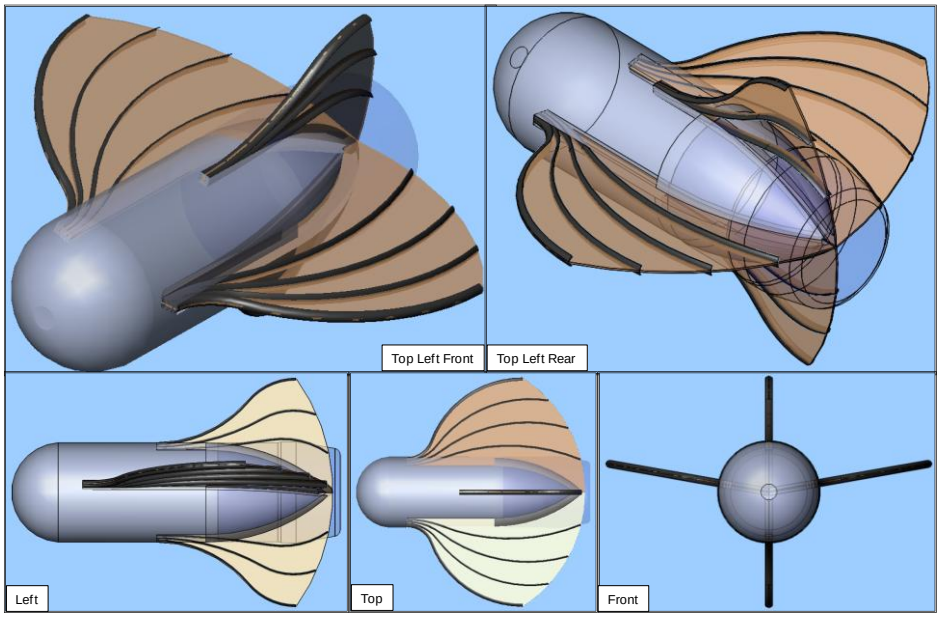

Figure 3-20: Leaf Spring Transformer Structural Concept

Volumetrically this system seemed to be by far the most efficient. With the leaves being the only solid components of the wing an extremely large area could be compacted into a much smaller volume than any other option, with the possible exception of the Wrapped Membrane system. Both methods left the central fuselage volume free for payload and electronics.

Problems this system could encounter include a somewhat difficult design of the leaves for a desired airfoil and planform shape, and difficulty in obtaining completely symmetrical wing deployment in both the transient phase and the final gliding shape. The aerodynamic analysis would also have to account for potential deformation of the membrane surface during flight. Unfortunately the span is limited by the mounting location, and the leaves may be forced to wrap around the fuselage tail for large spans. Span and tip chord are also cross-linked by the leading edge spar/tip rib leaf element as shown in Figure 3-21.

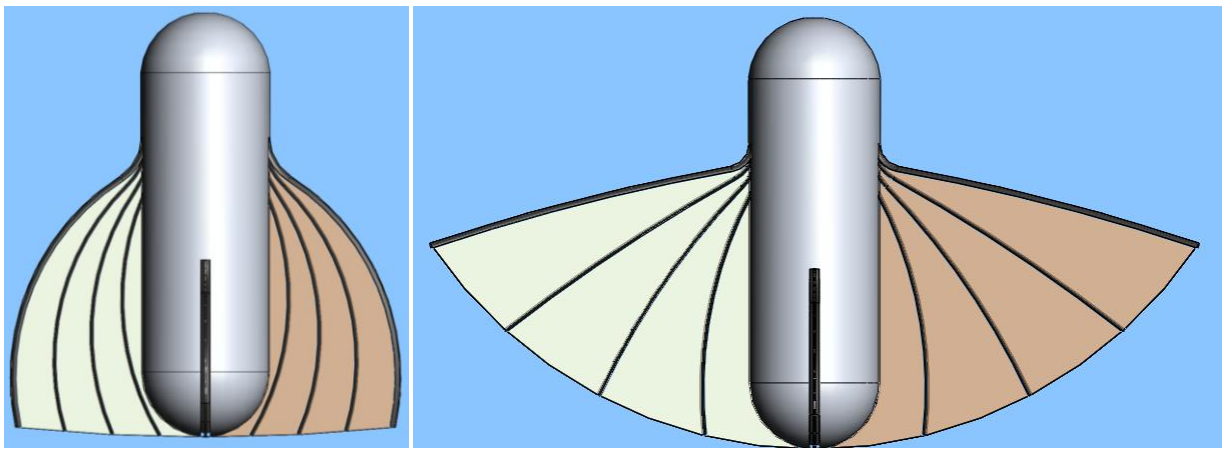

Figure 3-21: Inverse Relationship Between Span and Tip Chord Length of Leaf Spring Structure for Wings with Equal Length Leading Edge Leaves

Pros:

- Full airfoil profile possible
- Can support thin plate airfoil profiles
- Extremely small stowed volume
- Leaves center of fuselage available for payload and system components

Cons:

- Difficult design of leaf-spring element contours for desired airfoil shape
- Membrane covering will deform from desired shape
- Span-chord are cross-linked by leading edge spar/tip rib element
- Asymmetric deployment possible

3.1.4 Leaf Spring Structure Detail

Both thick, 10% thickness to chord ratio or greater, wing profiles and cambered plate airfoils could be coupled with a dynamic, morphing structure in the Leaf Spring concept. The minimal number of simple components move towards a rugged design with small stowage volume, and great planform and control diversity. Figure 3-22 illustrates how the relative angle between the fuselage centerline and the wing chord could be changed. All leaves would be mounted to a single rotating base point. This would remove the necessity to self-right. A tri or quad symmetry setup could be used. While requiring a control system able to re-orient for the rotated body reference frame the aerodynamic simplification may make this worthwhile.

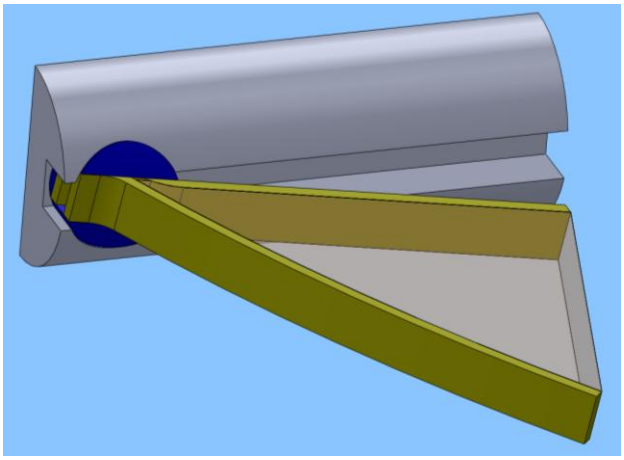

Figure 3-22: Method for Varying Leaf Spring Angle of Attack Relative to Fuselage; Gray) Fuselage With Slot for Membrane and Leaves, Blue) Rotating Mount for Leaves, Yellow) Leaf Spring Elements, Tan) Membrane Bonded to Leaf Upper and Lower Surfaces

Alternately some inboard leaves could be attached to an aft-mounted rotating base. This would form an effective control surface by altering wing camber around the rotated leaves as in Figure 3-23. It may be possible to couple this control system with the previous angle of attack alteration but more design work is required to prove this out.

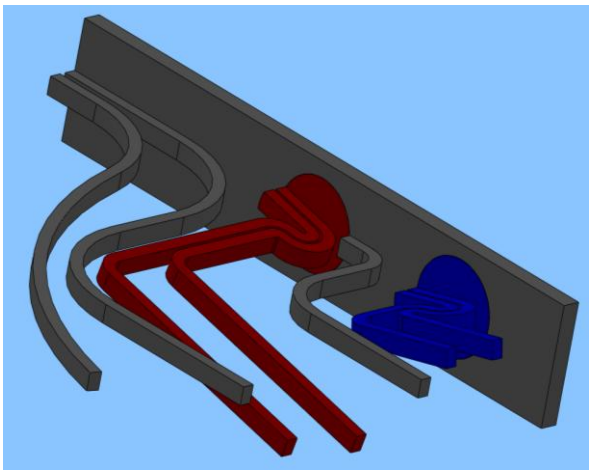

Figure 3-23: Rotated Leaves for Control Surface Actuation and Camber Modifications; Fixed Leaves and Fuselage (Gray), Outboard Surface Rotation Point and Leaves (Red), Inboard Rotation Point and Leaves (Blue)

Later powered versions may incorporate a method to actively change the amount the wings deploy, either through a winch system or active leaves of some variety. This system could be used to stage wing deployment as shown in Figure 3-24. Such a method would require an elastic membrane for the two-stage deployed main wings so that the appropriate airfoil shape would be maintained when not fully deployed during the de-spin and orientation phase.

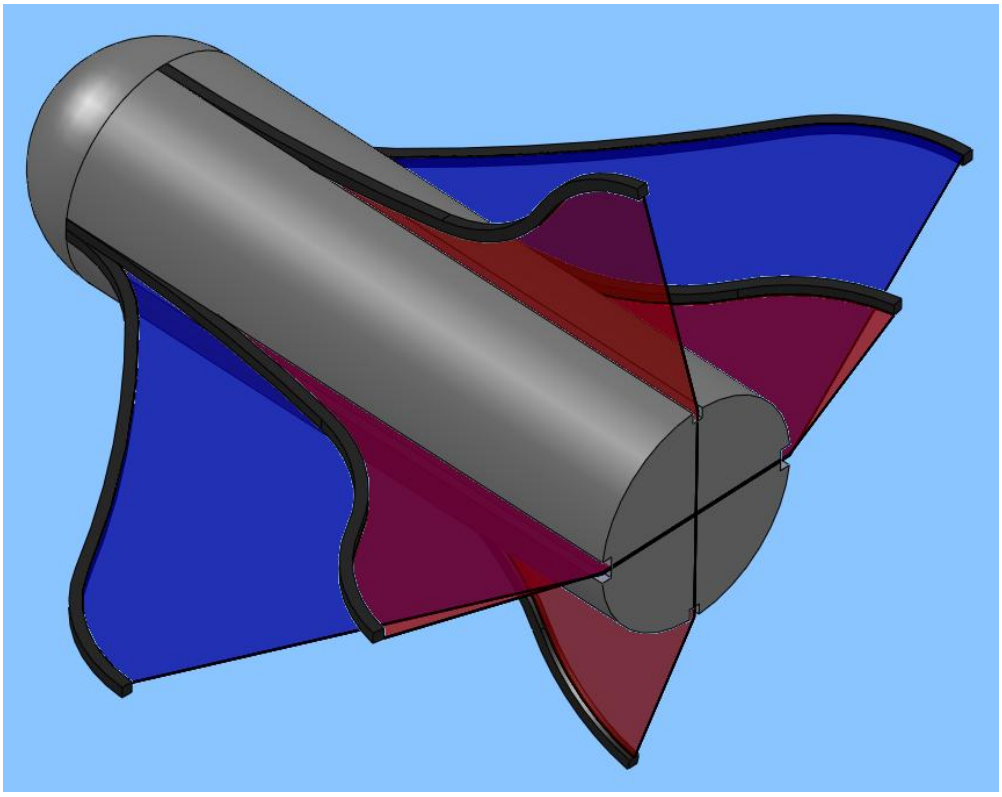

Figure 3-24: Staged Wing Deployment for Stabilization and De-spin; Red) Initial Deployment for De-spin and Orientation, Blue) Secondary Deployment of Main Wings

In addition, the ability to change wing area during flight could enable advanced maneuvers such as "bounding" flight described in *Design and Flight Test Results for Micro-Sized Fixed-Wing and VTOL Aircraft* (Morris, 1997) and shown in Figure 3-25. This shows how a bird, or an aircraft with variable wing area, can alternate between a ballistic trajectory and high-g pull-ups. This mode of flight could enable a powered aircraft to cruise at twice its optimum lift-to-drag velocity while operating near its maximum lift-to-drag ratio.

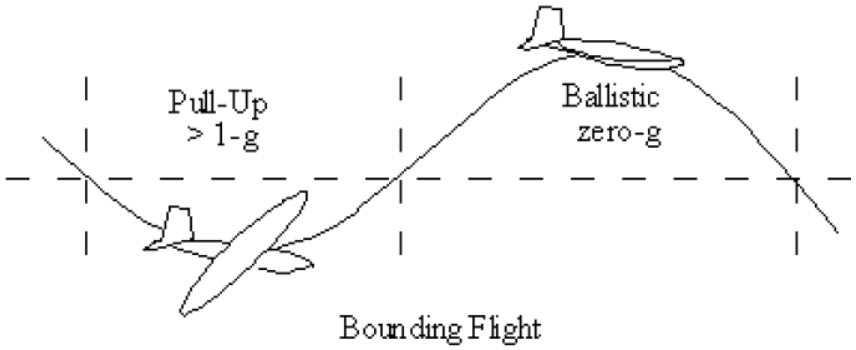

Figure 3-25: Illustration of Bounding Flight for Increased Cruising Speed (Morris, Design and Flight Test Results for Micro-Sized Fixed-Wing and VTOL Aircraft, 1997)

3.2 Control Surface Actuation Concepts

While future work may enable the use of advanced morphing control systems the present designs focused on incorporating simple, standard control surface systems into the collapsible wing structures discussed previously. This was an interesting problem requiring hinge lines capable of collapsing down in a plane perpendicular to their rotation axis. Several concepts were developed.

3.2.1 Torsion Rod System

Torsion rods for actuation of flexible wing surface deflection have been used by several previous small UAVS, and have been studied in detail at the University of Florida on a high aspect ratio batten reinforced wing [19]. Their work proved that, on a batten reinforced MAV wing, excellent roll control could be achieved using a system similar to that shown in Figure 3-26. A servo was used to apply torque to the horizontal rod along the quarter chord line. This rotated the two chordwise rods in the batten reinforced section of the wing to twist the wing structure in that region and provide an effective aileron control.

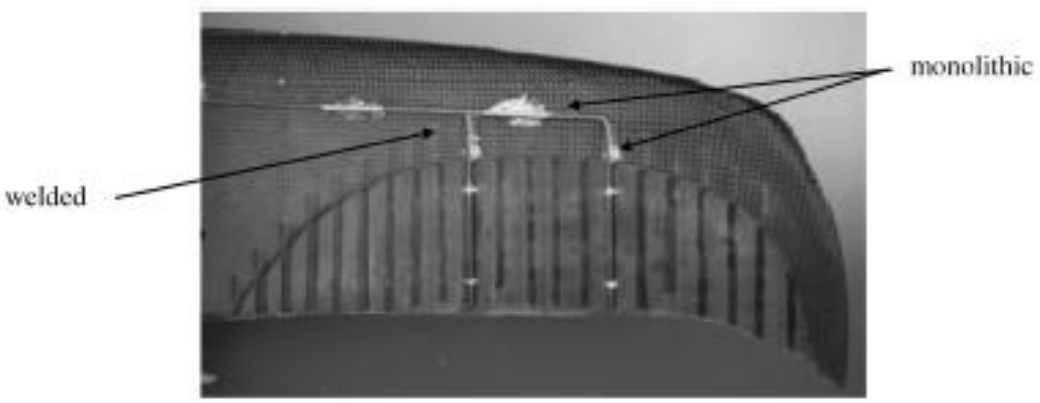

Figure 3-26: Torsion Rod Control System on Batten Reinforced Wing, Multiple Actuation Point Configuration (Stanford, Abdulrahim, Lind, & Ifju, 2007)

This work recommended locating the torsion rod in the weakest spanwise location to maximize the amount of deformation gained for the power applied. Unfortunately serious drag penalties were discovered when compared to conventional rigid wings and control surfaces. Control authority was comparable to conventional systems up to the point tip stall was encountered on the outboard wing. This may be a poor choice for a high wing loading design as tip stalls could be encountered when twisting the wing leading edge up.

[19] (Stanford, Abdulrahim, Lind, & Ifju, 2007)

3.2.2 Collapsible Flapped Surface

A control surface similar to a conventional hinged flap system was desired since it would provide a more known quantity. Unfortunately a simple hinged system could not be incorporated into the selected flexible wings without creating serious problems for either the hinge or stowage method. A compromise system, Figure 3-27, was developed. A more defined hinge line could be created by using a second set of rigid segments just forward of the control surface elements with a small gap between the two sets. The gap between the two sets of plates would then act as a defined living hinge. Alternately a high-tension spanwise line could be run just in front of the control surface elements between two adjoining battens and then be bonded to the membrane surface. This would also act as a defined hinge line for a living hinge. The rigid elements could be constructed from either a one-way flexible composite or plastic, or smaller completely rigid components. A pull-pull system would actuate control horns mounted to the central rigid control surface element. While the system would compromise the flexibility of the structure somewhat, the stowage system would still function and the system should operate nearly as a standard flapped system. For the leaf spring structure a compressible foam could be used to provide a trailing edge shape and compatibility with this system. Some efficiency improvements may even be gained since control surface gaps would be eliminated and the airfoil profile would not be modified to the extent a torsion rod system could generate.

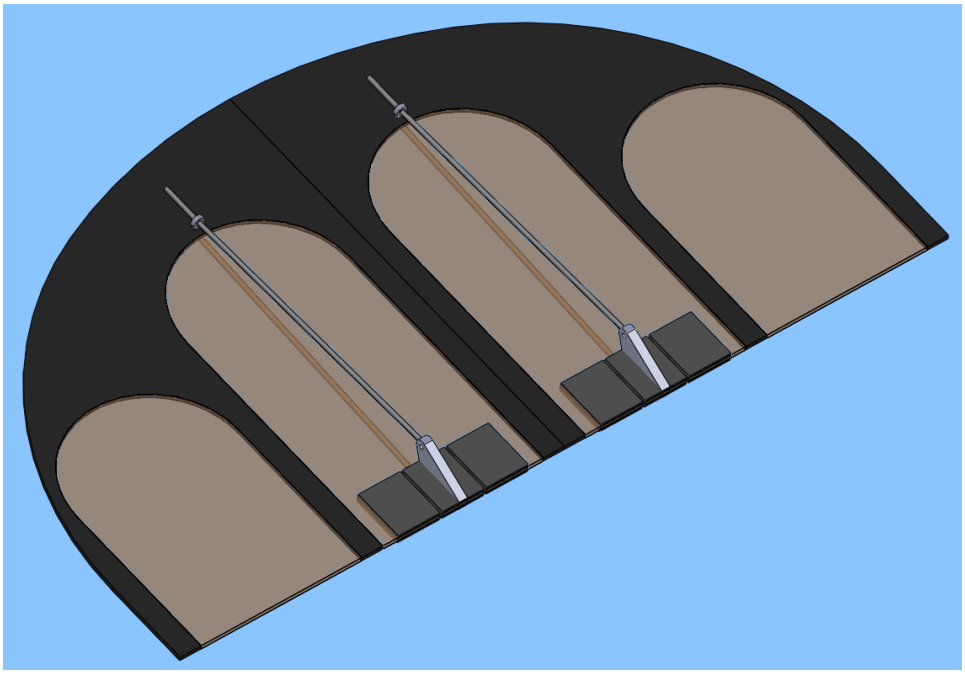

Figure 3-27: Effective Flapped Control Surface for Membrane Wings; Black) Carbon Laminate Structure, Tan) Membrane Surface, Dark Gray) Rigid Elements Bonded to Membrane, Light Gray) Control Horns and Cables for Pull-Pull Control

3.3 De-Spin and Orientation Methods

The gyroscopically stabilized shell must be de-spun prior to fully deploying any lift generating surfaces to avoid a massive recovery oscillation which may end with the MAV traveling in a random direction. With the specified center of gravity a high spin rate was required for gyroscopic stability. Slowly reducing this rate can permit Magnus instabilities to tumble the round. These instabilities are caused by asymmetric circulation lift generated by the round's axial rotation when at a sideslip or pitch angle of attack. High spin rates cause gyroscopic stability effects to override these destabilizing lift components, but as spin rate drops the round begins to diverge from its intended trajectory and eventually tumbles. Figure 3-28 shows an explosively formed penetrator shell encountering just this effect. While deployed fins may make a round aerodynamically stable the de-spin action could cause an instability similar to that shown in Figure 3-28. Therefore it would be desirable to shorten this de-spin behavior as much as possible using over-sized fins or other active methods to reduce the spin rate.

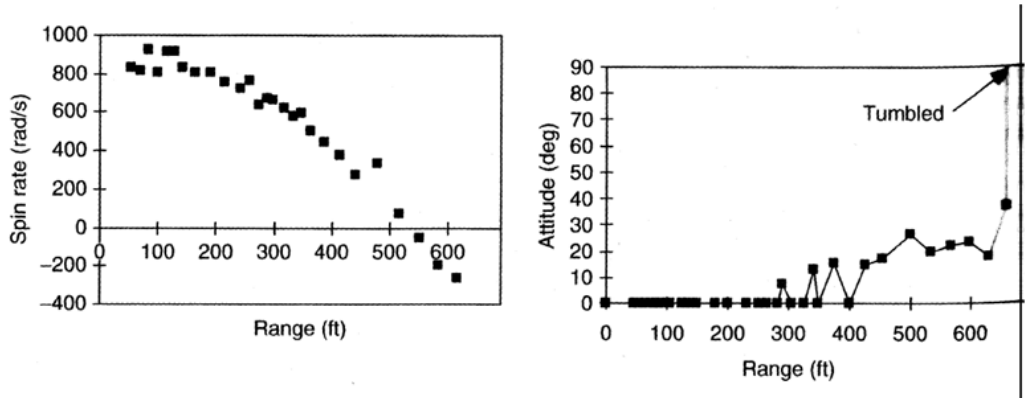

Figure 3-28: Instability and Dispersion Caused by Slowly Decreasing Spin Rate(Carlucci & Jacobson, 2008)

Unfortunately no passive de-spin system could be developed which would also guarantee a specified orientation within an acceptable time span. The correction to gliding condition must be achieved within a very few seconds to insure the round stays on-target and does not lose so much altitude that it could not reach its intended goal. All systems required an orientation sensor and control system. The Paparazzi autopilot system, created by Krashanitsa, et al., (2006) would be ideally suited to determine the spin rate and angle, as well as selecting the appropriate time to activate the de-spin mechanism. Paparazzi's suite of four IR sensors mounted around the radius of the round could directly collect spin rate information and provide bank angle data. Figure 3-29 shows the autopilot with the four infrared sensors as they would be arranged around the circumference of the fuselage.

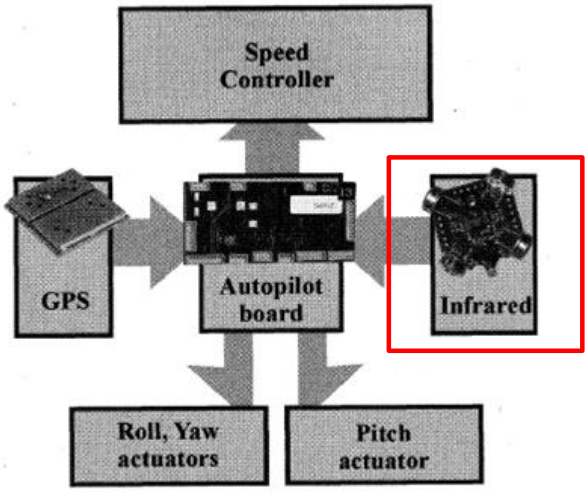

Figure 3-29: Paparazzi Autopilot Infrared Aerodynamic Angle Sensor System for Spin Orientation (Krashanitsa, Platanits, & Silin, 2006)

Simplest of the methods would to be to deploy three or four large, symmetric, delta wings around the body. These wings would be sized to provide lift for cruise flight and use active control surfaces on some or all as a mix of elevons and rudders as illustrated in Figure 3-30. The drag penalty incurred by the redundant wings would not act over much time and would therefore not impact range to a large degree. In addition, the lack of a preferred orientation means less time would be wasted while the aircraft seeks its upright position and pitches for lift. Finally, if the deployed configuration is lower drag than the stowed configuration the casing could be ejected and the wings deployed shortly after launch to gain an even greater range extension.

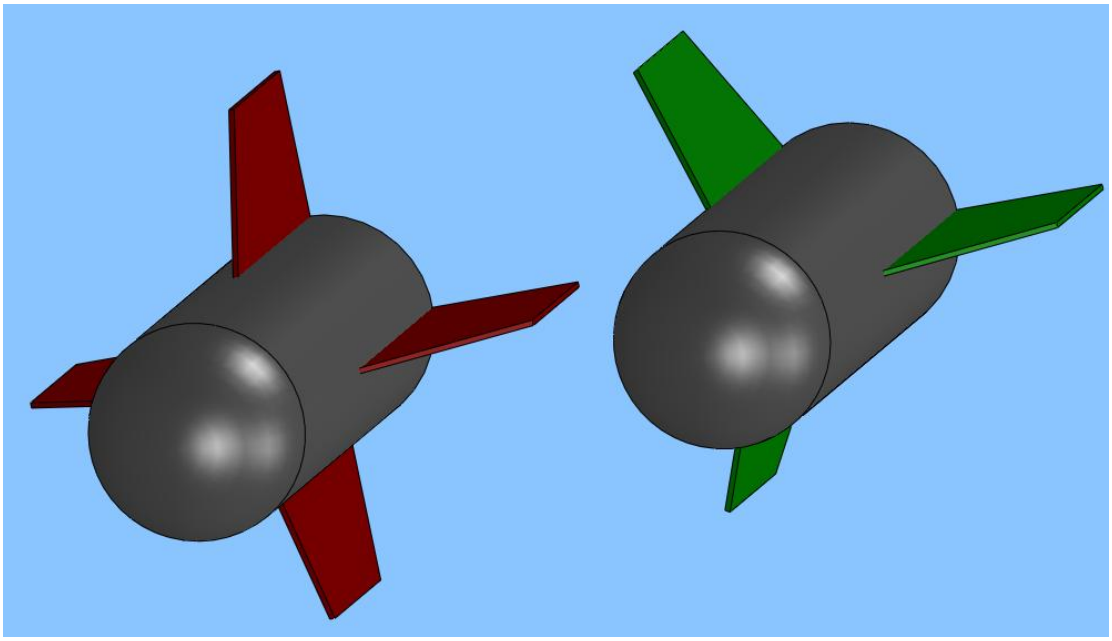

Figure 3-30: Cruciform Planform and Tri Planforms for Active Control Surface De-spin

Utilizing cambered airfoils, which significantly enhance performance, was a much more difficult problem. A cambered wing, with its single functional orientation, must be within a tight range of attitudes when deployed. Therefore the de-spin mechanism control and timing must be much more precise. A two stage process is recommended. Several options are shown in Figure 3-31. First, as discussed earlier, the main wing could have variable deployment: an initial opening identical to the vertical surfaces, followed by the full opening when the MAV has de-spun and the correct orientation has been reached. Second, a set of main wings would be deployed in addition to the de-spin tail fins. Third, a set of symmetrical de-spin fins would be deployed from the aft casing. Once the spin rate has dropped to the point that one half-revolution of the fully deployed main wings would damp out the rotation the casing, and de-spin fins, would be ejected and the main wings deployed. Strong dihedral stability would then complete the self-righting process. Rotating the main wings up about the longitudinal axis (dihedral) creates a vertical lift component imbalance when the aircraft is at a bank angle. The wing on the side the craft has rotated to has a larger vertical lift component than the one on the other side which creates a restoring roll moment. With careful design this method could also be applied to the wrapped membrane structure.

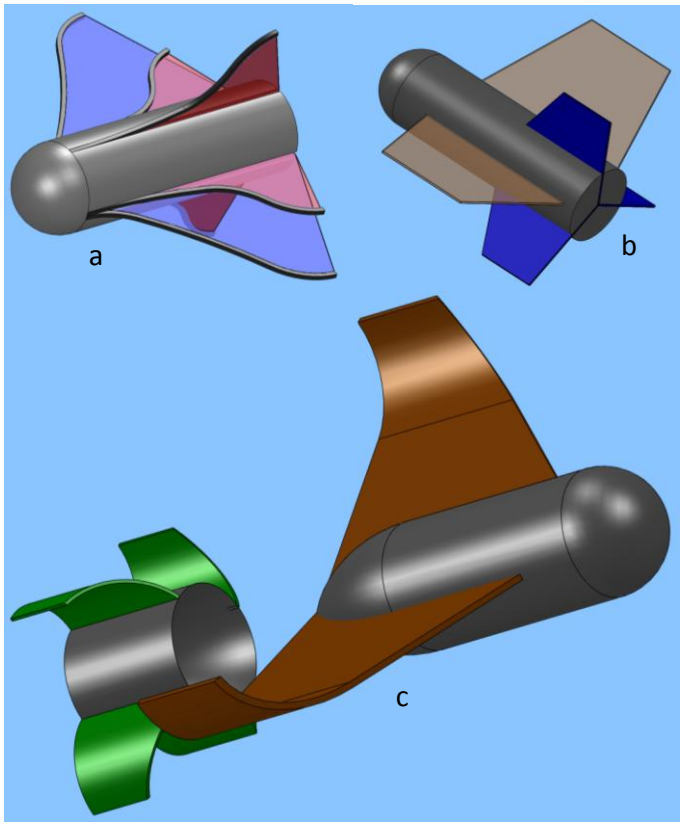

Figure 3-31: Multi-Stage Fin Deployment Schematic; a) Stabilizer Fins Deploy Further as Lifting Surfaces, b) Additional Lifting Surface Deploy, c) Stabilizers Deploy, De-Spin, and Discard Prior to Main Wing Deploy

Finally, as shown in Figure 3-32, the casing components could be ejected with high tangential velocity in the direction of spin. This would carry significant rotational momentum since the rear casing must be somewhat massive to withstand explosive launch forces. Fortunately this idea would be compatible with all structural concepts.

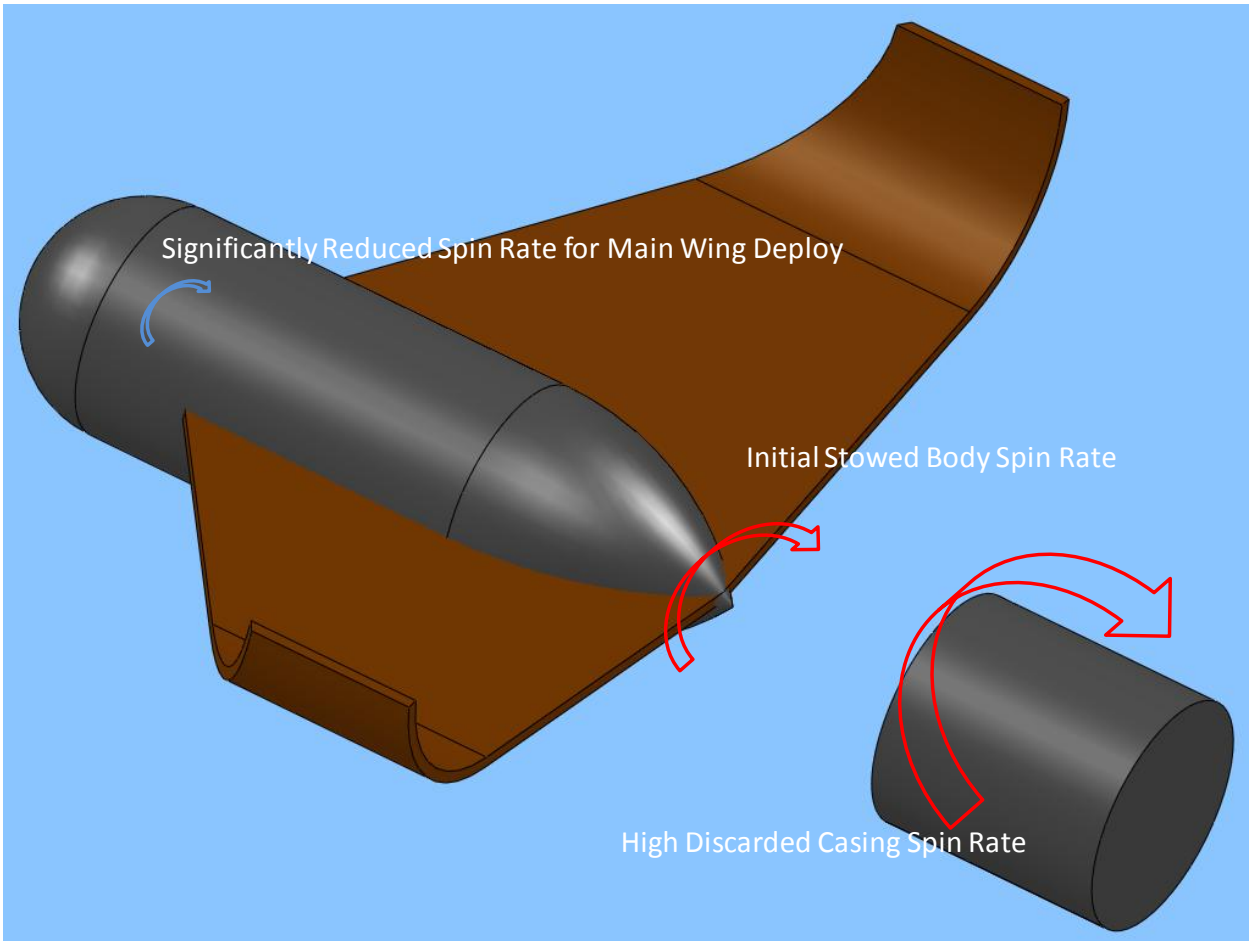

Figure 3-32: Casing Ejection in Spin Direction with High Rotation Rate to Reduce MAV Rotation Rate

Chapter 4 Initial Surface Sizing Calculations

The US Air Force Air Vehicles Research Directorate has been developing and improving Missile DATCOM (MDCOM), a semi-empirical code for the analysis of finned projectiles, for several decades. MDCOM was used to quickly test a large assortment of fins and wings applied to a generic fuselage. An initial survey of this type was necessary to begin restricting the design space. The code requires a text input file listing fuselage, wing, tail, and protuberance geometry parameters as well as flight conditions. A sample code used for this project incorporating both main wing and tails has been included in Appendix A with the associated output. The 1997 Fortran 90 version user's manual was a necessity due to the black-box nature of the executable file [20]

This semi-empirical code has been developed by the US Air Force to provide a first-cut estimation of aerodynamic coefficients for both gyroscopically and fin stabilized projectiles. Since access to this convenient program was available it was used to perform all initial sizing calculations. While not built for low Reynolds number work analytic and empirical relationships are exactly the classical aerodynamic theory used by all MAV design teams on their initial work[21].

Initial work assumed a constant 29 *mm* chord cruciform tail with trailing edges coincident with the aft end of the fuselage. Tail fin span was incremented from zero to 125 *mm* by 25 *mm* increments to find the optimum. A 50 *mm* long Ogive tail cone was imposed in addition to the hemispherical nose on the 40 *mm* diameter body as in Figure 4-1. An Ogive tail was imposed in an initial attempt to reduce the massive drag producing recirculation region behind the blunt tail of the stowed geometry. Three different locations for the center of gravity (CG) were examined, beginning 32.5 *mm* aft of the nose and moving to 66.5 *mm* aft, 50% body length. Additional information from the research sponsors fixed the CG location at the rearmost of the locations examined. Flight velocity was assumed to be the apex velocity of the given 45^{o} launch trajectory, 44 *m/s*.

[20] (Blake, Missile DATCOM User's Manual - 1997 FORTRAN 90 Revision, 1998)
[21] (Mueller, Torres, & Srull, Elements of Aerodynamics, Propulsion, and Design, 2006)

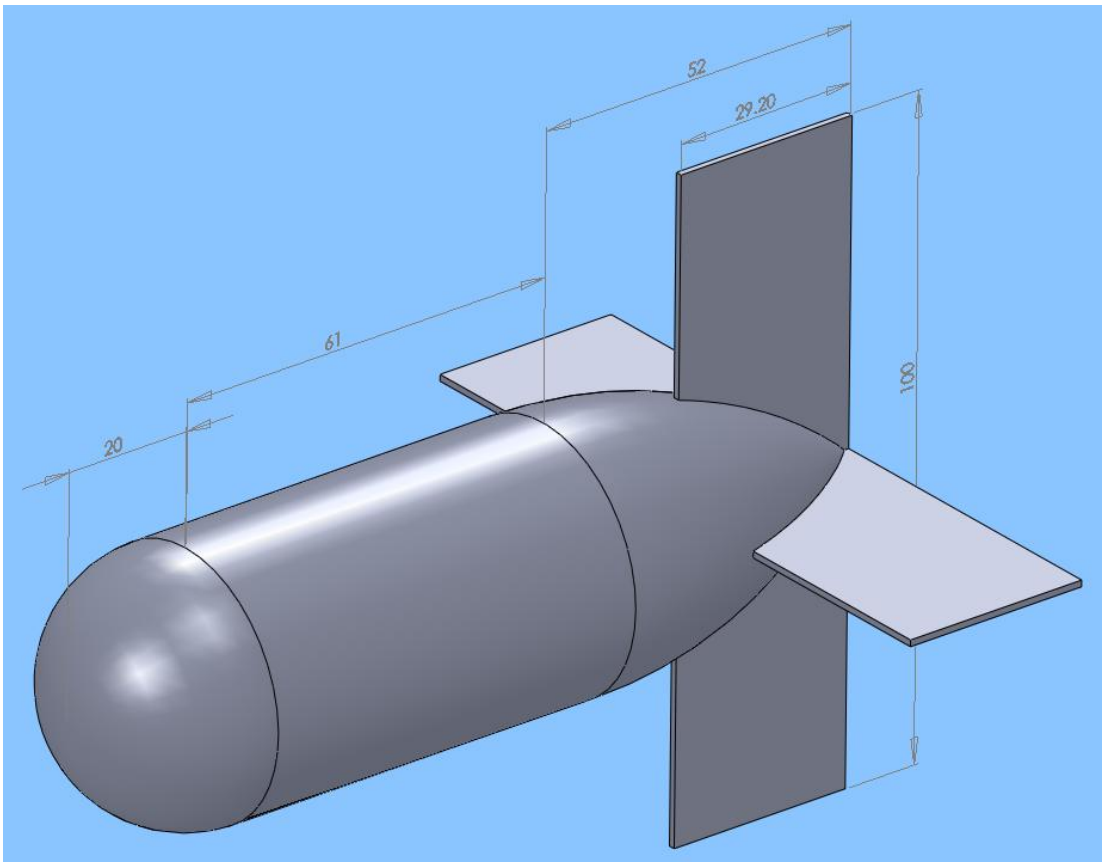

Figure 4-1: Fuselage and Tail Configuration Studied with MDCOM, Dimensions in *mm*

Figure 4-2 presents the results of this study showing a near linear reduction in pitching moment coefficient with angle of attack when tail span exceeded 50 *mm*. Linear interpolation between these points for a center of gravity conservatively located far aft, at 50% of the stowed geometry body length, provided sufficient information to estimate a stable tail surface area. A tail span of 60 *mm*, not including the fuselage diameter, was calculated to give a pitching moment coefficient of -0.017 per degree as recommended in *Aircraft Design: A Conceptual Approach*[22]. Since an extremely stable platform was desired values recommended for transport aircraft seemed a good starting point. Smaller surfaces would not pose a design problem as the span could simply be truncated. This was not true for enlarging the surfaces. For all future work the projected tail area, not including the fuselage as customary in projectile design, was fixed at 1,740 mm^3 for both horizontal and vertical surfaces. Work then moved to initial main wing sizing.

[22] (Raymer, 2006)

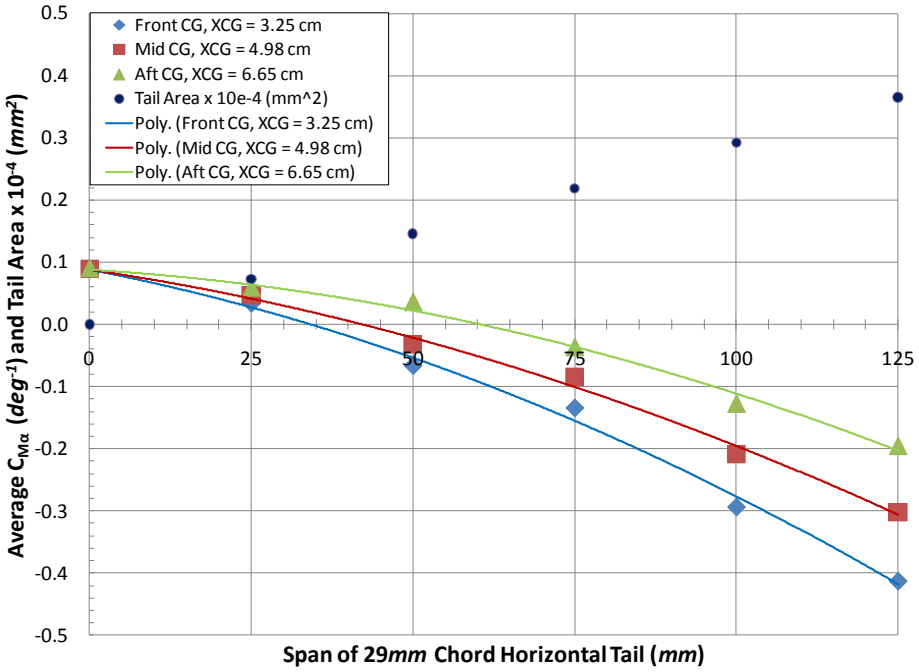

Figure 4-2: Tail Sizing Sensitivity Study with Three CG Locations

Wing sizing was done in a similar manner to tail sizing. A 36.5 *mm* chord main wing of varying span was placed with its quarter chord at the center of gravity, 62.5 *mm* aft of the nose. The tail was then rotated by 45^{o} to reduce interference issues, as shown in Figure 4-3. An extreme rearward location was required due to the fixed far aft CG location. A NACA 0008 airfoil was selected and simulations were done with the body at four angles of attack. Figure 4-4 presents the results of the analysis.

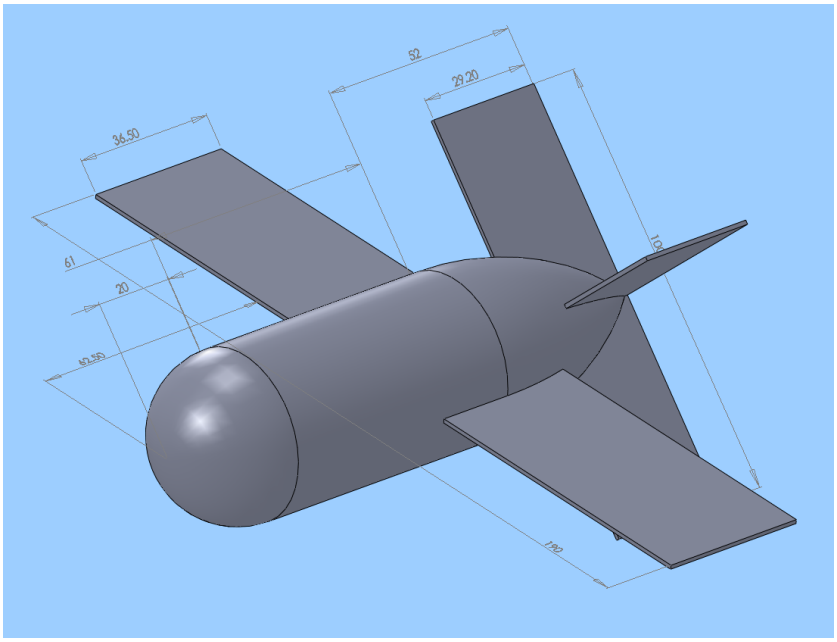

Figure 4-3: Complete Planform Studied with MDCOM, Dimensions in *mm*

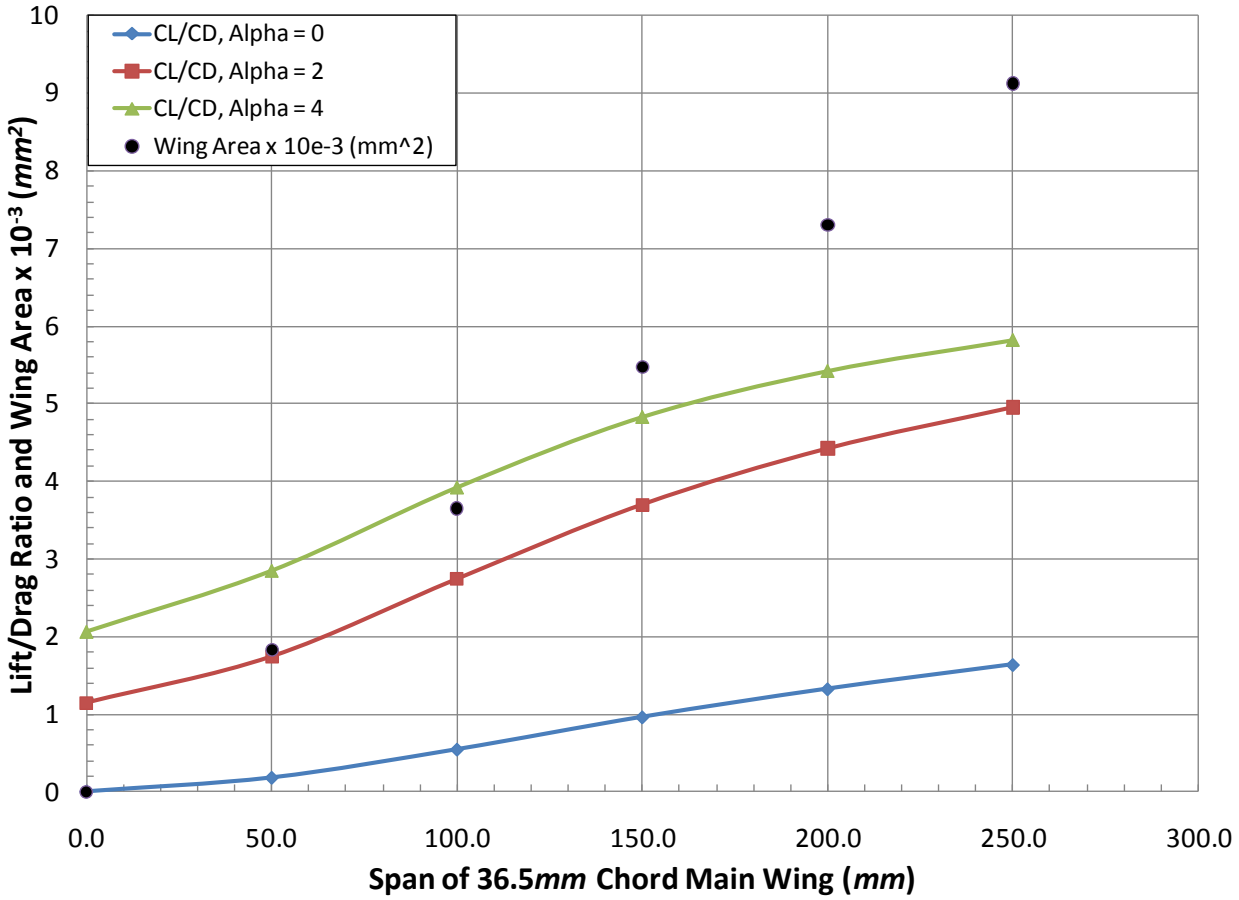

Figure 4-4: Main Wing Sizing Sensitivity Study

Figure 4-4 shows the near linear increase in lift-to-drag ratio with increasing wing area for a NACA 0008 airfoil mounted to the fuselage at 1^{o} angle of attack relative to the body. Data for the wing-body-tail combination is presented for three different angles of attack. Based on this information a wing area of 5,500 mm^3 was selected, corresponding to a span of 150 *mm*. This more than satisfied performance requirements with a 5:1 predicted lift-to-drag ratio. Structural stowage concepts were checked to insure that this wing was feasible.

Chapter 5 Preliminary CFD Analysis

Initial CFD work began with studying the stowed, or baseline, geometry, presented in Figure 5-1. This was done to insure that the baseline experimental data for the geometry could be reproduced, and to provide a starting point for the selection of optimal solver settings and mesh parameters as work progressed to more complex geometry. Both conventional high aspect ratio and truncated delta wing concepts were then analyzed for the first planform down-select.

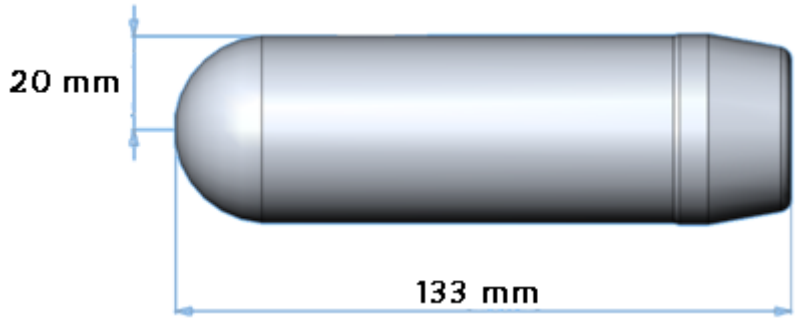

Figure 5-1: Stowed Geometry

5.1 Stowed Geometry Mesh Generation

The sponsors were familiar with the aerodynamics of the baseline configuration, and the associated CFD simulation of such geometries. A suite of recommended solver settings was provided as shown in Table 5-1 along with recommended domain sizes based on the cylindrical stowed body diameter. With these settings and the domain shown in Figure 5-2 the drag coefficient was predicted to within from the CFD simulation. Main body axial, dx, cell lengths of 2.0 *mm* were used, with a step down to 0.5 *mm* spacing at the tail. Five prismatic cell layers were grown up from the wall with a first height of 0.5 *mm* and a growth rate of 1.2. Outside the prismatic region a tetrahedral domain was created, again with a cell growth rate of 1.2. Specific details on the mesh generation parameters are provided in Appendix B.

Table 5-1: Sponsor Recommended Solver Settings and Domain Sizes With WVU Selected Solver Settings

Domain Geometry:		
Characteristic Length:	Body Diameter (d_o = 40mm)	
Domain Shape:	Truncated Cone	
Reference Location:	Body Nose	
Upstream Length:	$50d_o$ = 2,000mm	
Upstream Diameter:	$25d_o$ = 1,000mm	
Downstream Length:	$100d_o$ = 4,000mm	
Downstream Diameter:	$50d_o$ = 2,000mm	
Boundary Conditions		
	High Mach	**Low Mach (WVU Developed)**
Inlet	Pressure - Far Field	Velocity Inlet
Outlet	Pressure - Far Field	Pressure Outlet
Body Surface	Wall	Wall
Solver Settings		
	High Mach	**Low Mach (WVU Developed)**
Time	Steady	Steady
Type	Pressure-Based	Pressure Based
Velocity Formulation	Absolute	Absolute
Turbulence Model	Standard k-ω	Standard k-ω
Energy Equation	On	Off
Discretization	Second Order	Second Order
Gradient	Green-Gauss Node Based	Green-Gauss Node Based
Precision	Double Precision	Double Precision
Reference Location	$49d_o$ upstream = -1,960mm	$49d_o$ upstream = -1,960mm
Initialization	Velocity = 0m/s, Pressure = 1atm	Velocity = 0m/s, Pressure = 1atm

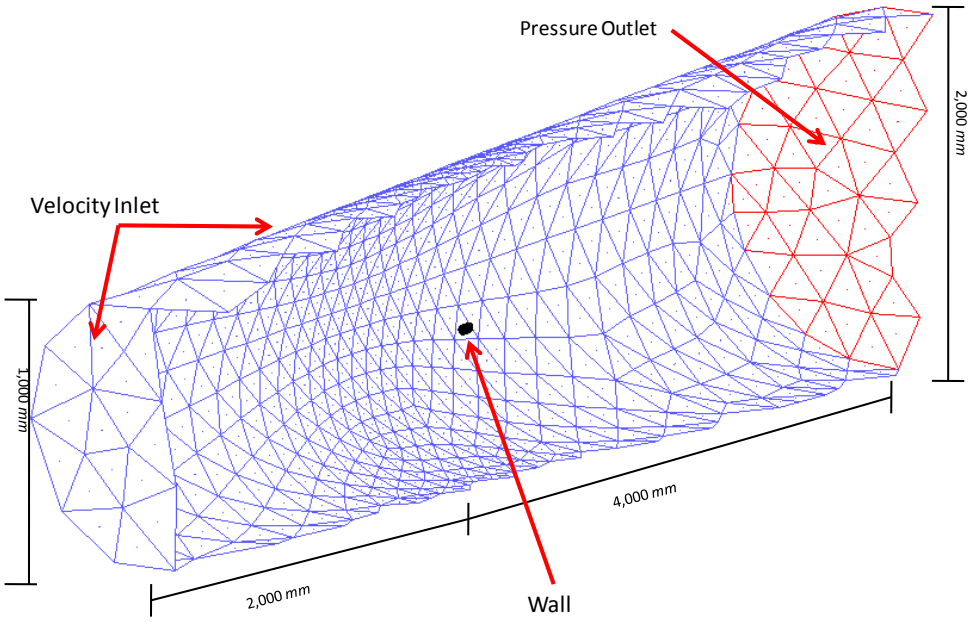

Figure 5-2: Solution Domain, Sliced on Longitudinal Centerline

Figure 5-3 shows the convergence obtained for the standard k-ω turbulence model which consistently under-predicted the drag value within acceptable limits, -7%. As seen in Figure 5-3 grid independence was reached with $2.7x10^6$ cells. A second run with the same mesh was conducted using the SST k-ω model. This shifted the error to +8%, still within acceptable limits for preliminary design work.

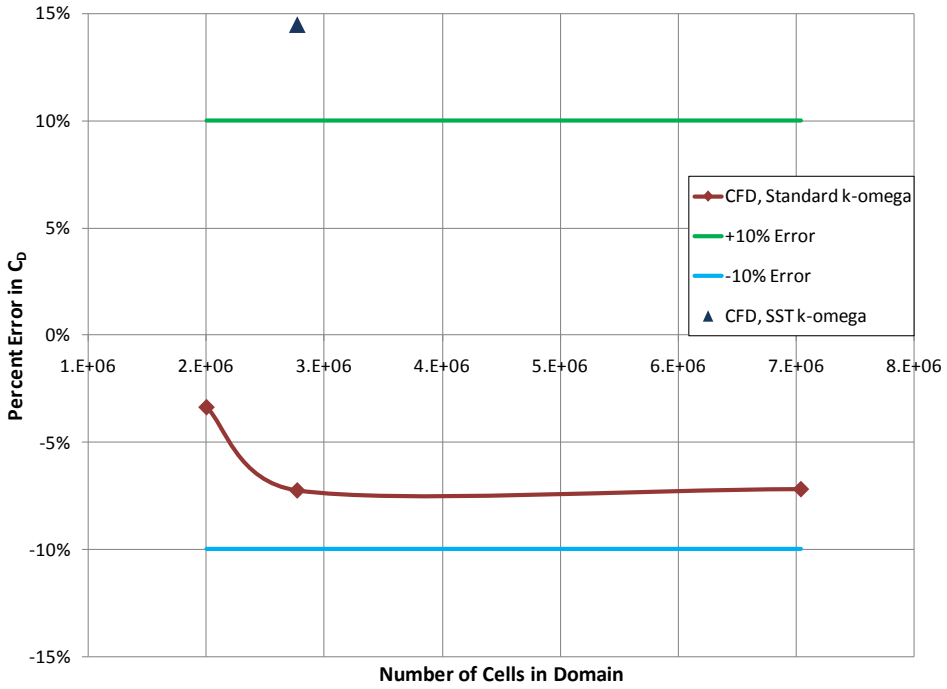

Figure 5-3: Convergence Plot for Stowed Geometry, Mesh Converged at $2.7x10^6$ Cells

5.2 Deployed Configuration Simulation

Once functional mesh and solver settings had been developed for the stowed configuration work moved to simulating the deployed configurations. Settings developed in the previous section were used as starting points for simulating the MAV geometry. Ogive tail cone fuselages, as detailed in Chapter 4, were used for the simulation of two configurations. Both a conventional planform based on the WVU Telescopic transformer, and a delta wing configuration were studied. Surface meshes were 1.5 *mm* spacing in large, low curvature regions, and condensed to 0.5 *mm* in complex regions such as the wing leading and trailing edges and wing-body junctions. This was done to match the on the stowed geometry discussed in Section 5.1, which provided an acceptable match to experimental data. All other mesh and solver parameters were defined similarly. Figure 5-4 shows the surface meshes of both geometries.

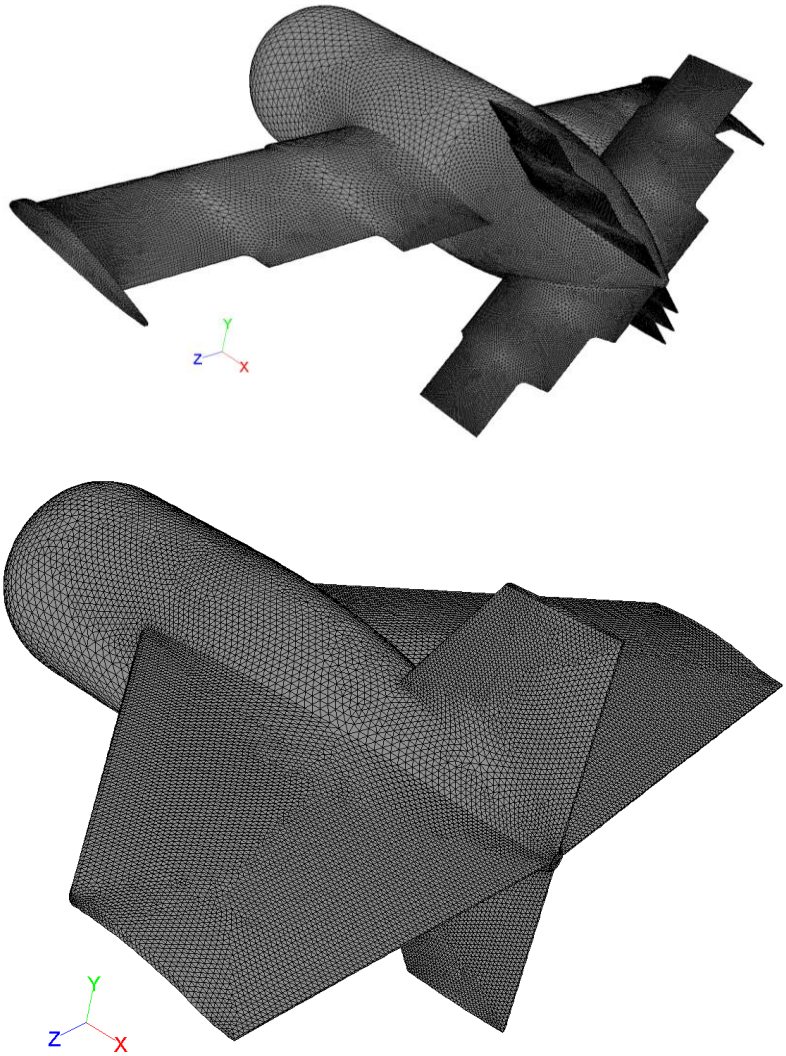

Figure 5-4: Initial Deployed Geometry Surface Meshes, Identical Vertical Tail Area and Main Wing Area, Identical Fuselages

While the conventional planform produced an acceptable lift-to-drag ratio of 4:1, the delta planform exceeded it by 100% with a L/D of 8:1. Both had the same wing area, angle of attack, and vertical tail area, mounted to identical fuselages. This huge difference was caused by two phenomena. First the interference between the main wing and tail on the conventional layout as clearly seen in Figure 5-5. The complex vortical structures starting aft of the main wings and becoming denser at the tail significantly increase drag on the MAV. While some of these structures still exist on the delta wing configuration they are smaller and fewer, therefore generating less drag. Second, as discussed in Section 2.3.2, the increased chordwise Reynolds number of the delta planform increased the performance of its airfoil far in excess of the induced drag penalty incurred by a low aspect ratio. Therefore delta planforms were selected for all optimization work. This down-select was also fortuitous from a structural standpoint. The delta wing would be far easier to create than the conventional layout primarily due to the elimination of two wing surfaces by removing a horizontal tail. In addition, at these small scales the larger structures will likely be easier to build.

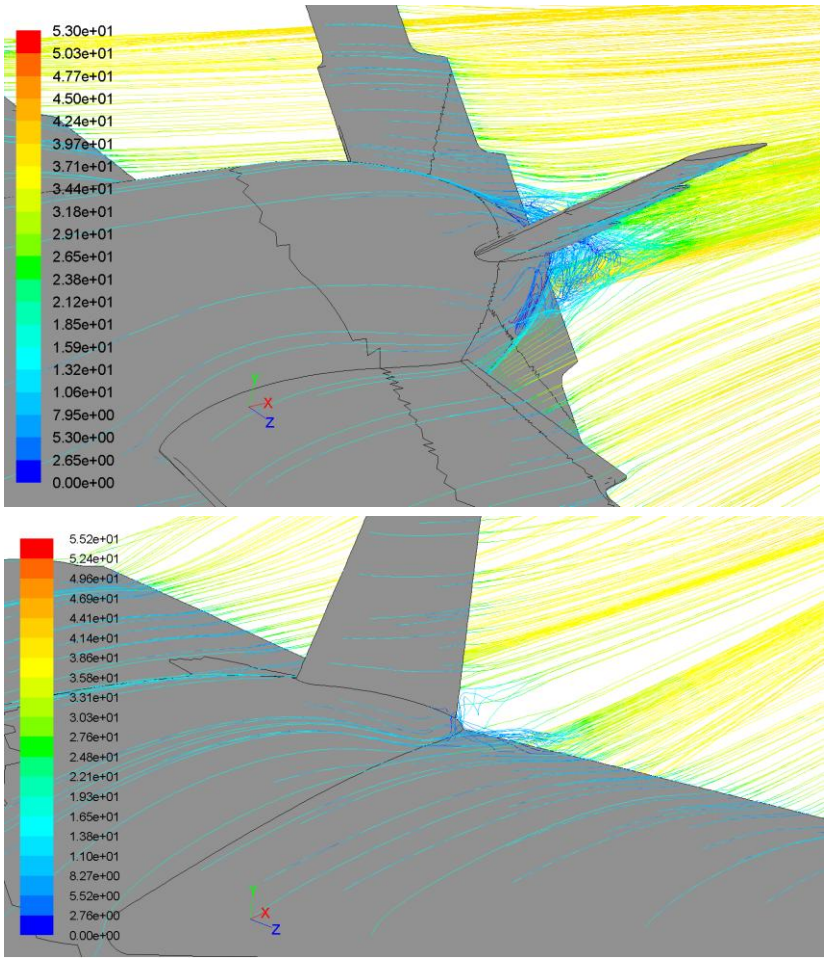

Figure 5-5: Comparison of Flow at Tails of Conventional and Delta Planforms, Pathlines Colored by Velocity, (*m/s*), Jagged Black Lines Are Artifacts From Geometry Contour Display

Chapter 6 Classical Aerodynamic Optimization Analysis

It was possible that more optimal MAV designs or other missions could be discovered by using a launch angle other than the initially specified 45°. Therefore, a basic optimization analysis was performed using classical ballistics and aerodynamics. A simple MATLAB code was written to calculate launch velocity from the known data presented in Table 6-1. Once the launch velocity was known an array of apex altitudes and velocities were determined using a second in-house program. This study was conducted to provide initial gliding altitudes an velocities (apex altitude and velocity) as a starting point to optimize for maximum range. An increased lift-to-drag ratio at a lower velocity could provide a greater range by starting from a significantly higher altitude. All codes discussed in Chapter 6 have been included in Appendix C.

Table 6-1: Given Stowed Trajectory Data and Calculated Launch Velocity

Given Trajectory Data		
Drag Coefficient	0.133	
Range	450	*m*
Launch Angle	45	*deg*
Apex Velocity	40	*m/s*
Flight Mass	180	*g*
Calculated Data		
Laucnh Velocity	71.32	*m/s*

Calculated Apex Information			
Launch Angle (*deg*)	Apex Altitude (*m*)	Apex Velocity (*m/s*)	Apex Range (*m*)
45	124.2	45	233.9
55	162.5	37	222.9
65	193.8	28	181.2
75	215.3	18	118.4
85	116	6	41.2

Results of the trajectory program for launch angles, Λ_{launch}, of 40, 60, 70, and 80 degrees are presented in Figure 6-1. From this point on apex velocity, V_A, and optimum MAV glide velocity are considered to be identical. In addition, note that increasing launch angle reduces cruise velocity, increases starting glide altitude, and, by basic aerodynamics, increases optimum cruising wing area.

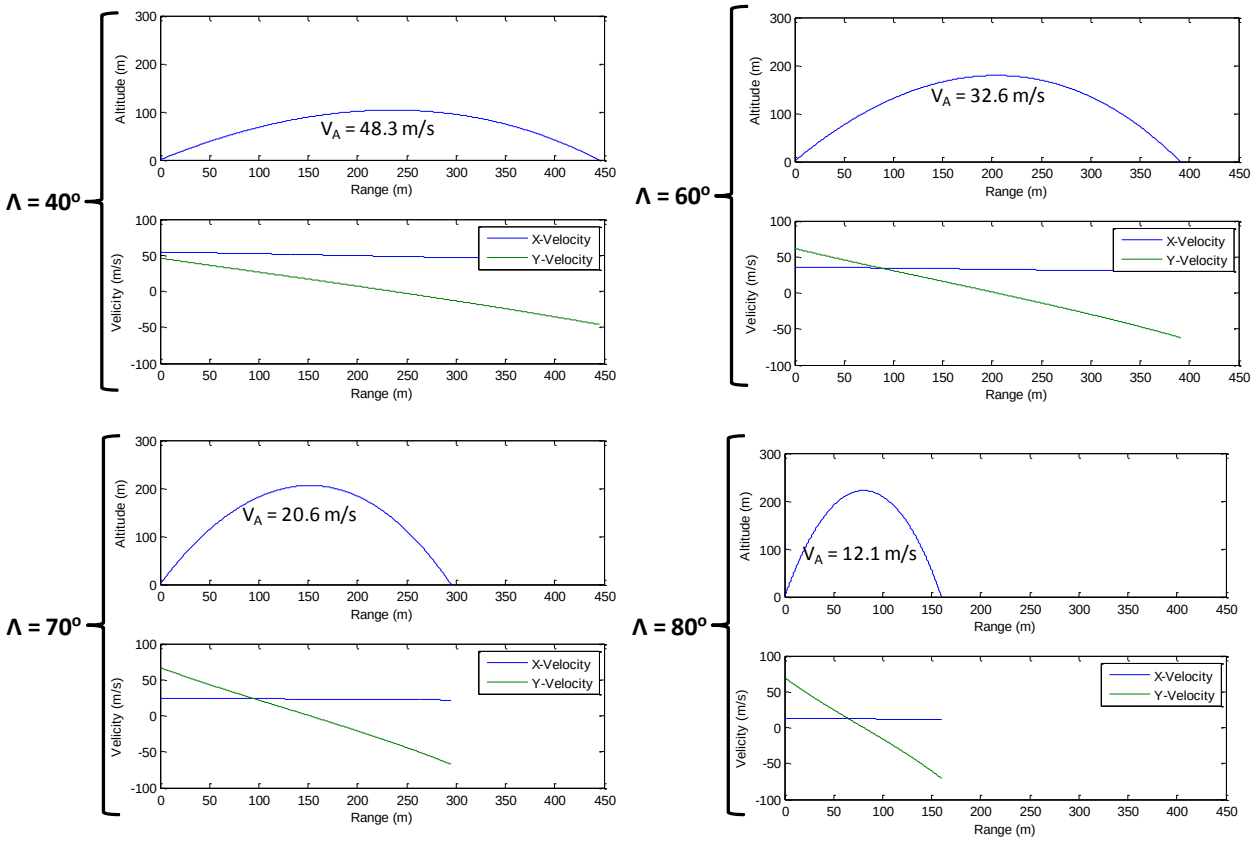

Figure 6-1: Effect of Varying Launch Angle for AR = 2 Wing on Cruise Velocity and Initial Gliding Altitude

Once the precise effects of launch angle on cruise velocity and apex altitude were known a third code was written. This algorithm calculated an optimum main wing area of specified planform, located the wing on the fuselage such that no horizontal tail was necessary, and proceeded to calculate expected range and flight time. In the cases detailed in Table 6-2 the main wing was fixed at an aspect ratio of 2 with a taper ratio of 0.5. Similar sets of data were generated for aspect ratios from 1 to 4. All other values were calculated as illustrated by the program flowchart provided in Figure 6-2.

Table 6-2: Results of Optimization Code for an Array of Launch Angles

Launch Angle	(deg)	40	45	50	55	60	65	AR	2
Apex Altitude	(*m*)	103.8	124.2	143.9	162.5	179.2	193.8	Λ_{LE} (*deg*)	30
Apex Velocity	(*m/s*)	48	45	41	37	33	28	λ	0.5
Apex Range	(*m*)	236	238.3	233.9	222.6	204.9	181.2	t/c	0.1
Total Range	(*m*)	659	798	1,004	1,256	1,498	1,914	$c_{t/c}$	0.4
%+ Range		146%	177%	223%	279%	333%	425%		
W/S	(N/m^2)	700	600	450	325	250	150	X_{CG} (*mm*)	80
Wing Area	(cm^2)	25.23	29.43	39.24	54.33	70.63	117.72		
L/D		4.07	4.51	5.36	6.35	7.2	8.94		
Re_{MAC}		121,020	122,550	128,930	136,910	143,450	152,510		
$X_{CR\ LE}$	(*mm*)	68.4	67.5	65.6	63	60.6	55		
c_R	(*mm*)	47.4	51.1	59.1	69.5	79.2	102.3		
c_T	(*mm*)	23.7	25.55	29.55	34.7	39.6	51.15		
b	(*mm*)	71	76.7	88.6	104.2	118.9	153.4		
α_{trim}	(deg)	7.4	7.14	6.17	5.14	4.41	3.56		
L/D Wing		7.04	7.64	8.99	10.43	11.14	13.05		

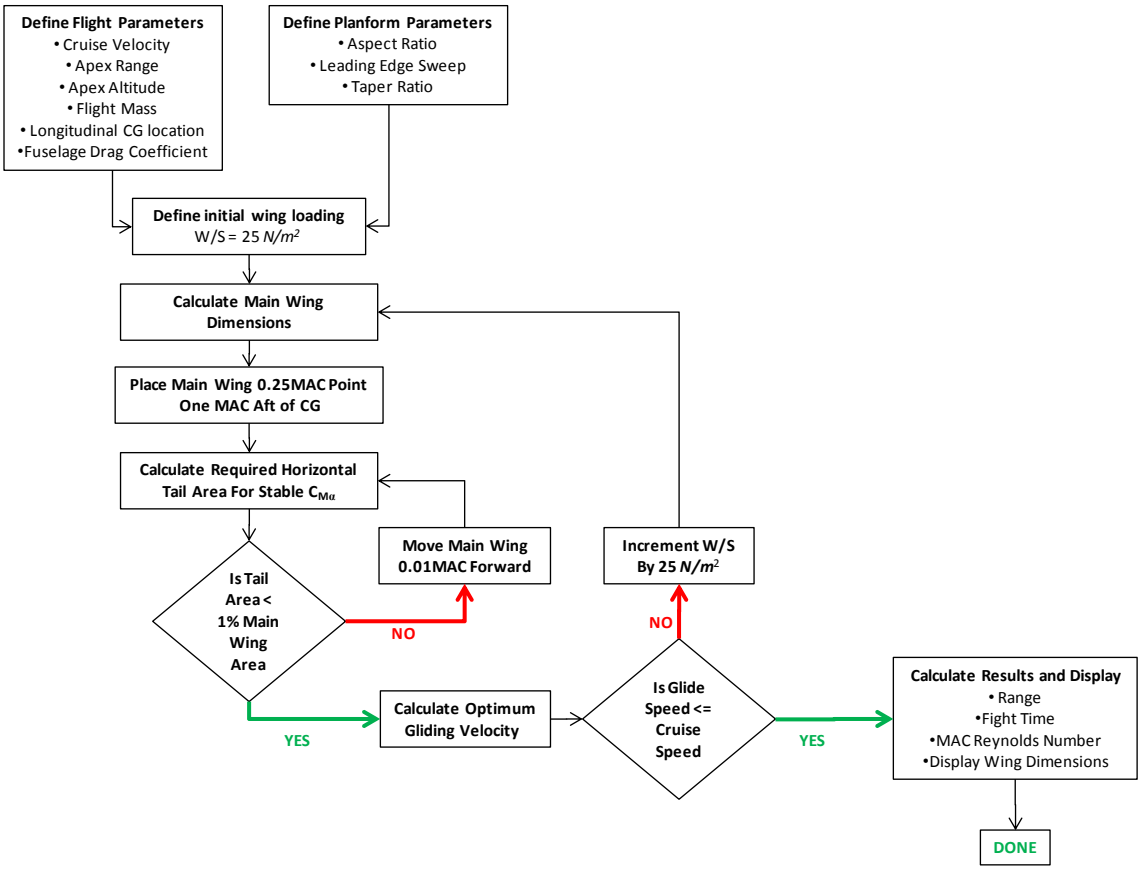

Figure 6-2: Optimization Code Flowchart

Figure 6-3 presents the most important results from this process, clearly illustrating the significant range extensions possible with increased lift-to-drag ratio from greater launch angles. The increased efficiency possible with larger wings at lower velocities coupled with the greater initial glide start was far more important to maximum range than obtaining the maximum down-field distance at apex.

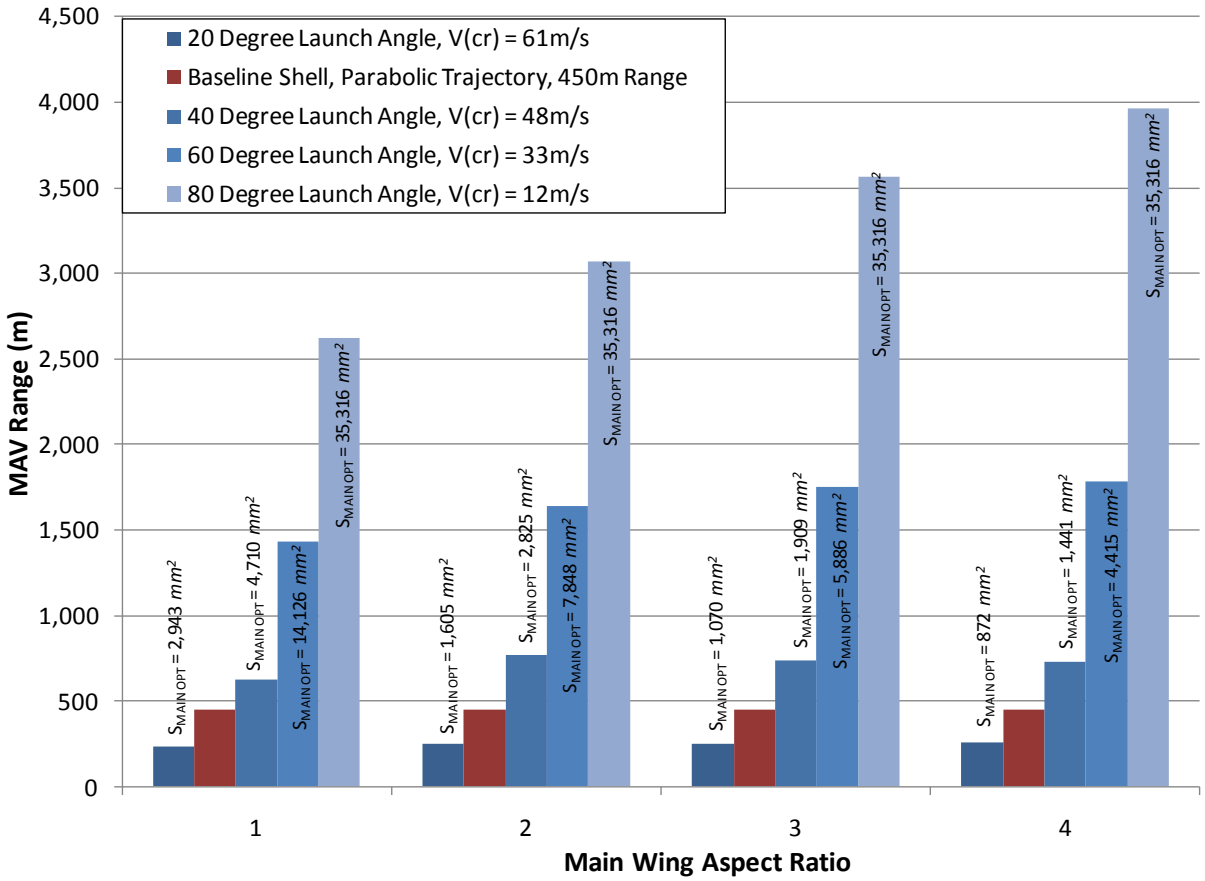

Figure 6-3: Comparison of High Speed, Low Angle Launch and Low Speed, High Angle Launch Missions

Based on the results from Figure 6-3 the idea of two divergent mission plans was developed. The simplest route was to achieve the minor range extension originally specified from a 45^{o} launch angle with high cruise speed and very small wings. Alternately, and more difficult, a high 60^{o} to 80^{o} launch angle would produce ranges on the order of 2,000 *m* and extremely long flight times when coupled with large wings. Figure 6-4 compares the two mission profiles and Figure 6-5 shows the wing areas required to accomplish them, along with the stowed geometry as a size reference.

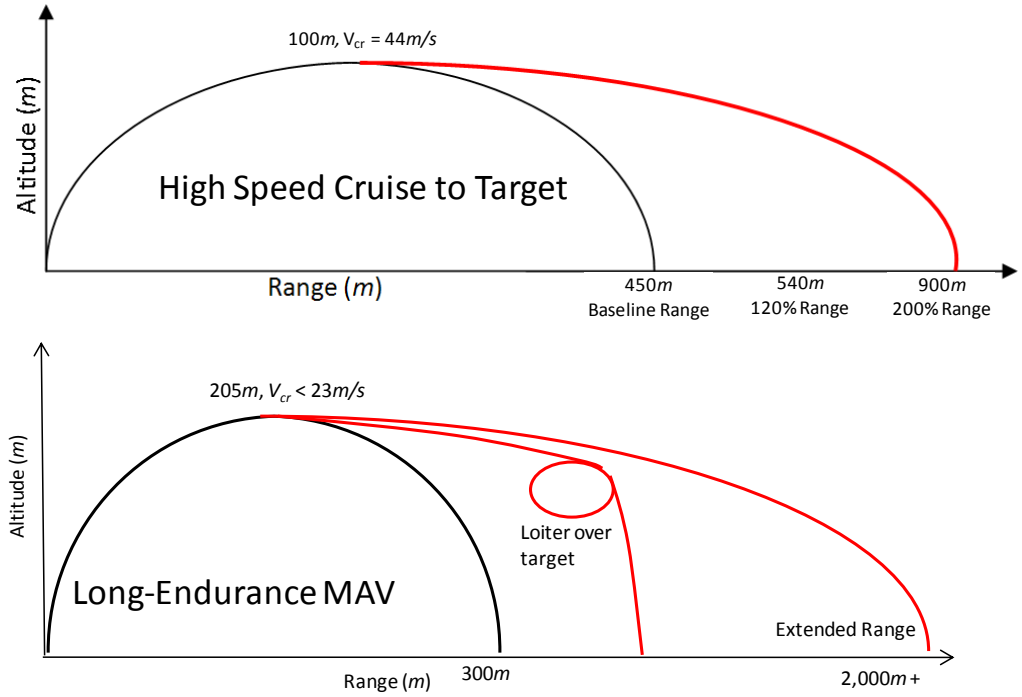

Figure 6-4: Comparison of Alternate Mission Plan Required Wing Areas, Dimensions in *mm*

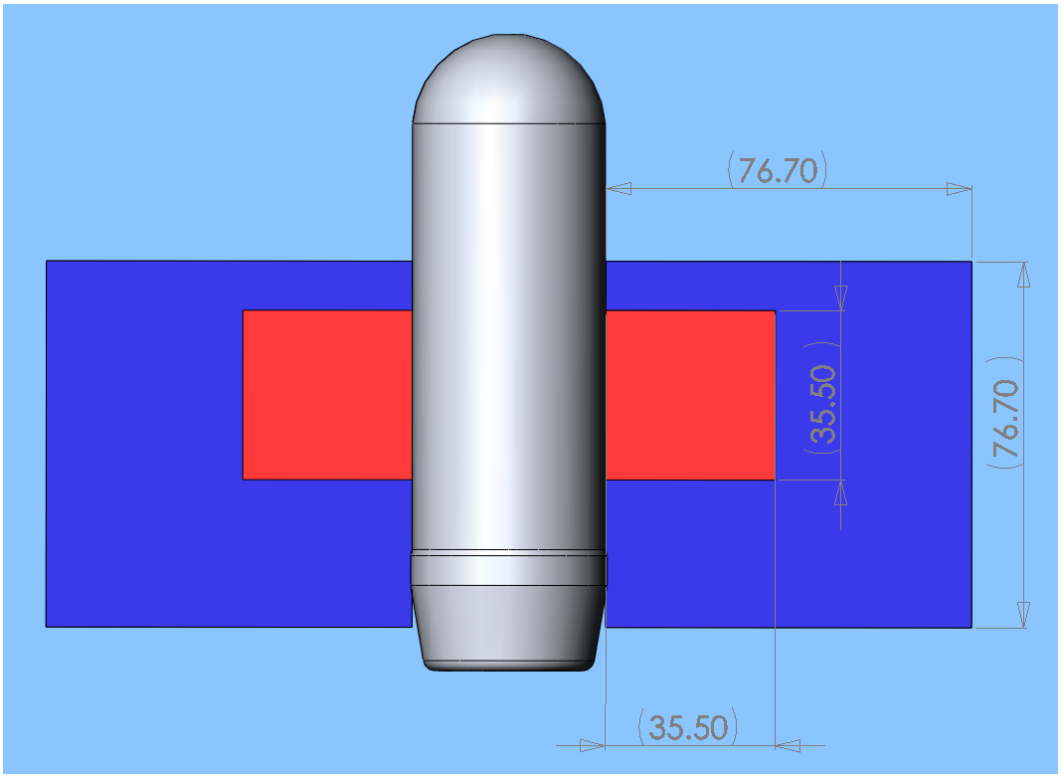

Figure 6-5: Comparison of Required Wing Area for High-Speed Cruise (Wing Loading (*W/S*) = 700 N/m^2, V_{cr} = 48 *m/s*, *S* = 2,523 mm^2) and Long Endurance Missions (Wing Loading (*W/S*) = 150 N/m^2, V_{cr} = 20 *m/s*, *S* = 11,772 mm^2) Relative to Stowed Geometry

The low flight speed option would be best suited to a surveillance role while the high speed variant would provide rapid, maneuverable, extended delivery. A compromise design would be a poor choice since it would require a more complex wing system than the high-speed variant and would fly much too fast for surveillance with insufficient duration. MAVs for surveillance tend to operate between 10 *m/s* and 20 *m/s* to provide useful time-on-target without having to frequently re-orient the viewpoint.[23]

With the decision to pursue two alternate missions the comparison to current MAV and UAV designs was re-considered. Figure 6-6 presents a modified version of Figure 2-3 with the two missions indicated. Neither is within the normal regime, and the high-speed version is not similar to any other current designs.

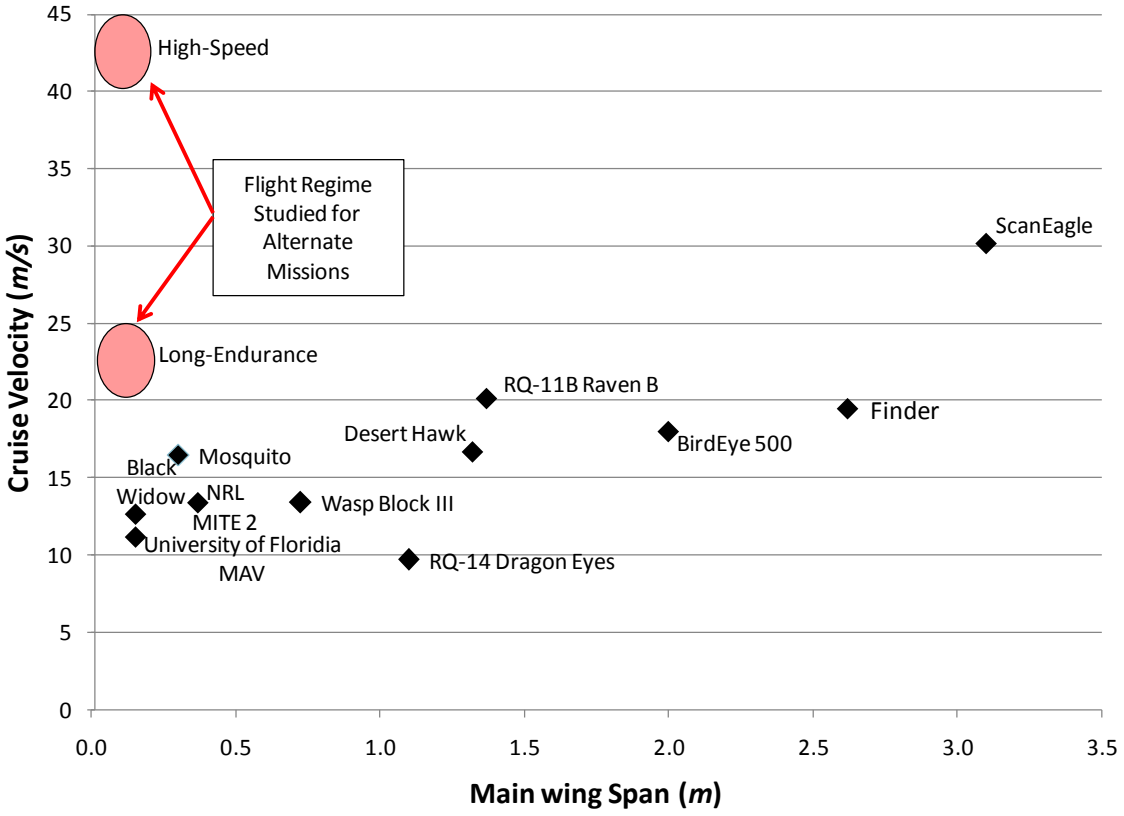

Figure 6-6: Comparison of WVU Stowable UAV Flight Regimes for High-Speed and Long-Endurance Missions to Current UAV and MAV aircraft

[23] (Davis, Kosicki, Boroson, & Kostishack, 1996)

Fuselage drag effects on range were also considered. Since the fuselage drag coefficient was a single specified value in the code it was trivial to vary between 0.2, based on fuselage frontal area, a worst-case scenario for a fuselage generating more drag than the stowed geometry, and 0.05 for an impossibly low drag configuration. Resulting ranges were predicted for both large and small wing designs as shown in Figure 6-7. As expected the percent increase in range from a lower fuselage drag coefficient was greater with the larger wing. This was due to the increased flight time over which the drag had an effect. In both cases the reduction of fuselage drag coefficient would be limited by required fuselage volume. The optimum range-volume selection cannot be made until a much more complete systems design is available.

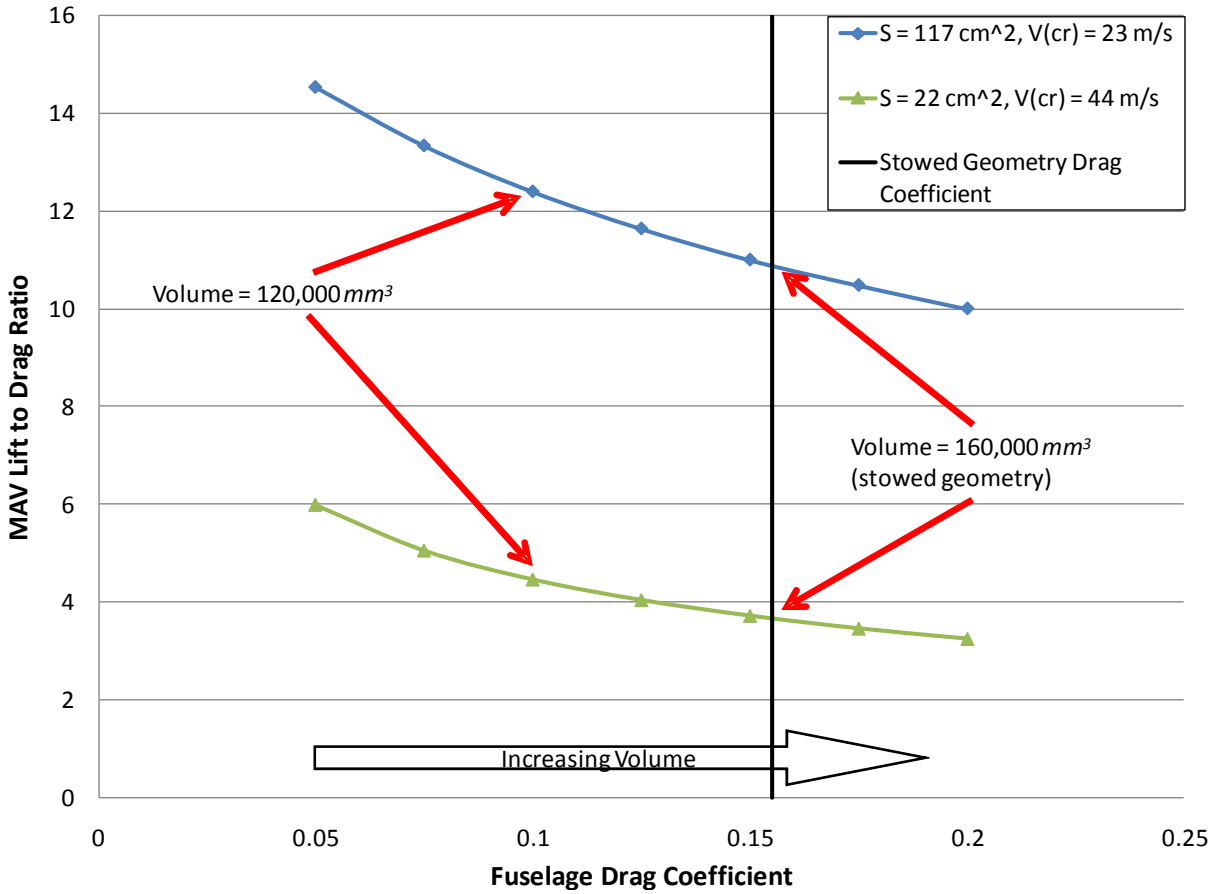

Figure 6-7: Lift-to-drag Ratio Sensitivity to Fuselage Drag Coefficient

Chapter 7 Component CFD Analysis

To simplify the parametric numerical analysis the aircraft was broken down into sub-components. Fortunately this could be reduced to a pair of major segments, the fuselage and a wing which, over a range of Reynolds numbers and with a symmetric airfoil, would provide data for both the main wing and vertical tail. Mesh independence analyses for each of the sub-components were conducted to provide starting points for full MAV studies to be conducted in the future. This also allowed a more in-depth exploration of Fluent's ability to predict low Reynolds number airfoil performance. A detailed summary of the Fluent solver settings used in this work is provided in Appendix D.

7.1 Fuselage Analysis

From the classical aerodynamics work presented in Chapter 6 it was apparent that the fuselage was the largest drag contributor. Therefore any possible fuselage drag reductions would have large effects on overall MAV performance. As illustrated in Figure 7-1 a pair of Ogive tail cones were "carved" from the stowed baseline geometry. The Ogive geometries are referenced by the corresponding length of straight cylinder: 30 and 45 *mm*. Mesh and solver settings identical to those used for the stowed geometry, presented in Figure 5-2 and Table 5-1were applied. Streamlining the fuselage in this manner cost 35,000 mm^3 with the 45 *mm* long body and 45,000 mm^3 with the 30 *mm* body.

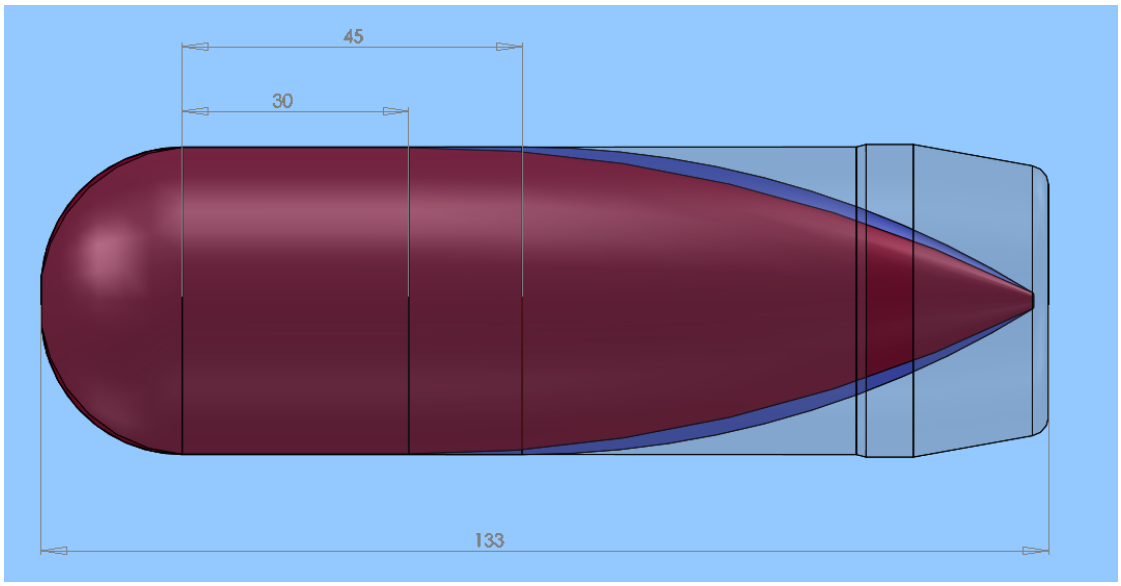

Figure 7-1: Various Ogive Tail Cones Applied to Stowed Geometry for Fuselage Study, Dimensions in *mm*

Grid independence was obtained on the 45 *mm* long central body version (middle outline in Figure 7-1). Specific details on mesh sizing are provided in Appendix B. Figure 7-2 shows that a mesh-independent solution was reached at $7.5x10^5$ cells in the domain. The entire mesh was generated with triangular prisms on the body and tetrahedral cells in the main volume. Body cells were restricted to 2.0 *mm* on a side with a first cell height of 1.05 *mm*. A sample domain including local refinement regions and prismatic boundary layer is presented in Figure 7-3.

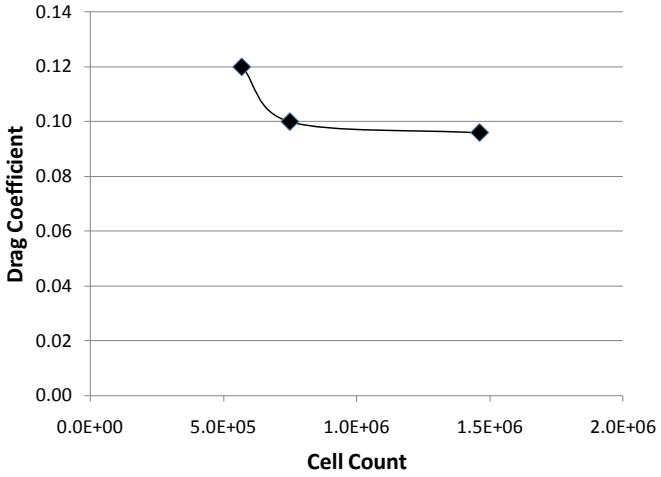

Figure 7-2: Mesh Independence Study for 45 *mm* Center Body Fuselage

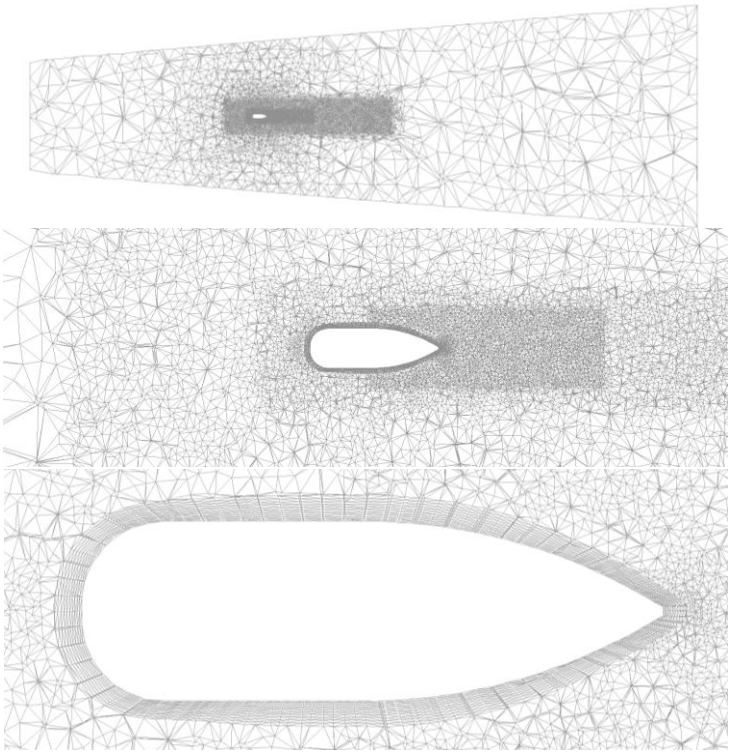

Figure 7-3: Component Mesh For Fuselage Analysis, 45 *mm* Center Body

With drag data collected and plotted in Figure 7-4 it was apparent that no peak "optimum" existed. Instead a case of diminishing returns was encountered. Maximum drag reductions of approximately 30% were possible, but significant fuselage volume was sacrificed. Since the case of diminishing returns in the drag-volume correlation was gradual it appeared that fuselage volume should first be dictated by mission payload, sensors, and controls. Only after the internal design is completed could the appropriate streamlining be selected.

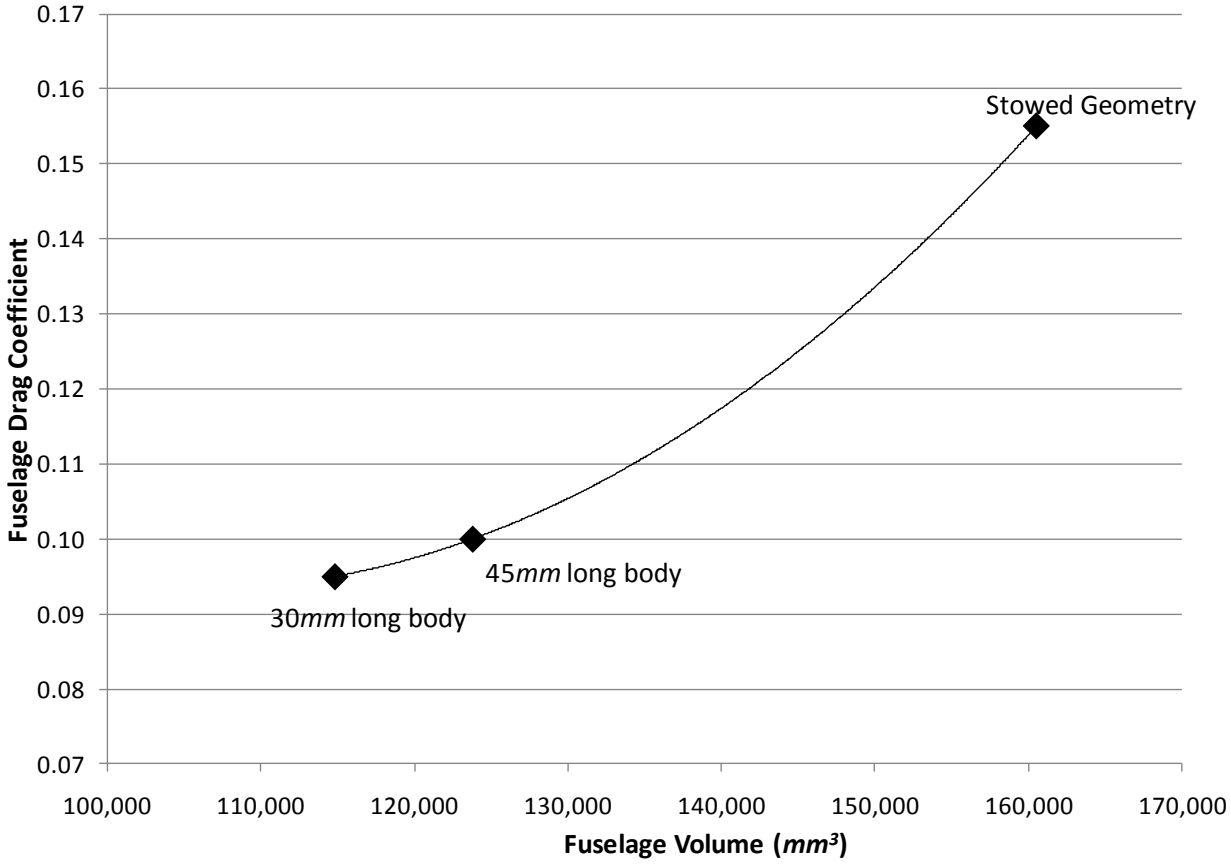

Figure 7-4: Correlation Between Fuselage Volume and Fuselage Drag Coefficient, Stowed Geometry is Far Right Value, Length of Tail Cone Increases to Left

7.2 Two Dimensional Low Reynolds Number Airfoil Analysis

As mentioned briefly in Section 2.3.1 flow over a two dimensional airfoil at low Reynolds numbers becomes extremely complex. The combination of laminar and turbulent regimes with possible flow separation and recirculating pockets, as shown in Figure 7-5, pushed the limits of commercial CFD software.

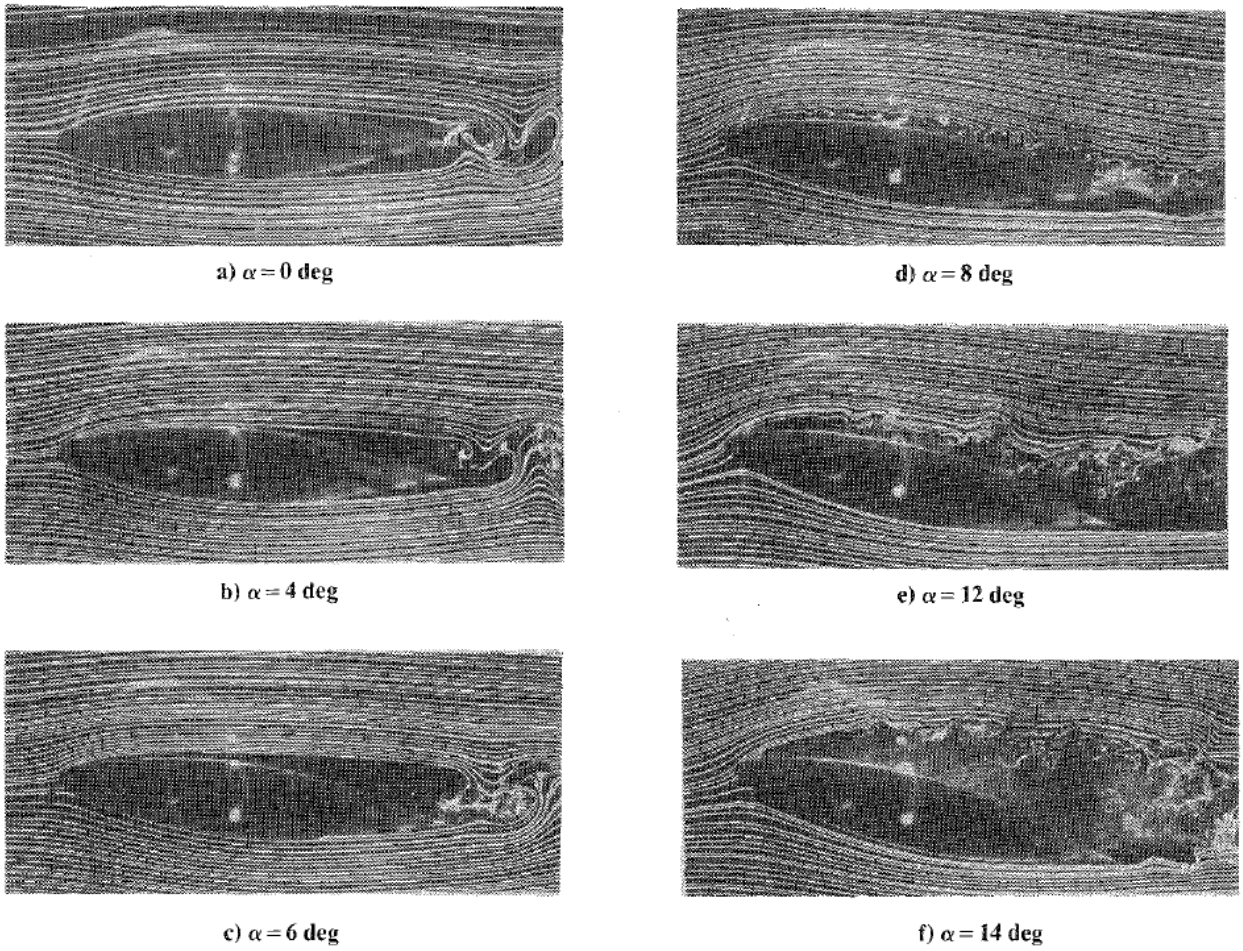

Figure 7-5: Smoke Visualization of Transition Bubble on a Smooth Airfoil at Re - 40,000 (Mueller & Batill, 1982)

To begin this analysis a survey of other low Reynolds number airfoil simulations was conducted. All prior work appeared to use fully orthogonal structured meshes with customized codes and transition models.[24] While useful for expanding theoretical knowledge and improving turbulence transition models these codes are not useful for full three dimensional MAV design and optimization studies. To conduct this project a very flexible set of mesh specifications was required along with solver settings which functioned over a broad range of aircraft geometries.

[24] (Lian & Shyy, 2007)

Work done by Kim, et al. in 2009 showed the complex turbulent behavior over a lifting airfoil at low Reynolds number in detail from experiment. As seen in Figure 7-6 the turbulent and recirculation regions of the boundary layer can extend up to 0.06 chord lengths from the airfoil surface at very low Reynolds numbers. Initially it was hoped that the same mesh settings used to simulate the Ogive tailed fuselage geometries would work with minor changes to maximum surface cell edge lengths. Unfortunately the separation, recirculation, and reattachment was not correctly captured modeled by the y+>30 mesh settings generated for the stowed geometry and fuselage analysis as illustrated by the extremely poor lift and drag prediction in Figure 7-7. At most five grid points would have been located in the unusually complex boundary layer. Therefore a y+<1 high resolution mesh was generated with 10 to 20 nodes in the boundary layer depending on chord location. Specifics of this process are discussed in the following section.

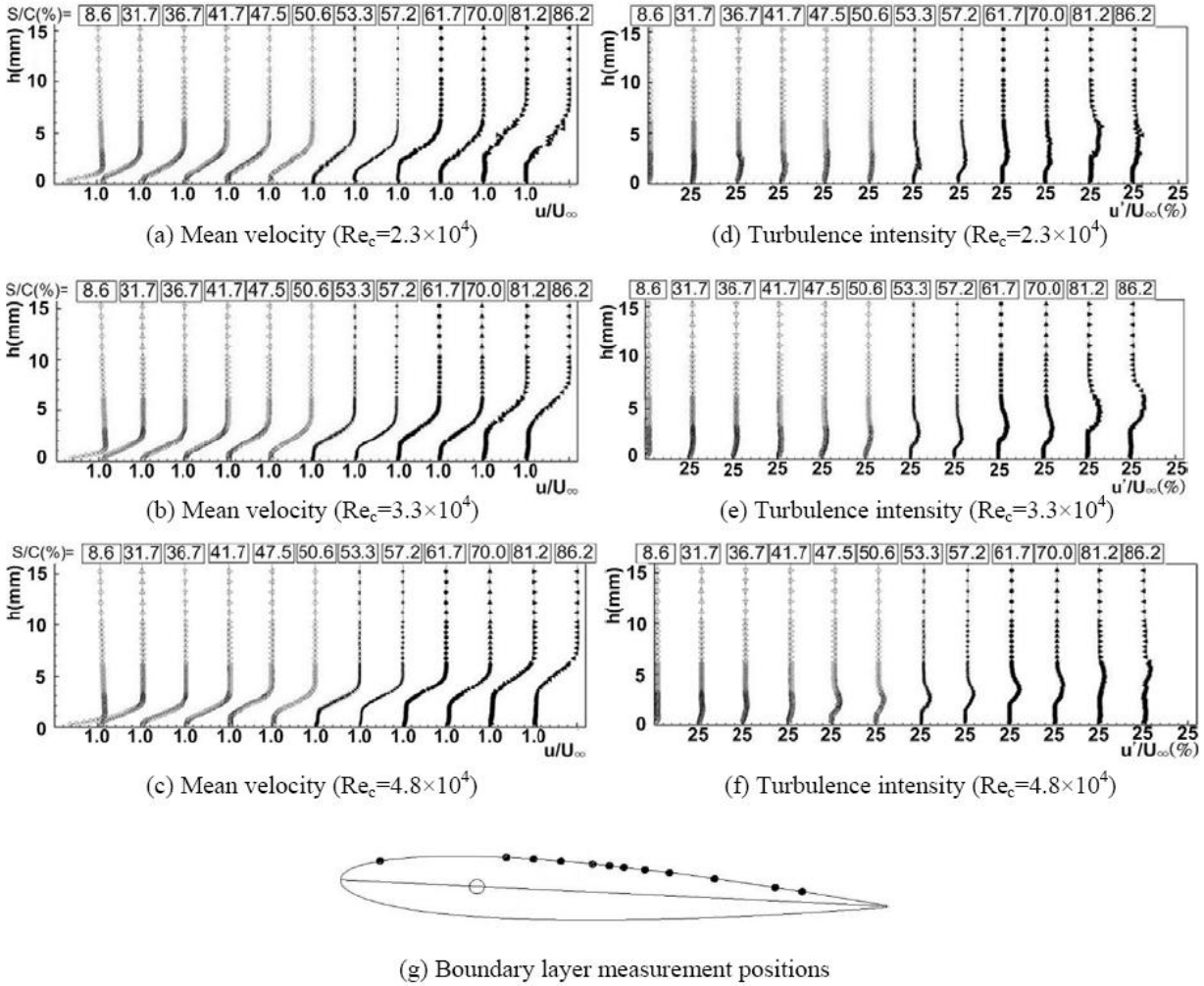

Figure 7-6: Turbulent Boundary Layer Measurements at Reynolds Numbers Under 0.5x10^5, Airfoil Chord = 180 *mm*, α=3^o (Kim, Yang, Chang, & Chung, 2009)

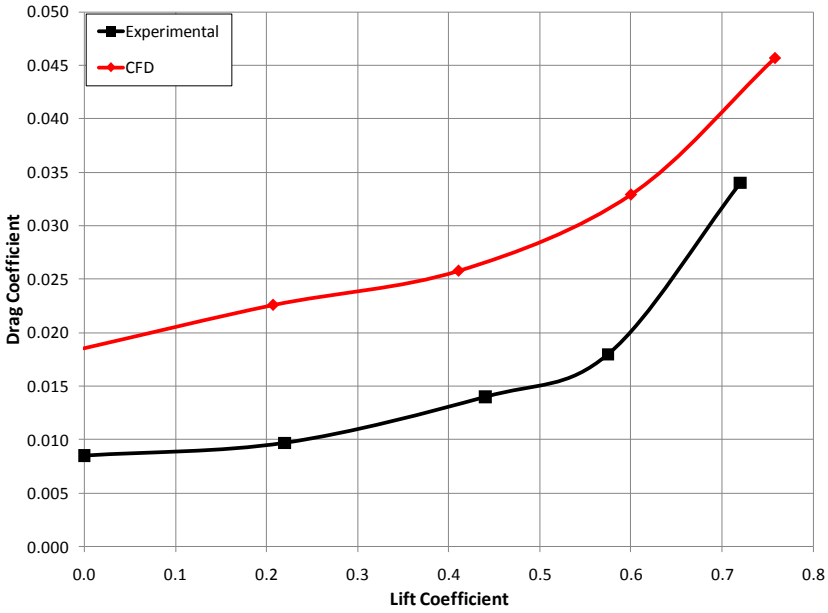

Figure 7-7: Comparison Between y+>30 Mesh Results and Experimental Data for a NACA 0009 Airfoil at Re=1.5x10^5. NACA 0009 Experimental Data, (Selig, Donovan, & Fraser, 1989)

7.2.1 NACA 0009 Validation

Two dimensional data required validation for both mesh independence and turbulence model selection. The simple NACA 0009 airfoil was chosen for mesh and solver validation due to the wealth of experimental data available. Low Reynolds number data for the NACA 0009, reported by Selig, et al., (1989) has been used for all validation studies. Many other airfoils were studied by Selig's group; a small subset is discussed later in this document.

7.2.1.1 Mesh Independence

Figure 7-8 presents the mesh regions on which the values in Table 7-1 were specified. Settings vary from the coarsest, Mesh 5, to the finest, Mesh 1. Results from these grids at a Reynolds number of 3x10^5 for both the lift and drag coefficients, as well as the lift-to-drag ratio, were used to check for grid independence as shown in Figure 7-9. This demonstrates that even Mesh 4 with its 8,480 cells would have been sufficient to obtain reasonable results. However, since the two dimensional solutions took minimal computational time, "Mesh 3 Mod", incorporating a thicker prismatic layer and a more detailed local refinement region, was used to improve accuracy. Results, presented in Figure 7-9, show that while no mesh completely matches the experimental lift curve, and all over-predict the drag curve, grid independence was achieved with Mesh 4. Lift matched well for all meshes, but there was an increase in predicted drag from all finer meshes to an angle of ten degrees where the fine meshes predicted lower drag.

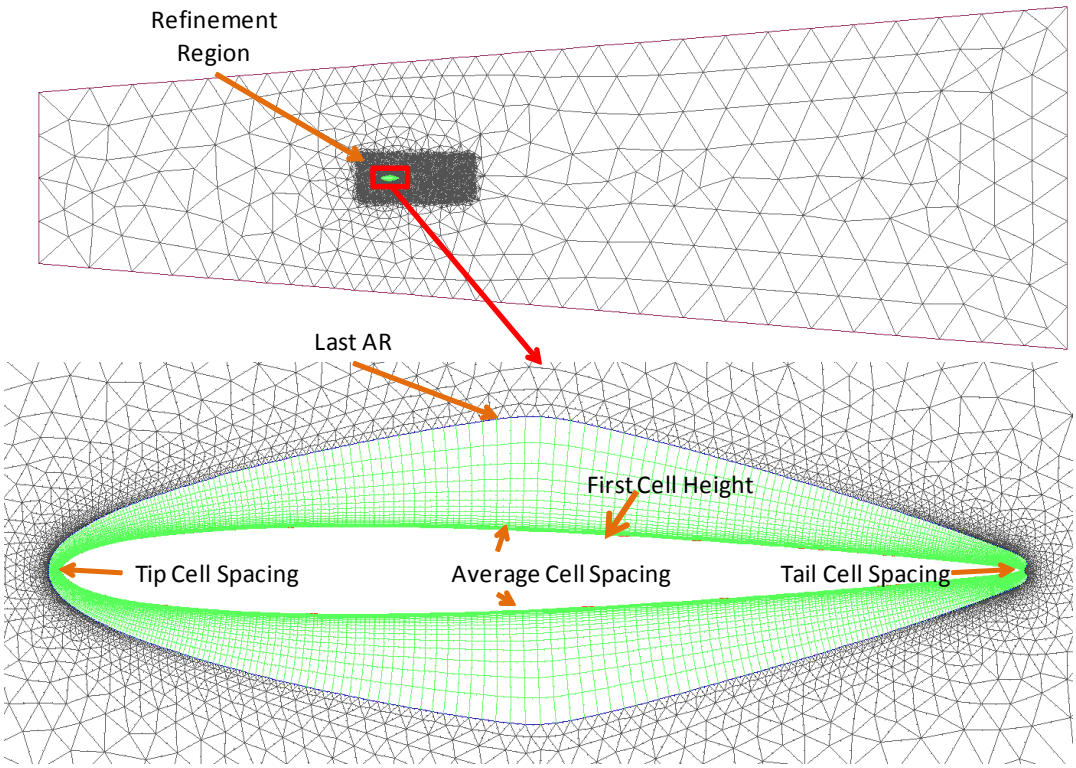

Figure 7-8: Mesh Regions for 2D Airfoil Studies, Labels as in Table 7-1

Table 7-1 Mesh Region Specifications for Figure 7-8, C=Chord Length, 0.1 *m* for this Study

Surface Mesh	**Mesh 5**	**Mesh 4**	**Mesh 3**	**Mesh 3 MOD**	**Mesh 2**	**Mesh 1**
Tip & Tail Spacing	0.004C (0.002C	0.002C	0.001C	0.001C (0.00033C	0.0005C	0.00025C
Average Cell Spacing	0.02C	.01C	.005C	.005C	.0025C	.00125C
Prismatic Layer	Last AR	Last AR	Last AR	Last AR	Last AR	Last AR
First Cell Height	0.00005C	0.00005C	0.00005C	0.00005C	0.00005C	0.00005C
Number of Layers	25	25	25	25	40	40
Aspect / Growth Rate	50%	50%	50%	200%	50%	50%
Tetrahedral Domain						
Domain Growth Rate	1.3	1.3	1.3	1.3	1.3	1.3
Refine Growth Rate	1.01	1.01	1.01	1.005	1.01	1.01
Refine X_{center}	2C	2C	2C	2C	2C	2C
Refine X_{length}	7C	7C	7C	7C	7C	7C
Refine Y_{length}	3C	3C	3C	3C	3C	3C
Refine Vol_{max}	400	200	100	50	100	100
Mesh Statistics	Last AR	Last AR	Last AR	Last AR	Last AR	Last AR
Skewness	0.78	0.71	0.72	0.74	0.77	0.75
Average Volume	1,709	1,061	509	358	263	98
Number of Cells	5,266	8,480	17,664	25,110	34,176	91,634

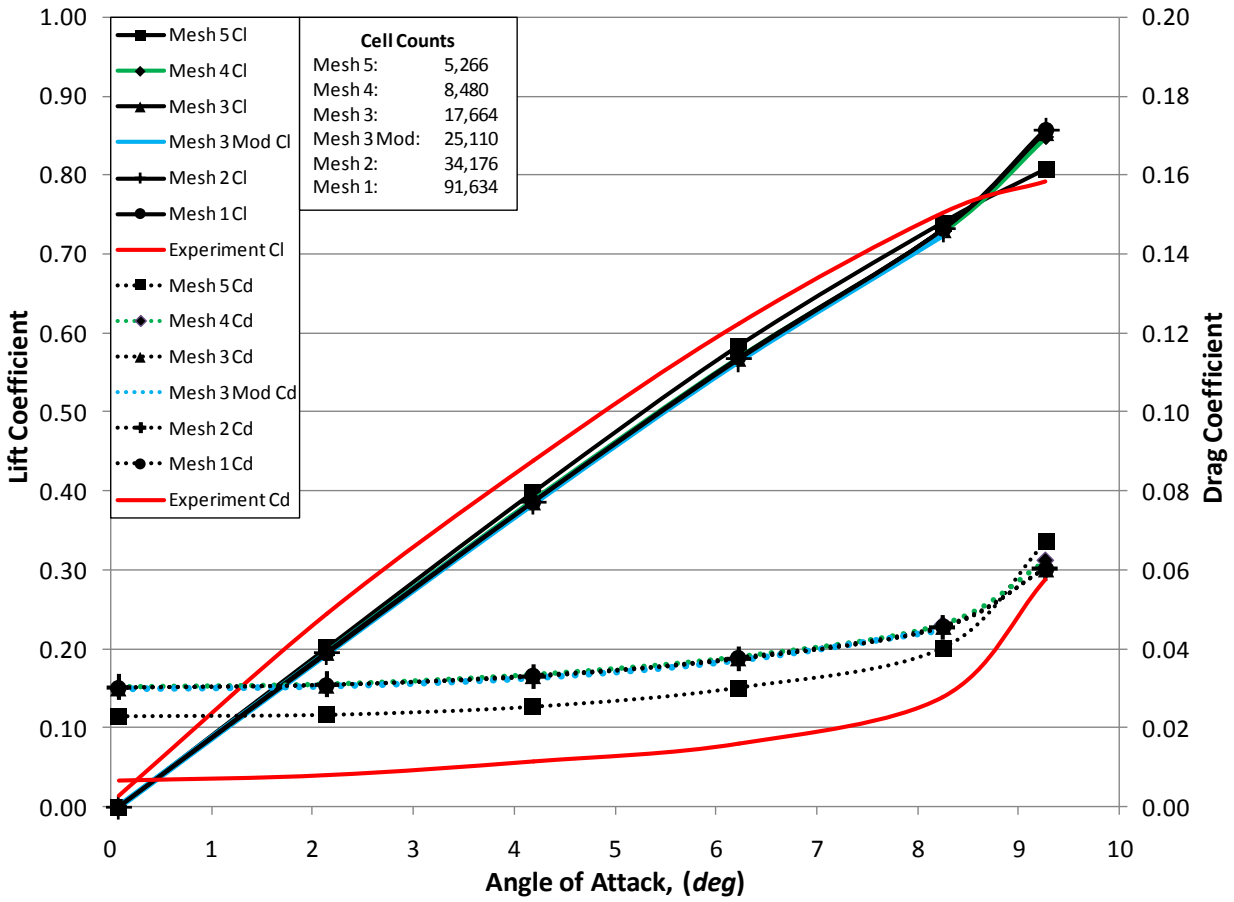

Figure 7-9: Lift and Drag Coefficient Plot Showing Mesh Independence for NACA 0009 2D Airfoil, Standard k-ω Turbulence Model

One geometric modification was made to the NACA 0009 and all other airfoils studied. As shown in Figure 7-10 the trailing edge of the airfoil was blunted. This was done by rotating the upper and lower surfaces about the leading edge by 0.1^{o} away from one another. To verify that this change had minimal effects Mesh 3 was compared to results generated by a sharp trailing edge geometry with the same upper and lower surface mesh settings.

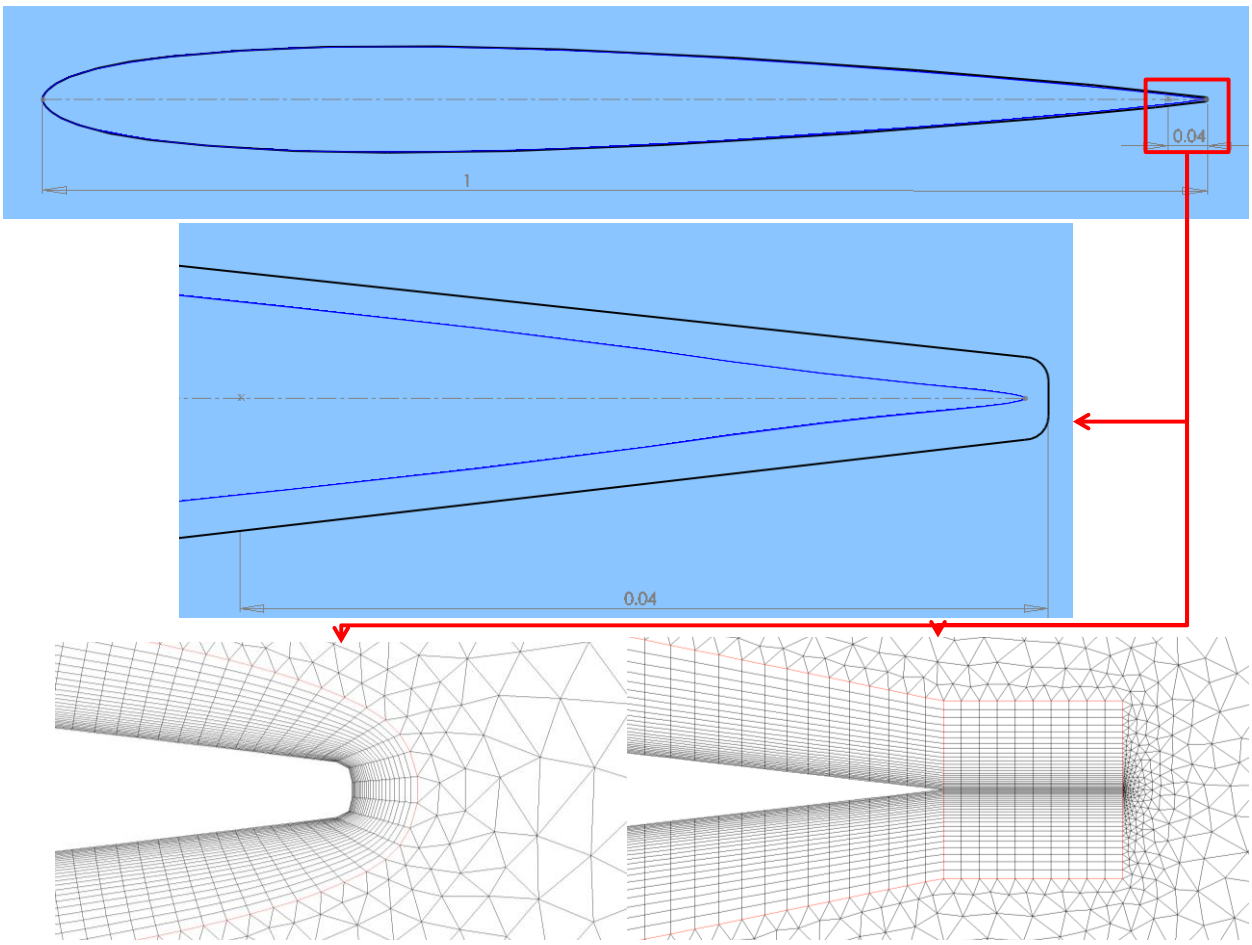

Figure 7-10: Comparison of Blunt and Sharp Trailing Edge Mesh Geometries, Dimensions in *m*

Figure 7-11 shows that the lift and drag coefficients returned by the blunted geometry were nearly identical to those calculated for the sharp training edge. Lift and drag coefficients for this study were not expected to match experimental data at this point. Errors at this stage were likely due to imperfect transition and turbulence modeling with the current settings. Following sections discuss the process used to select an appropriate turbulence model for these Reynolds numbers. This geometric modification allowed a single "last AR" prismatic layer to be grown from the surface of the airfoil which greatly simplified mesh generation for both two and three dimensional cases. A "last AR" prismatic layer creates a set of prism cells with the final layer having a specified ratio between the cell height normal to the surface and the cell length along the surface. Prismatic layers specified in this manner are more flexible and easier to generate around complex geometries but deal poorly with sharp edges. In this project it was easier to eliminate sharp edges by going back to the geometric model an inserting fillets and chamfers rather than developing a more complex and more tightly structured mesh. This blunted geometry is also likely more representative of any physical model which would be created. Even if the effort were invested to create a perfect sharp trailing edge it would likely be blunted in use.

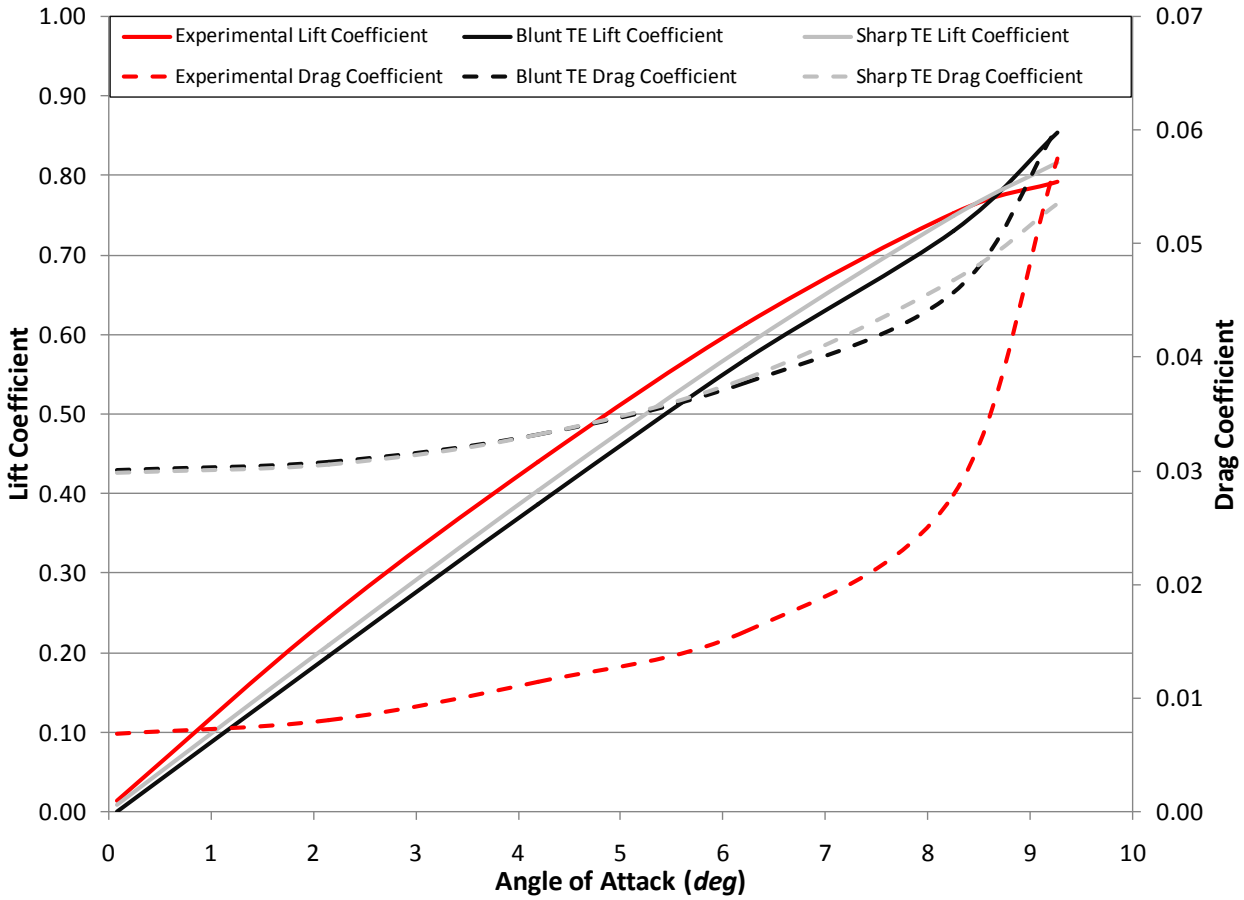

Figure 7-11: Comparison of Blunt and Sharp Trailing Edge Mesh Results, Standard k-ω Turbulence Model

7.2.1.2 Turbulence Model Selection

As seen in Figure 7-7, the standard k-ω turbulence model produced extremely poor results. As this research program was focused on design work it was not practical to write a custom turbulence model for this flow regime. A model sufficient to produce conservative first-cut engineering estimates was required. To this end the full suite of turbulence models and settings available in Fluent 12 was examined on Mesh 3 Mod at an angle of attack of 6^{o} and a Reynolds number of $3x10^{5}$. Table 7-2 presents a summary of all turbulence models, some general comments, and their performance in this case. Laminar solutions were also attempted in both steady-state and transient formulations. Neither configuration returned useful results and have been omitted here. Laminar solvers failed to capture the leading edge separation, circulation bubble, and reattachment and returned a fully-stalled solution as soon as leading edge separation occurred. Only those models which predicted both lift and drag coefficients, and lift-to-drag ratio, within were selected for further study. The Reynolds Stress models have been omitted due to the number of options to be displayed, and the fact that these seven equation models performed poorly and ran slowly in later testing.

Table 7-2: Summary of Fluent 12 Turbulence Models Applied to NACA 0009 at 6° Angle of Attack and Reynolds Number of $3x10^5$, Errors Less than 10% Highlighted in Green

Model	Prediction for NACA 0009 at α=6°				Comments
	C_L	% Error C_L	C_D	% Error C_D	
Laminar	Unstable	Err	Unstable	Err	Failed due to flow detatchment at separation bubble, no modeling for re-attachment
Spalart - Allmaras					
Vorticity - Low RE	0.657	7.15%	0.017	6.92%	Simple, one equation model built for the aerospace industry to handle wall bounded and adverse presure gradient flows
Strain/Vorticity - Low RE	0.655	6.79%	0.017	5.66%	
Strain/Vorticity	0.062	-89.85%	0.026	64.15%	
Vorticity	0.062	-89.87%	0.027	66.67%	
k-ε					
Standard-Standard	0.592	-3.46%	0.041	155.35%	Simple two equation model based on turbulent kinetic energy and turbulent dissipation rate
Standard- NWF	0.563	-8.14%	0.053	230.82%	
Standard - Enh Wall	0.612	-0.20%	0.038	135.85%	
Standard - Enh Wall - Press Grad	0.612	-0.24%	0.038	135.85%	
RNG - Standard	0.624	1.75%	0.029	81.76%	RNG model improved for high strain rates
RNG - NWF	0.589	-3.85%	0.041	159.12%	
RNG - Enh Wall	0.649	5.84%	0.028	75.47%	
RNG - Enh Wall - Press Grad	0.649	5.84%	0.023	43.40%	
RNG - Standard - DVM	Unstable	Err	Unstable	Err	
RNG - NWF - DVM	Unstable	Err	Unstable	Err	
RNG - Enh Wall - DVM	0.645	5.22%	0.024	50.94%	
RNG - Enh Wall - DVM - Press Grad	0.645	5.22%	0.240	1409.43%	
Realizable - Standard	0.622	1.47%	0.027	68.55%	Realizable model built for planar and round jets, rotation, adverse pressure, separation, and recirculation
Realizable - NWF	0.586	-4.34%	0.038	140.88%	
Realizable - Enh Wall	0.652	6.39%	0.020	28.30%	
Realizable - Enh Wall - Press Grad	0.652	6.41%	0.020	28.30%	
k-ω					
Standard	0.635	3.54%	0.026	64.15%	Standard model verified for wakes, mixing layers, and jets. Should be valid for wall bounded shear flows
Standard - Low Re	0.620	1.14%	0.035	118.24%	
Standard - Shear	0.631	2.97%	0.025	55.97%	
Standard Low Re - Shear	0.616	0.52%	0.032	99.37%	
SST	0.651	6.18%	0.016	3.14%	SST model uses the k-ω model in the near field and the k-ε model in the far-field
SST - Low RE	Unstable	Err	Unstable	Err	
Transition k-kl-ω Steady	Unstable	Err	Unstable	Err	
Transition SST Steady	Unstable	Err	Unstable	Err	
Transition SST dt=10^{-5}	0.653	6.56%	0.017	3.77%	

With the first down-select complete all potential turbulence models were run at angles of attack between 0° and 8° at two degree increments at Reynolds numbers of $3.0x10^5$, $1.5x10^5$, $1.0x10^5$, and $0.6x10^5$. These Reynolds numbers were selected to correspond with Selig's published data.[25] Repeated down-selects occurred each time the Reynolds number was reduced based on the closest experimental match at the current Reynolds number. Figure 7-12 shows lift-to-drag ratio data after the first down-select. All steady-state models under-predicted the lift-to-drag ratio across the range. Two transient turbulence transition models, SST and k-kl-ω were also examined. Neither performed well; both over-predicted lift and under-predicted drag and were therefore useless as conservative engineering tools, even neglecting the 10^{-5} *s* time step forcing extremely long run times and making three dimensional simulations utterly impractical.

[25] (Selig, Donovan, & Fraser, 1989)

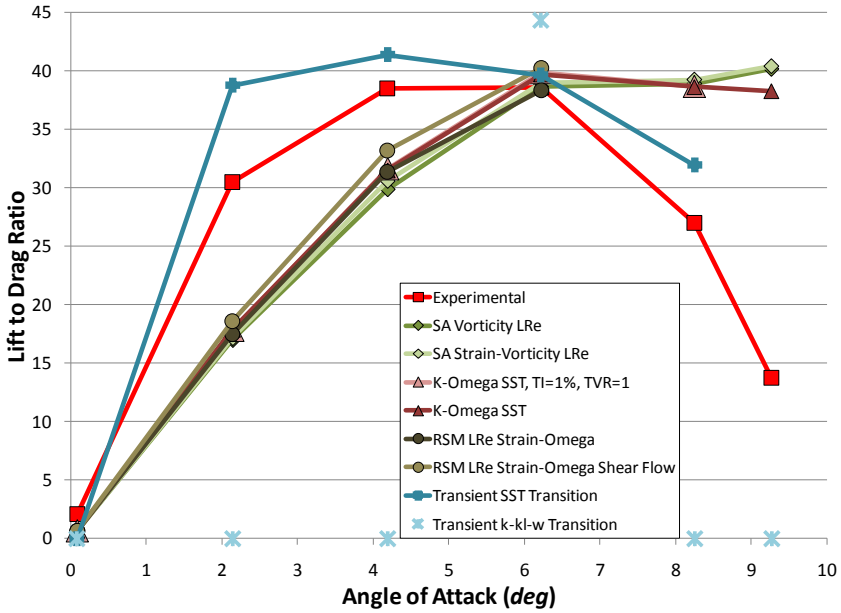

Figure 7-12: Lift-to-drag Ratios for Selected Turbulence Models at a Reynolds Number of $3x10^5$

Continuing down-selects were conducted as the Reynolds number was reduced to $1.5x10^5$, $1.0x10^5$, and $0.6x10^5$. The final lift to drag ratio plot, Figure 7-13, compares the two permutations of the Spalart-Allmaras turbulence model and a pair of k-ω model permutations. While the faster one equation Spalart-Allmaras model would have been preferable due to its reduced computational time, especially when looking forward to three dimensional modeling, the far better stall prediction of the k-ω SST model made it the clear winner.

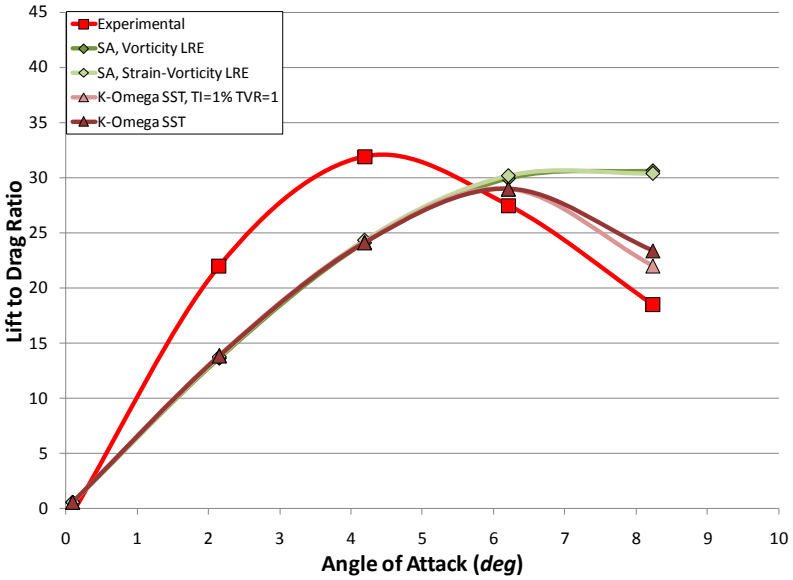

Figure 7-13: Lift-to-drag Ratios for Final Turbulence Model Down-Select at Reynolds Number of $0.6x10^5$

From this process the k-ω SST model was selected for its accuracy, simplicity of implementation, and short run times. Most turbulence models produced very similar results, under-predicting efficiency to 6° angle of attack and over-predicting afterward. Only the transient SST Transition model seemed to predict the physical stall angle, however it significantly over-predicted efficiency across the lower angle range and was therefore not a useful engineering tool. The transient k-kl-ω model was only checked at 6° and returned a significant over-prediction which also made it useless as a preliminary design tool. All turbulence models which produced useful results under-predicted performance at lower angles of attack, however since all were built on the assumption of fully turbulent flow stall was not predicted at the physically correct angle. The increased mixing caused by the fully turbulent boundary layer solution maintained flow attachment resulting in over-predictions of lift and under-predictions of drag past the physical stall angle of 6°.

Figure 7-14 through Figure 7-17 show the drag polars at each Reynolds number across the angle of attack range from zero degrees to eight degrees. Note that for these plots the experimental data was taken from tabulated lists which were not precisely at 0, 2, 4, 6, and 8 degrees angle of attack due to the limitations of the experimental apparatus used.

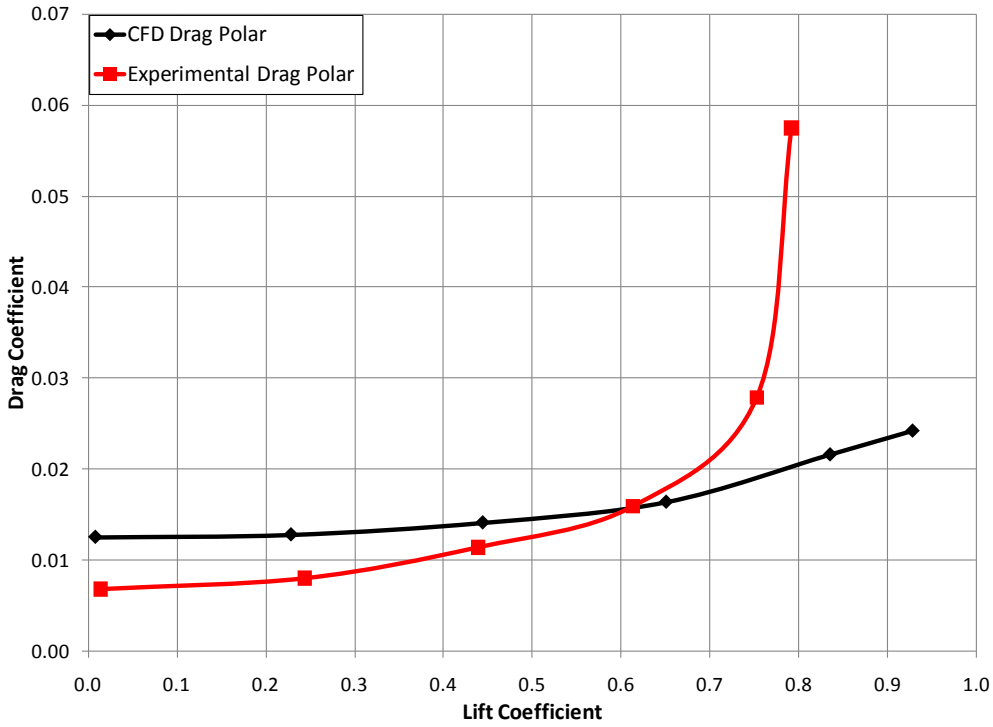

Figure 7-14: Drag Polar Using K-ω SST Turbulence Model for a NACA 0009 at a Reynolds Number of $3.0x10^5$, Markers at 2° α Increments from 0°

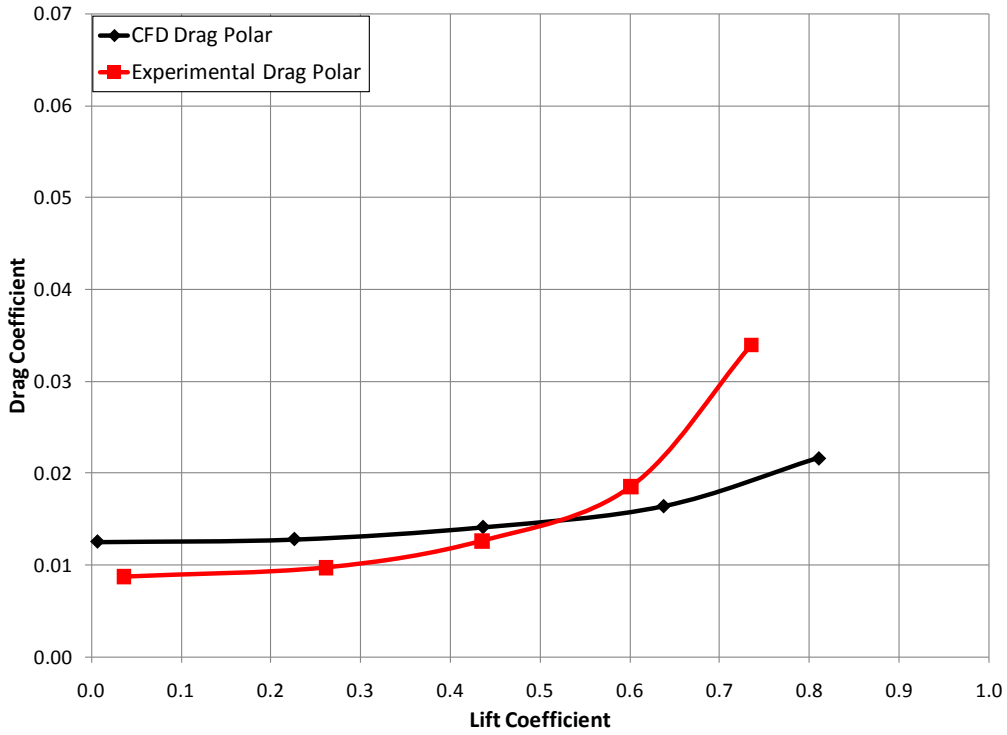

Figure 7-15: Drag Polar Using K-ω SST Turbulence Model for a NACA 0009 at a Reynolds Number of $1.5x10^5$, Markers at 2^o α Increments from 0^o

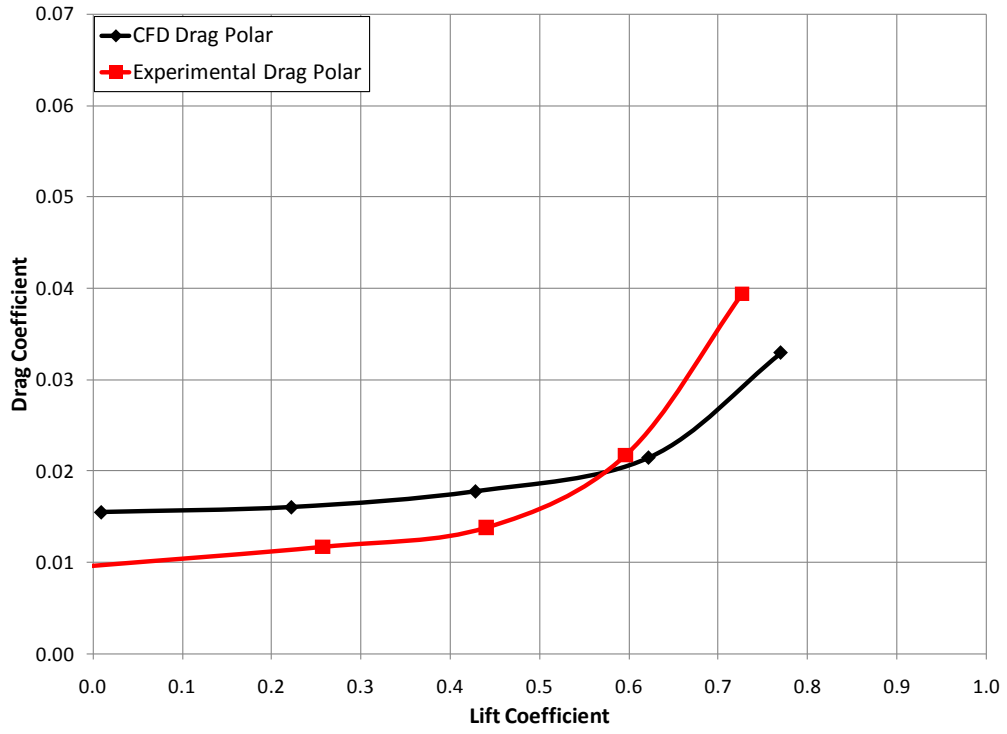

Figure 7-16: Drag Polar Using K-ω SST Turbulence Model for a NACA 0009 at a Reynolds Number of $1.0x10^5$, Markers at 2^o α Increments from 0^o

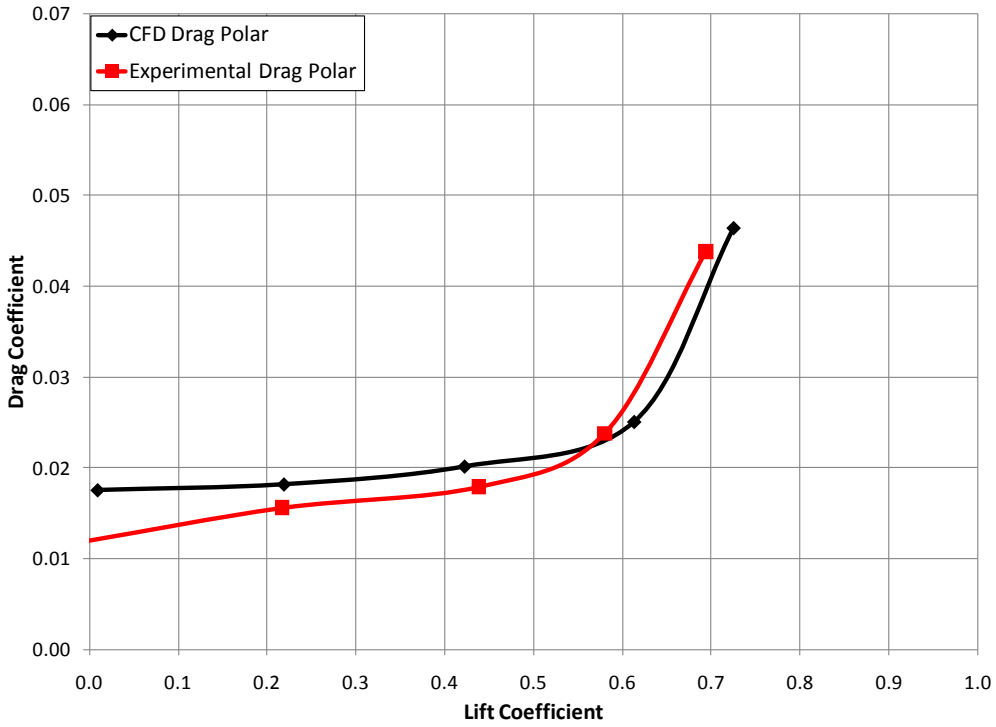

Figure 7-17: Drag Polar Using K-ω SST Turbulence Model for a NACA 0009 at a Reynolds Number of $0.6x10^5$, Markers at 2^o α Increments from 0^o

While not perfect by any means the preceding results show that the k-ω SST model provided an acceptable preliminary engineering design tool, particularly at moderate angles of attack and lower Reynolds numbers. In all cases the lift was predicted with reasonable accuracy and the drag tended to be over predicted which resulted in conservative performance estimates. Wind tunnel testing would be required to verify a final design or to inform the design optimization process. Prediction was poor near zero degrees angle of attack due to the solver forcing a turbulent boundary layer around the entire airfoil. Physically large portions of the leading edge boundary layer were likely laminar in nature and therefore producing less drag. In addition, the lift coefficient, and lift-to-drag ratio was over predicted at high angles of attack. This was likely due to the turbulence model maintaining flow attachment past the point where flow separation would begin. It is interesting to note that the pre-stall prediction performance of these settings improved significantly as the Reynolds number was reduced.

Surprisingly the turbulence model did indicate the existence of a circulation bubble and reattachment region as shown in Figure 7-18 and Figure 7-19.

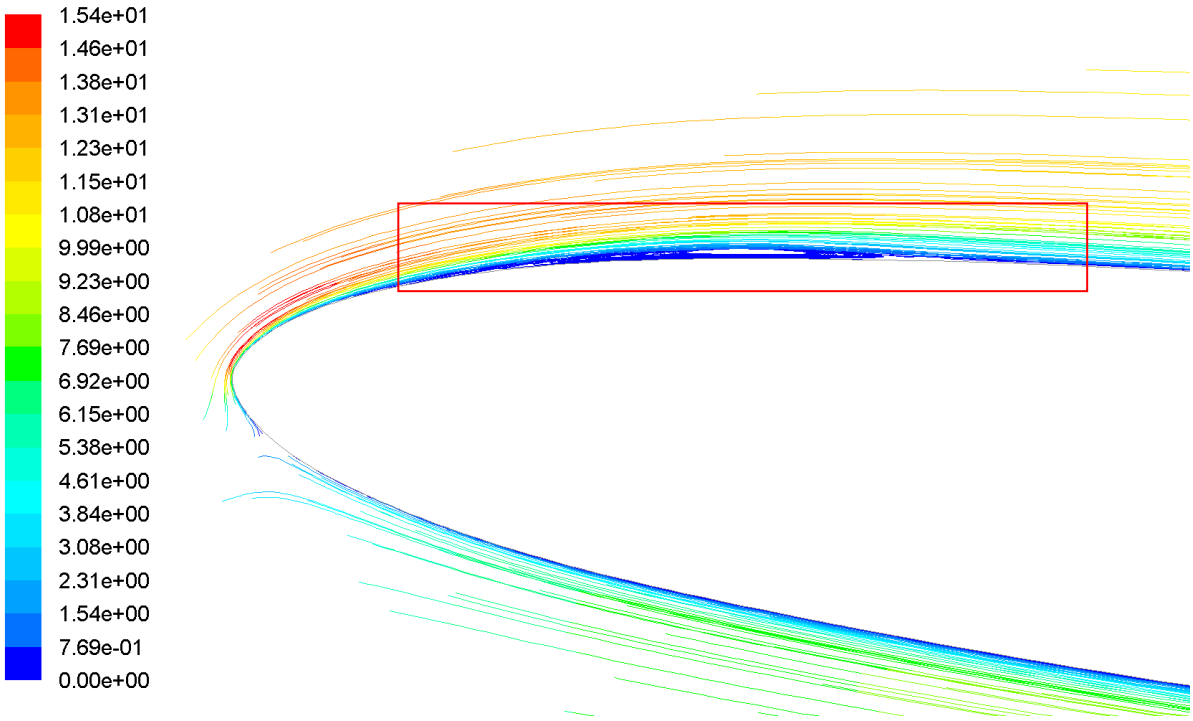

Figure 7-18: Velocity Pathlines (*m/s*) Showing Prediction of Recirculating Separation Bubble, 6° *α*, Re=0.6x10^5

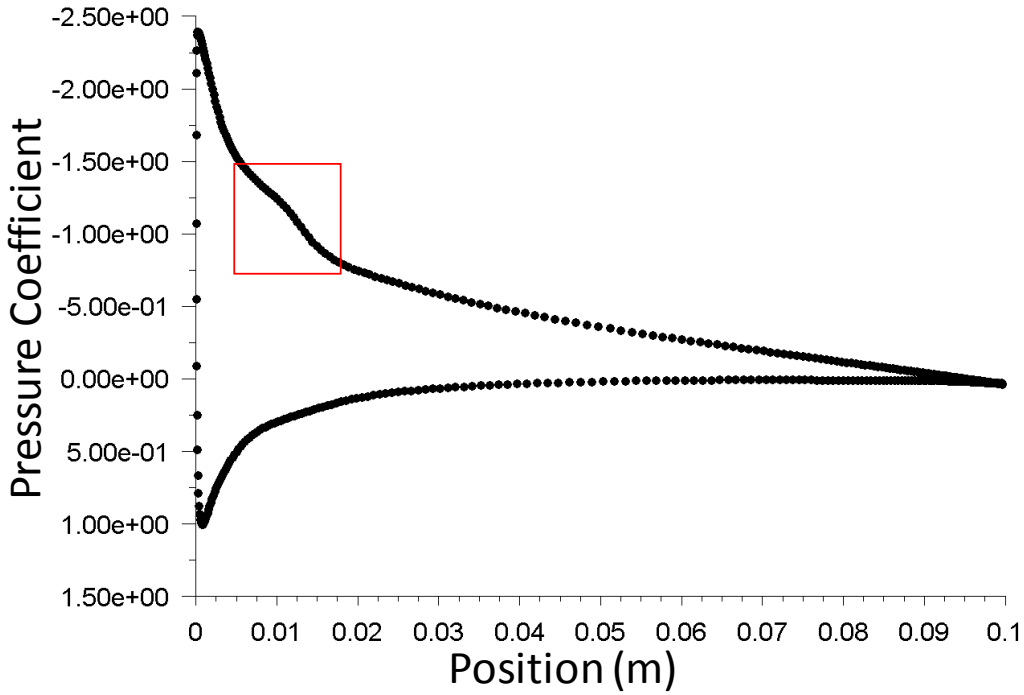

Figure 7-19: Pressure Coefficient Around NACA 0009 Showing Separation Bubble "plateau", 6° *α*, Re=0.6x10^5

This demonstrates that, while not yet physical in magnitude and location, the field of turbulence modeling is progressing toward the ability to accurately predict low Reynolds number aerodynamics on arbitrary aircraft geometry. In fact work with the model constants in the Fluent solver could significantly increase accuracy. This was not pursued for the current project since acceptable results had already been obtained. Future work on this project could involve some experimentation with these constants to more closely match physical data.

7.2.2 Two Dimensional Airfoil Comparison

Table 7-3 shows the seven airfoils analyzed with the mesh and solver settings discussed previously. With the NACA 0009 already complete the other six were simulated at angles of attack from zero to eight degrees and the same set of four Reynolds numbers.

Table 7-3: Selected Airfoil Profiles and Details

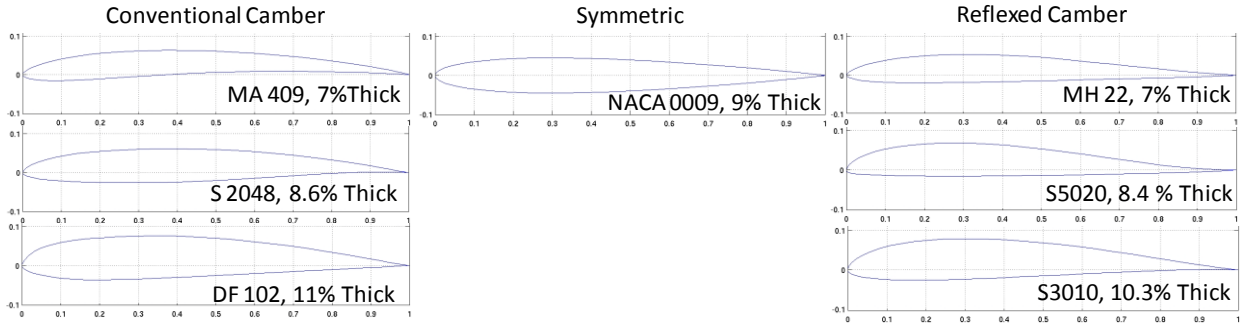

Figure 7-20 through Figure 7-26 present the drag polars for each airfoil. It is interesting to note that the quality of prediction improves as the airfoil thickness to chord ratio increases. This is likely due to the larger separation bubbles created by the sharper leading edge radius on thinner airfoils. The same trend of reasonably predicting lift and over predicting drag within the useful angle of attack range held for all but the MA 409 which had the smallest leading edge radius of all. Experimental data was unavailable for either the S5020 or S3010 airfoils. Developing this comparison with experiment was necessary to provide confidence in the ability to predict the behavior of three dimensional wings using these or other airfoils. The cost to experimentally test all airfoils, wing, and wing-body configurations would be prohibitive; therefore the current study was conducted to provide a basis for a computational optimization analysis. Future experimental work will be used to verify and improve the computational predictions.

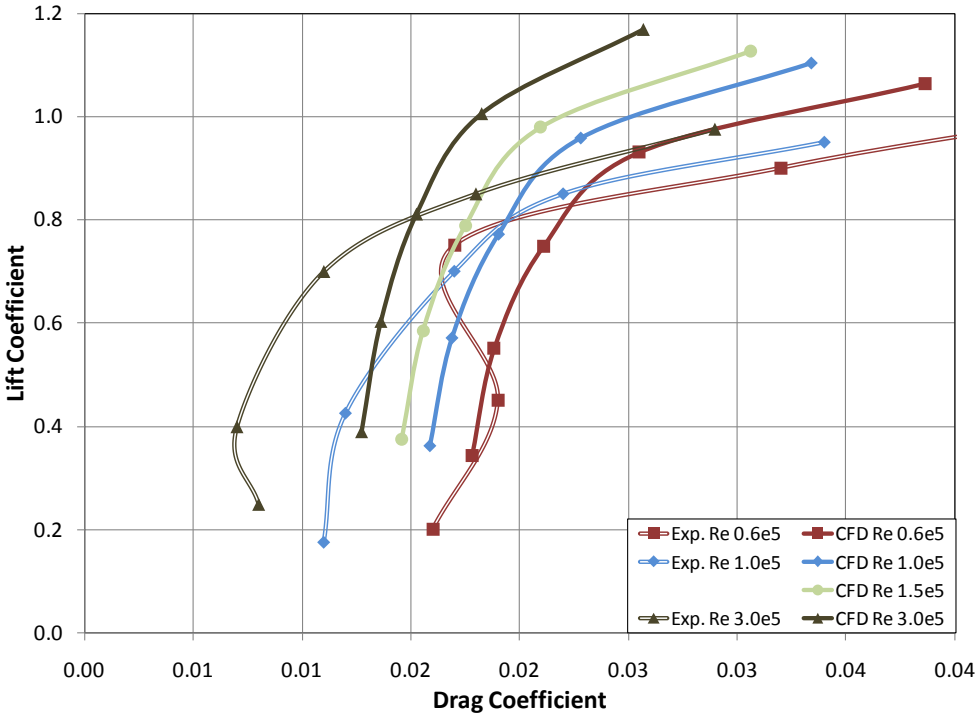

Figure 7-20: MA 409 Drag Polar with Experimental and CFD Data

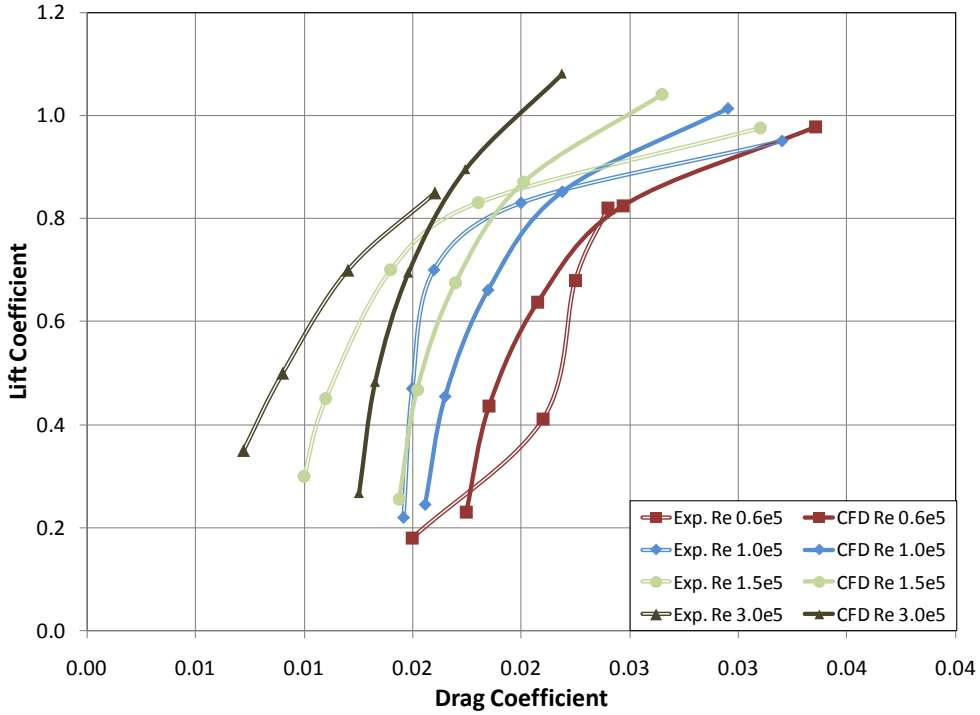

Figure 7-21: S 2048Drag Polar with Experimental and CFD Data

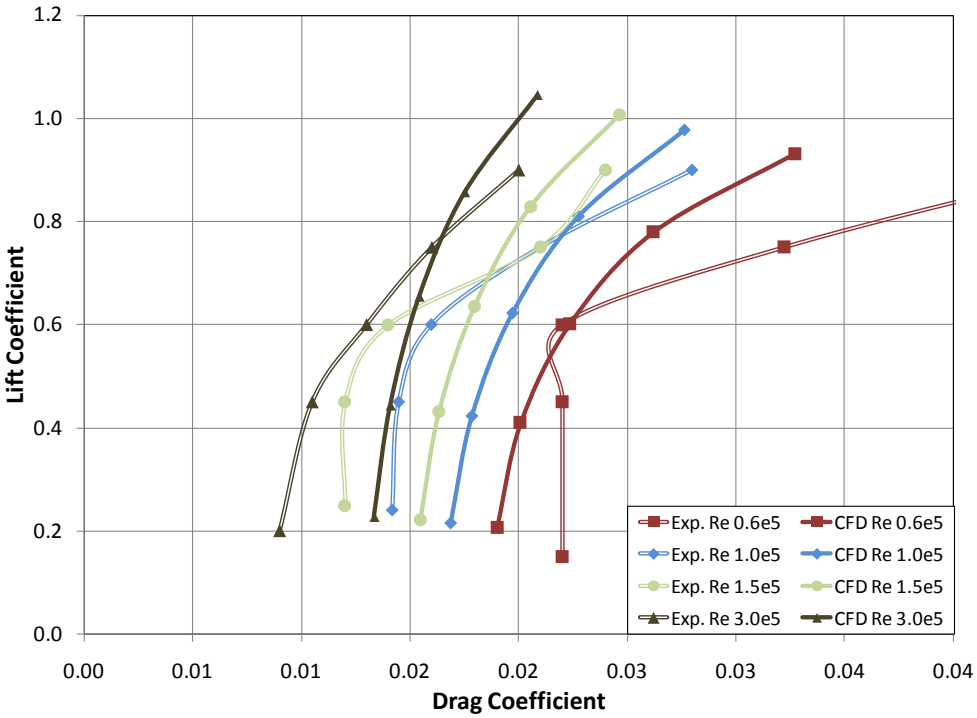

Figure 7-22: DF 102 Drag Polar with Experimental and CFD Data

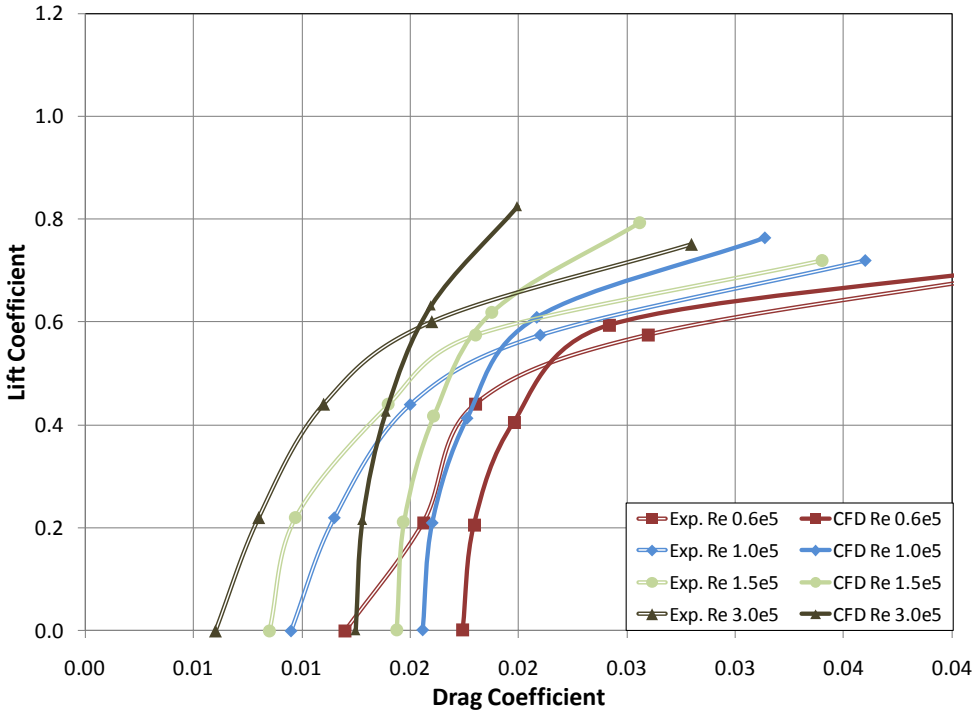

Figure 7-23: NACA 0009 Drag Polar with Experimental and CFD Data

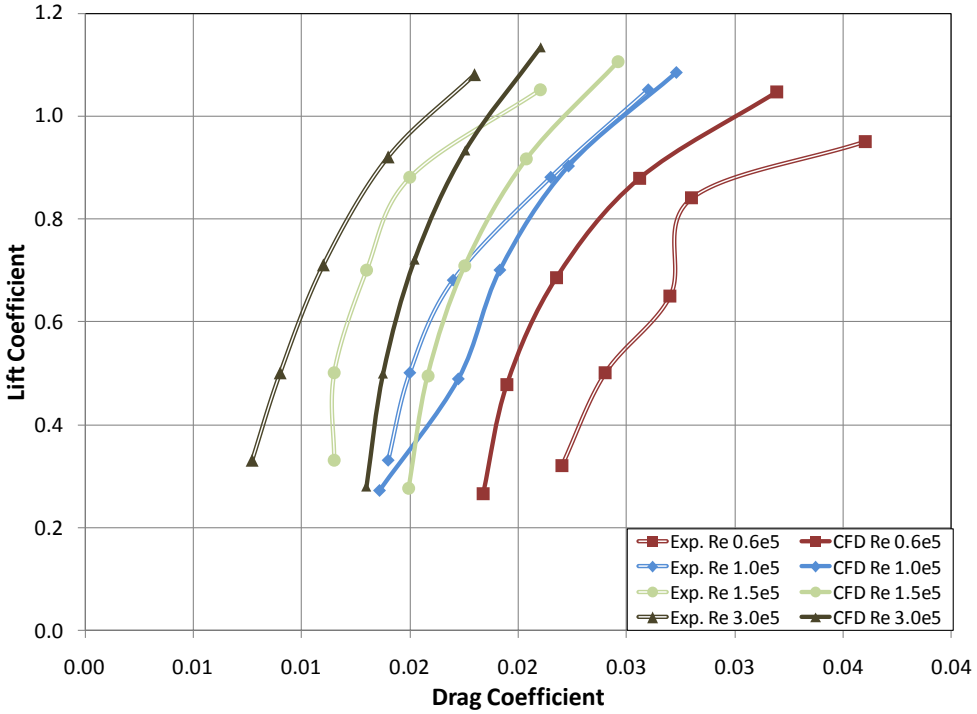

Figure 7-24: S 3010 Drag Polar with Experimental and CFD Data

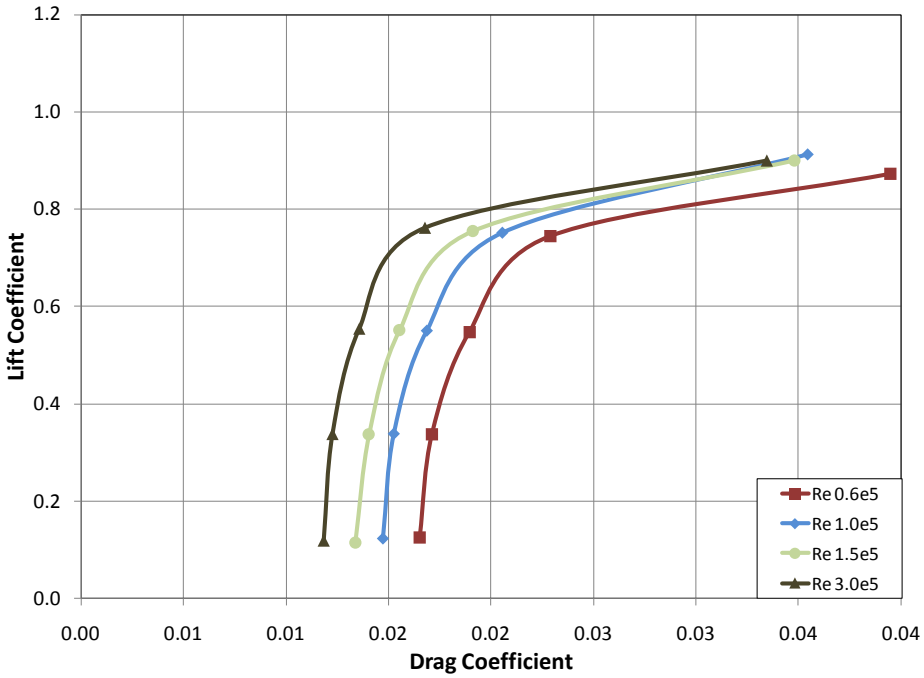

Figure 7-25: MH 22 Drag Polar

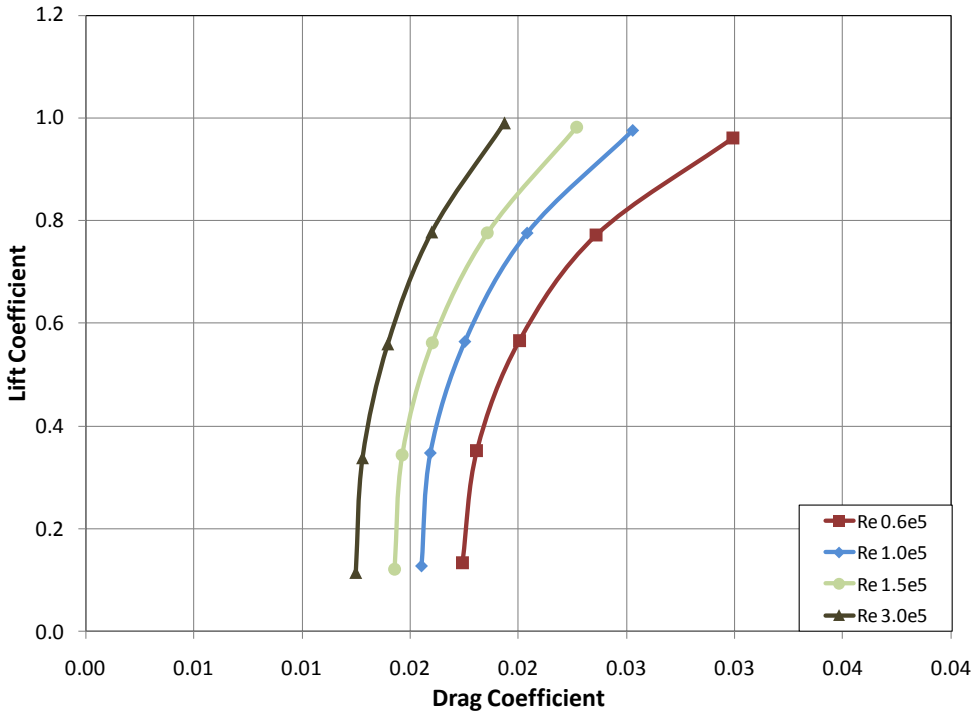

Figure 7-26: S 5020 Drag Polar

While this analysis does show some capability to predict the performance of various airfoils at low Reynolds numbers it did not seem likely that an accurate representation of their effects in three dimensions would be correctly captured. Parametric numerical studies of other airfoils would be interesting future work if coupled with a wind tunnel verification study.

7.3 Preliminary Three Dimensional Main Wing Analysis

Early three dimensional wing work was done prior to the two dimensional analysis discussed in Section 7.2. A DF102 airfoil was used prior to obtaining a full appreciation for simulation of flow in this regime. While the general trends of that early work, reported here, are consistent with other projects such as the work done by Mueller, et al. (2006) the specific values and exact locations of optimums are questionable [26]. Future work will complete a more detailed set of these analyses using mesh and solver settings expanded from Section 7.2 but the previously collected trends provided information that is worth covering as a preliminary step in this direction. The more detailed analysis will use chordwise meshes and solver models based on those developed in the 2D work discussed previously in this document.

[26] (Mueller, Torres, & Srull, Elements of Aerodynamics, Propulsion, and Design, 2006)

Figure 7-27 shows the primarily structured hexahedral prismatic boundary layer with triangular prism tips used for the 3D study. A detailed listing of the mesh generation parameters used is presented in Appendix B. Grid independence was reached, as illustrated by the lift and drag convergence shown in Figure 7-28, at $1.5x10^6$ cells. Geometric and flow parameters used are presented in Table 7-4. The 33 *m/s* flow velocity was selected in an attempt to split the difference between the high-speed extended range mission and the low-speed long endurance mission so that two sets of planform studies would not be required. A lift coefficient of 2.09 based on the fuselage frontal area was required to lift the 180*g* mass MAV at 33 *m/s* and all wings were incremented in angle of attack until this value was reached. Stowed geometry body diameter was used as the reference area for lift and drag coefficient calculations due to the huge variation in planform area between the high-speed and long-endurance (nearly 500% larger) designs. A fixed reference was required to easily compare efficiencies of the competing designs. Performance data was then collected with each planform producing sufficient lift to complete the mission.

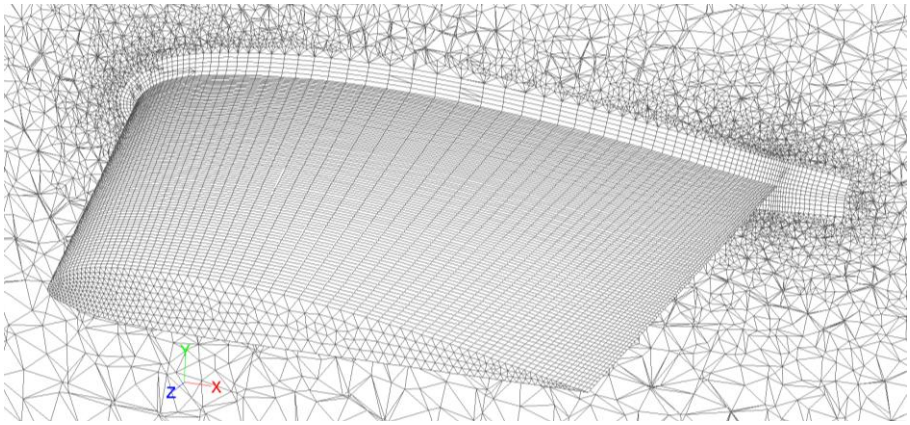

Figure 7-27: Surface and Centerline Volume Mesh for Initial 3D Wing Modeling

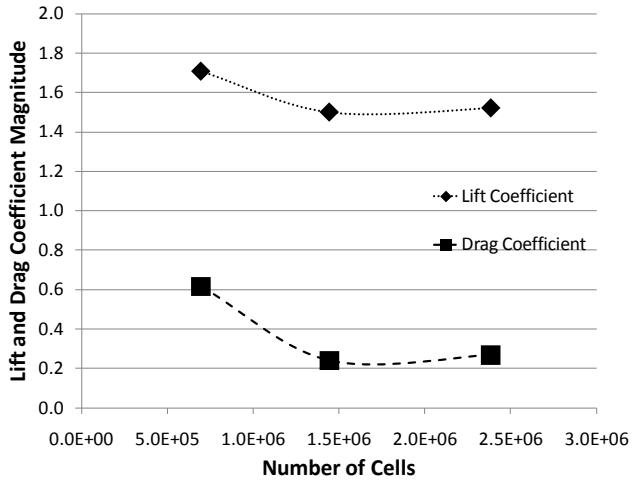

Figure 7-28: Mesh Independence Plot for Initial 3D Wing Modeling

Table 7-4: Flow Parameters, Lift Coefficient, and Geometric Parameters Varied for Three Dimensional Planform Study

Velocity	33	*m/s*	Lift Coefficient, based on fuselage frontal area			2.09
Airfoil	Wing Loading	Aspect Ratio	Sweep Angle	Taper Ratio	Wing Area	Re_{MAC}
	N/m^2		*deg*		cm^2	
DF 102	200	3	30	0.5	88.29	127,096
	300	3	30	0.5	58.86	103,773
	300	3	30	0.75	58.86	100,748
	300	3	30	1	58.86	100,067
	300	3	15	0.5	58.86	103,773
	300	3	0	0.5	58.86	103,773
	300	2	30	0.5	58.86	127,096
	300	4	30	0.5	58.86	89,870
	400	3	30	0.5	44.15	89,870

As expected, Figure 7-29 shows that the classical three dimensional flow structure about a lifting wing has been captured by this simulation. The reference wing that all parameters was varied from used a DF 102 airfoil, 300 N/m^2 wing loading, aspect ratio of 3, 30^o sweep angle, and a taper ratio of 0.5.

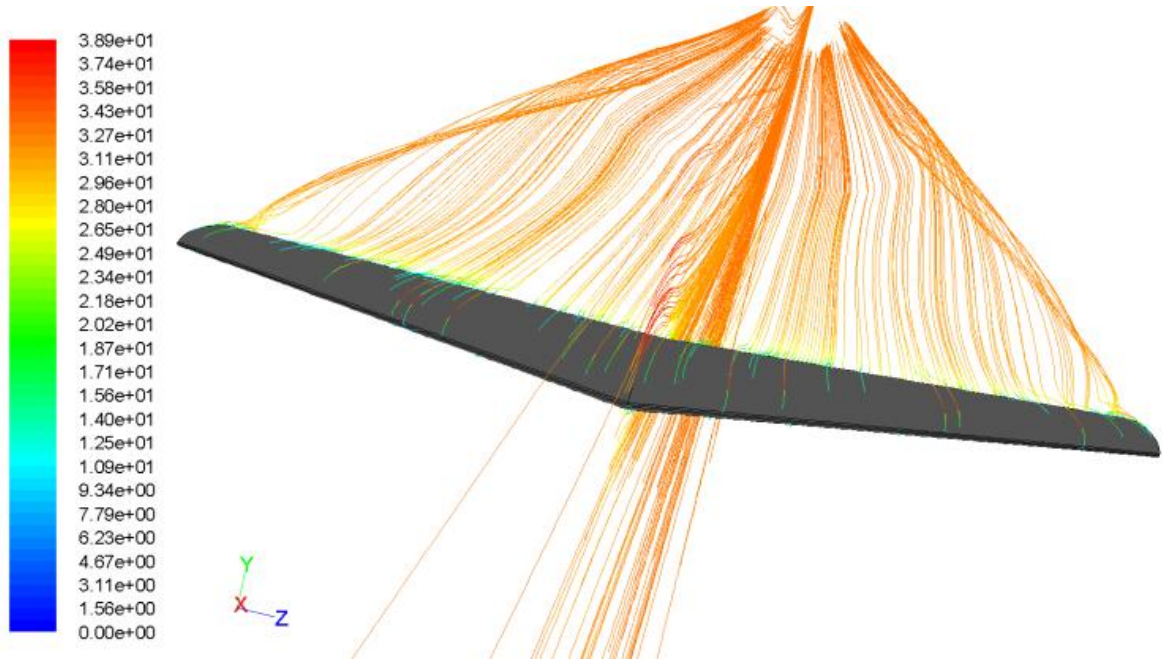

Figure 7-29: Pathlines Colored by Velocity (*m/s*) Around Reference Wing (Angle of Attack = 4^o)

The most interesting result of this preliminary 3D wing analysis was the inverse relationship between aspect ratio and the lift-to-drag ratio of these wings. This is entirely counter to classical aerodynamic theory which states that as aspect ratio increases efficiency also increases due to a reduction in induced drag. Figure 7-30 clearly shows nearly a 25% drop in performance as the aspect ratio was doubled from 2 to 4. A drop of 40,000 in the Reynolds number accompanied the increased aspect ratio. This indicates that an optimum exists, which is significantly driven by the Reynolds number at the mean aerodynamic chord for aircraft at this small scale. Apparently for MAVs in certain flight regimes, with a fixed wing area, the increased efficiency of the airfoil section caused by increased mean aerodynamic chord Reynolds number can be significantly greater than the induced drag penalty incurred by reducing aspect ratio. In the more detailed study currently underway, aspect ratios of 0.5, 1.0, and 1.5 will also be examined. At some point the induced drag losses must begin to overwhelm the increased Reynolds number effects. Finding this point will be critical to optimizing the final design of these MAVs.

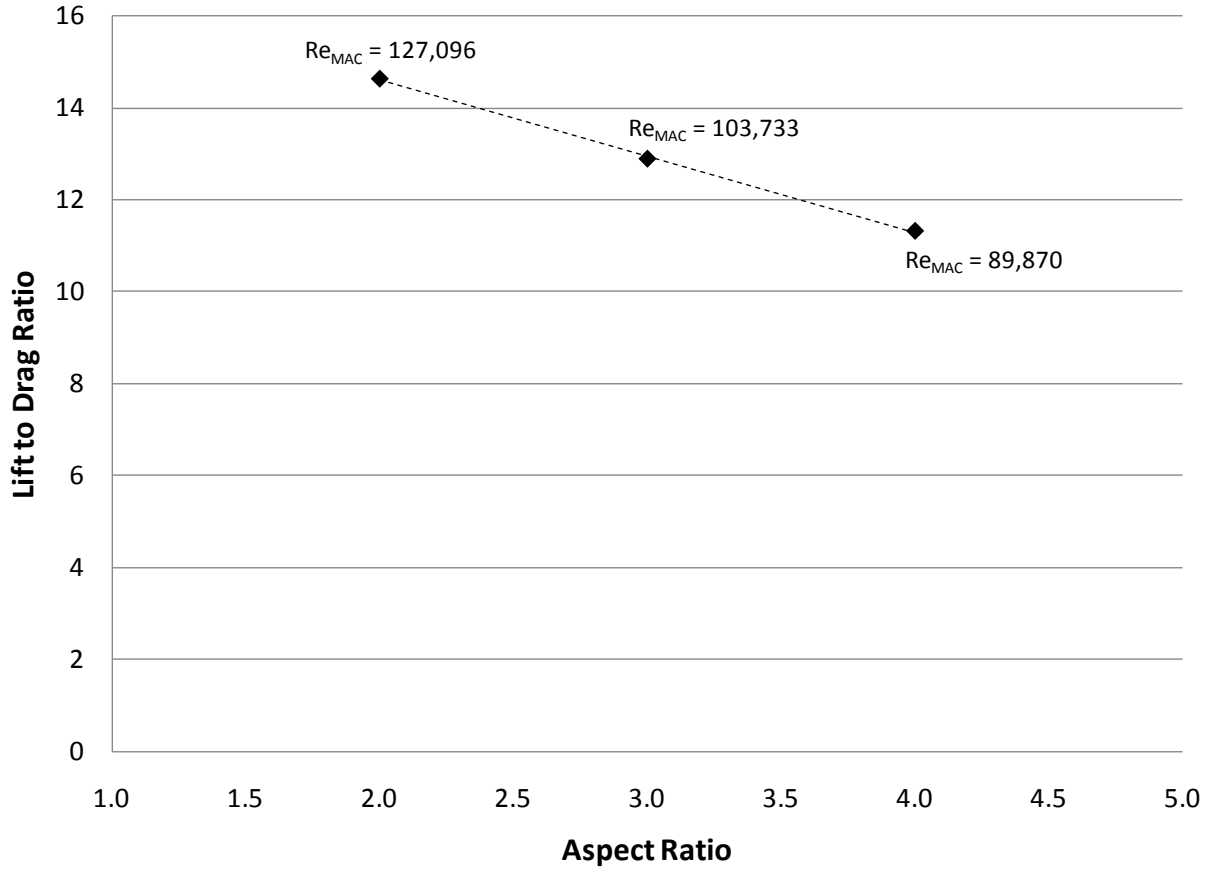

Figure 7-30: Inverse Correlation Between Aspect Ratio and Lift-to-drag Ratio and Direct Correlation Between Lift-to-drag Ratio and Mean Aerodynamic Chord Reynolds Number

Increasing wing loading at this velocity had a positive effect on efficiency, as demonstrated in Figure 7-31. The reference 300 N/m^2 wing loading was the optimum calculated by the classical aerodynamics code discussed in Chapter 6. It is apparent that this was a significant under estimate as performance improves by 11% with a 33% increase in wing loading. Finding the peak of the wing loading tradeoff will permit designs to be sized at or above this point so as to minimize wing loading and simplify the task of collapsing the wings into the stowed geometry. These trends remain qualitatively similar between the MAV scale and in classical theory, though it is possible that the curves are shifted somewhat. No judgment can be made at this time due to the previously discussed limitations with this study.

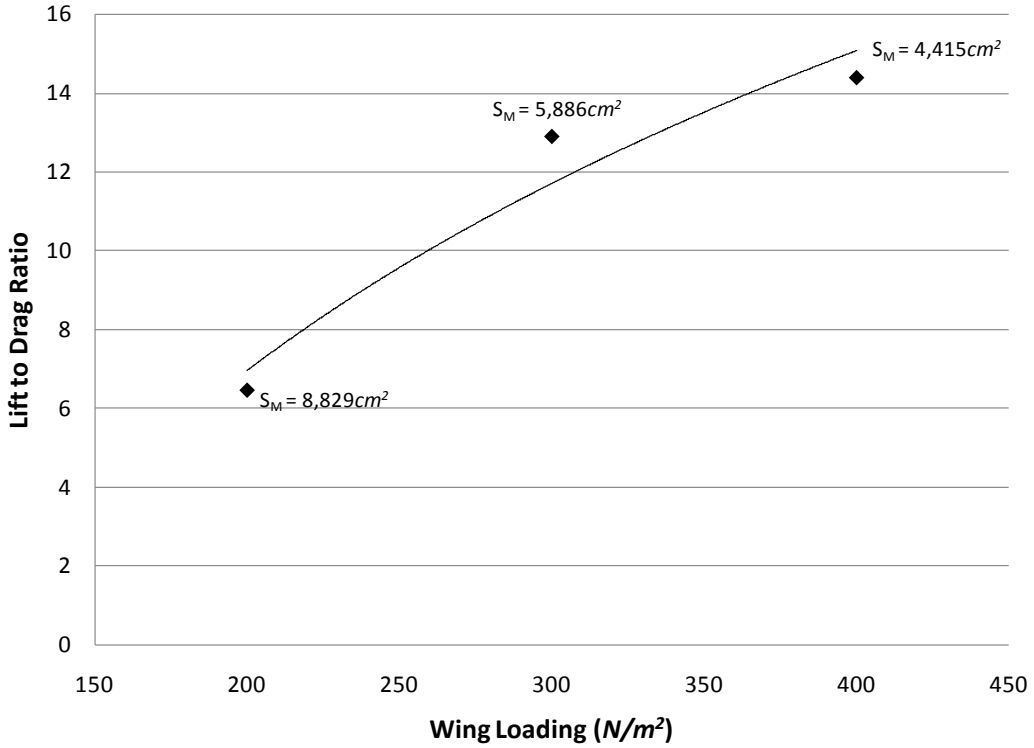

Figure 7-31: Lift-to-drag Ratio Improving Towards Optimum As Wing Loading Increases in Initial Study

Fortunately, from a parameter space perspective, varying the leading edge sweep angle had little effect on the performance of the wing as shown in Figure 7-32. Therefore leading edge sweep may be used to enhance stability by both shifting the aerodynamic center and through the dihedral effect of rear sweep angles. This agrees with classical aircraft design theory though the intensity of the effect of sweep angle on stability may be different at these scales.

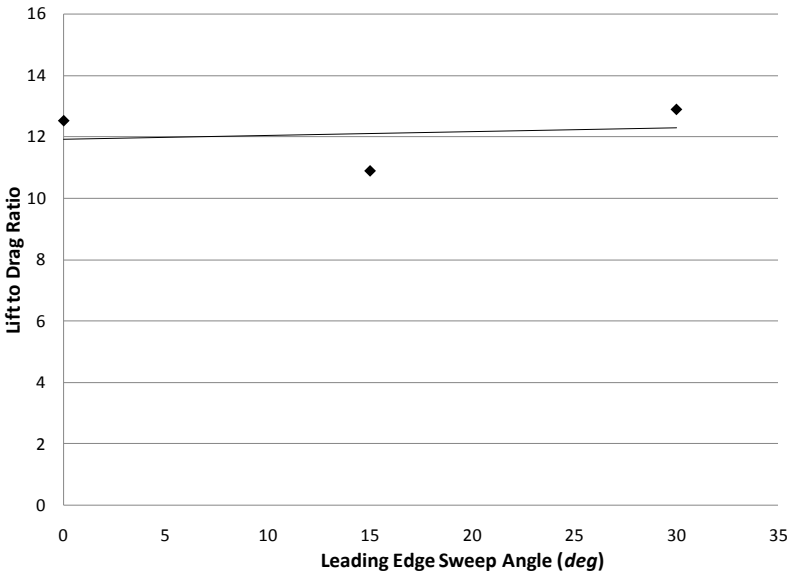

Figure 7-32: Lift-to-drag Ratio Insensitive to Leading Edge Sweep Angle

Classical aerodynamic theory agreed well with the trends observed when varying the taper ratio. Reducing the taper ratio from 1.0 to 0.5 enhanced the lift-to-drag ratio consistently as shown in Figure 7-33. It appears that the classical ideal elliptical lift distribution may well still hold at these scales.

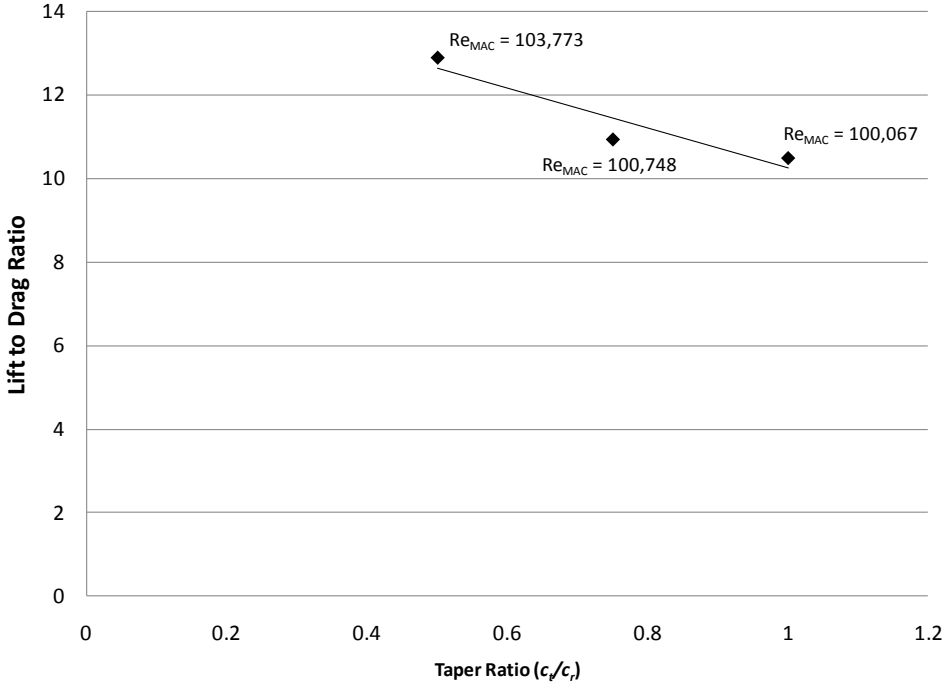

Figure 7-33: Inverse Correlation Between Taper Ratio and Lift-to-drag Ratio

.

Chapter 8 Recommended Preliminary Designs

Based on this work it is possible to recommend two designs for prototyping, wind tunnel validation, and eventual flight tests. This would include the high speed cruise and long endurance configurations and both leaf spring or membrane wing structures will be experimented with. While the work presented here provides excellent starting points, true design optimization will require significant physical experimentation. Determining the complex interactions between large fuselages and low aspect ratio wings at low Reynolds numbers is only one of the problems not yet vetted. With this ground work it is now possible to implement the optimization process outlined in Figure 8-1.

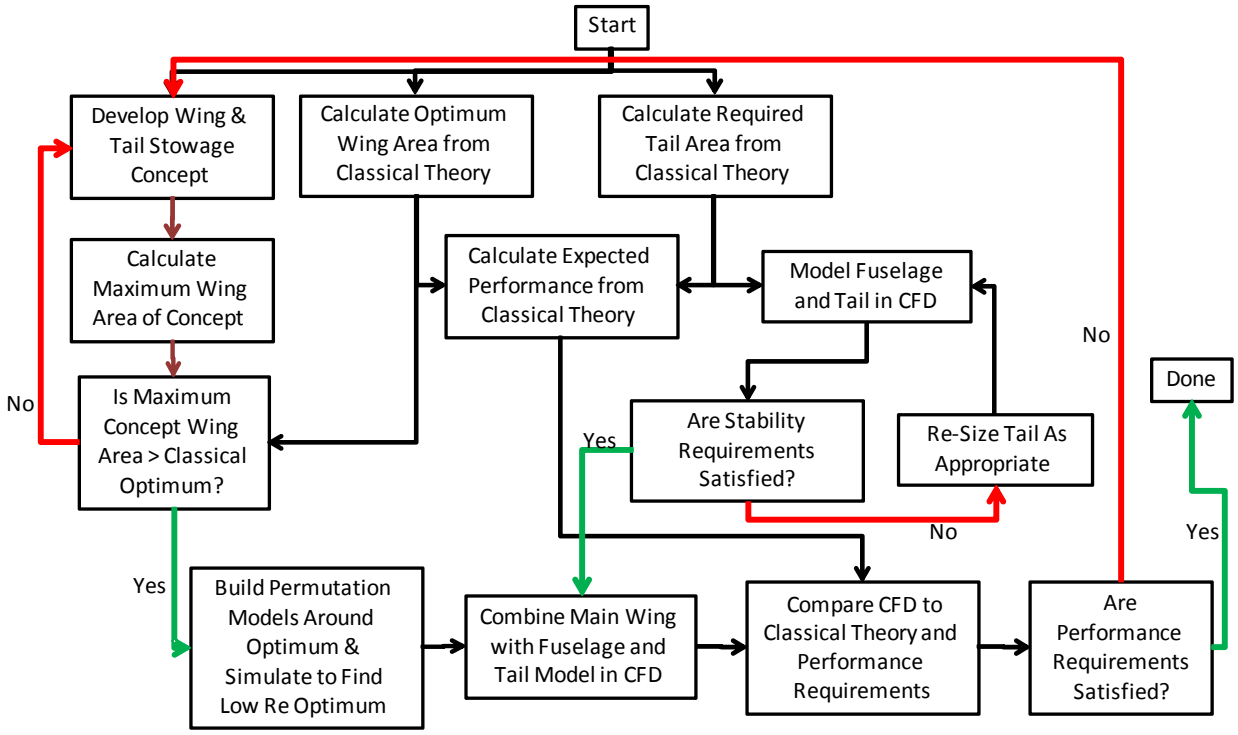

Figure 8-1: Flow Chart of Proposed Optimization Process

8.1 High Speed Cruise Configuration

From a mechanical perspective the high speed cruise mission would be the simplest to implement. Wing areas less than 22% of those required for the long endurance mission will be relatively easy to store. Figure 8-2 provides a simplified sketch of the design with an Ogive tail and appropriate wing areas in a cruciform layout. Figure 8-3 provides an outline of the high speed cruise mission.

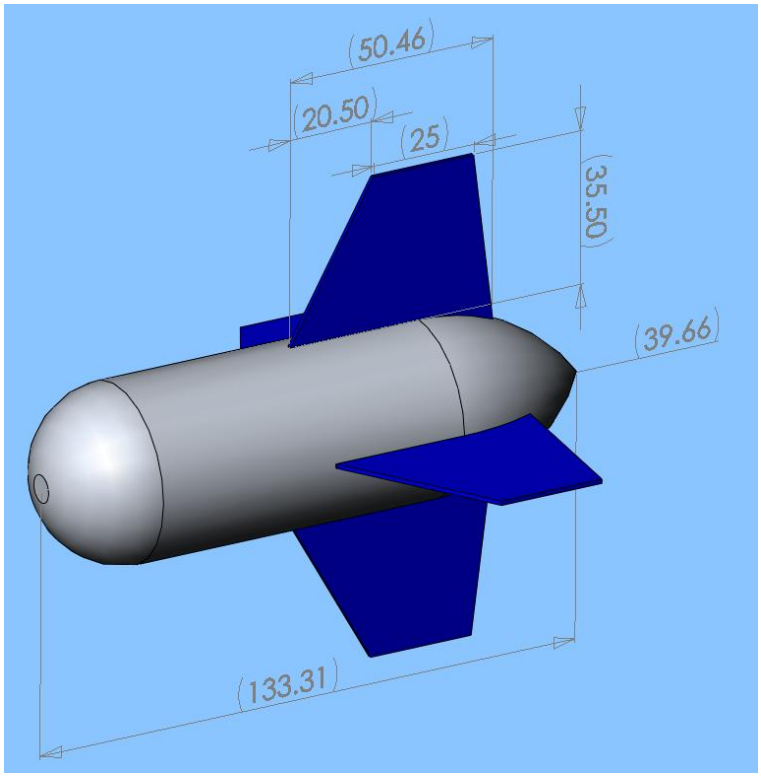

Figure 8-2: High Speed To Target Configuration, (dimensions in *mm*)

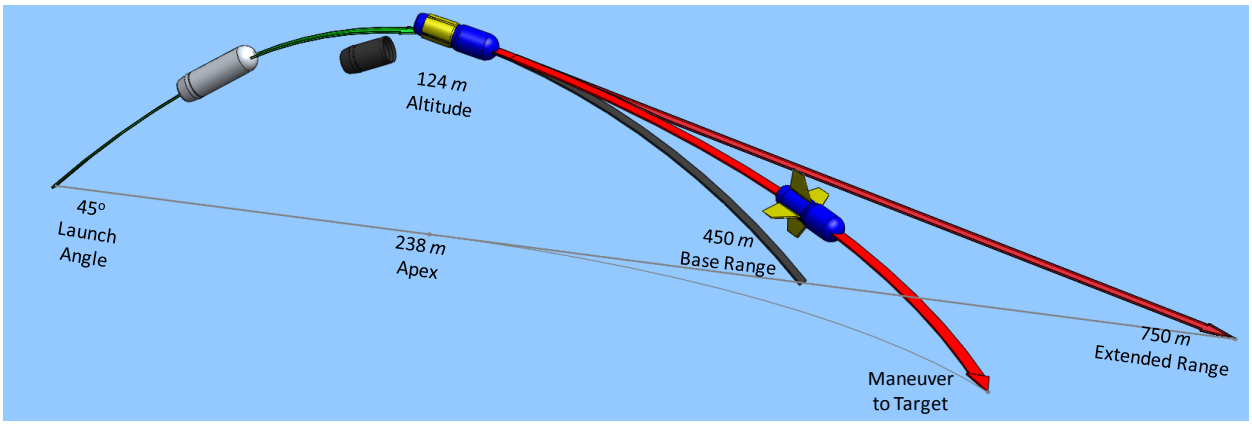

Figure 8-3: High Speed Cruise Mission Profile

At this point preliminary structural design and prototyping are ready to begin for both the membrane and leaf spring structures. Conceptual packaging designs for both are shown in Figure 8-4 and Figure 8-5. These initial models, with hemispherical tails, retain nearly 130,000 mm^3 of usable fuselage volume out of the 161,000 mm^3 provided by the stowed geometry, or 82%. More detailed structural design work will be required to implement the designs shown. Both were created to confirm that sufficient volume was available; actuators, catches, and connectors will be designed in the next stage of the project.

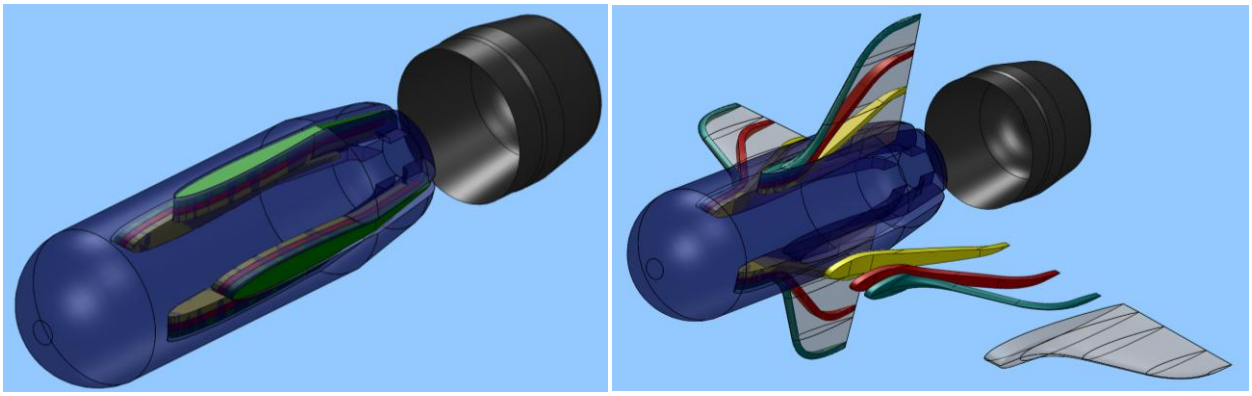

Figure 8-4: High Speed Leaf Spring Structure Concept, Partially Deployed (Left) and Fully Deployed (Right)

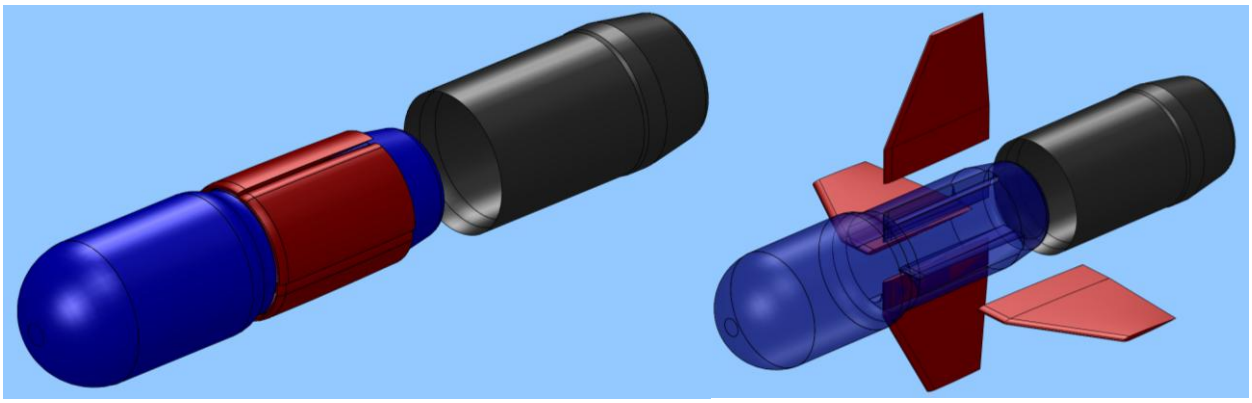

Figure 8-5: High Speed Membrane Wing Structure Concept, Partially Deployed (Left) and Fully Deployed (Right)

As discussed in Chapter 6, the high speed cruise wing area has been fixed at 2,520 mm^2 through a classical aerodynamic optimization analysis. The initial location of the center of gravity will be 50% down the fuselage and coincident with the 20% mean aerodynamic chord location. This should provide a stable platform. However, complex interactions between the nonlinear positive pitching moment of an axisymmetric body and the behavior of low aspect ratio wings at these Reynolds numbers is poorly understood and may cause problems. Significant experimental work will be required.

Prototypes of both the leaf spring and membrane structures should now be created since conceptual modeling and analysis have reached their limits. Wind tunnel experimental results will be required to improve efficiency and stability.

The expected performance for the high-speed design is presented in Table 8-1. Performance was calculated for both the high-drag baseline fuselage (C_D = 0.155) and an idealized, streamlined version (C_D = 0.100). It is interesting to note that the range only increased by 88 *m* (13%) when the fuselage drag coefficient was dropped by 35%.

Table 8-1: Sizes and Expected Performance of High Speed MAV

Launch Information			Wing Planform Information			Performance, $C_{do\ Fuse} = 0.155$			Performance, $C_{do\ Fuse} = 0.100$		
Launch Angle	45	*deg*	Wing Loading	700	N/m^2	Main Wing α_{TRIM}	8.8	*deg*	Main Wing α_{TRIM}	8.8	*deg*
Apex Velocity	45	*m/s*	Wing Area	2,523	mm^2	Glideslope	16.3	*deg*	Glideslope	13.6	*deg*
Apex Altitude	124	*m*	LE Location	68.4	*mm*	Range	663	*m*	Range	751	*m*
Apex Range	238	*m*	Root Chord	47.4	*mm*	Gliding Time	9.84	*s*	Gliding Time	11.7	*s*
Ballistic Time	10	*s*	Tip Chord	23.7	*mm*	RE_{MAC}	113,460		RE_{MAC}	113,460	
$C_{D\ o\ Fuselage}$	0.155		Span	71	*mm*	L/D	3.42		L/D	4.1	

8.2 Long Endurance Configuration

Preliminary structural designs of the long endurance configuration have been developed as well. Sections 3.1.1.3 and 3.1.3.3 showed that sufficient wing area for the long endurance mission can be compacted into the stowed geometry. However, these models are not as certain or detailed as those of the high speed configuration due to the increased wing area exacerbating any unforeseen packing problems. Packing issues should be explored first with the high speed design before continuing work on the long endurance version. Figure 8-6 provides a schematic showing dimensions of a characteristic trapezoidal planform for this variant. Several features should be noted:

- High-wing improves lateral stability characteristics
- Near total masking of fuselage by the main wing should reduce non-linear axisymmetric body pitching moment behavior but will need to be tested
- Clean transition between wing and upper fuselage should smooth air flow over the wing upper surface and increase efficiency as found by Kellog et al. (2001) in the design of the NRL MITE 2. The wing should be mounted so that the upper surface of the airfoil extends above the upper surface of the fuselage.

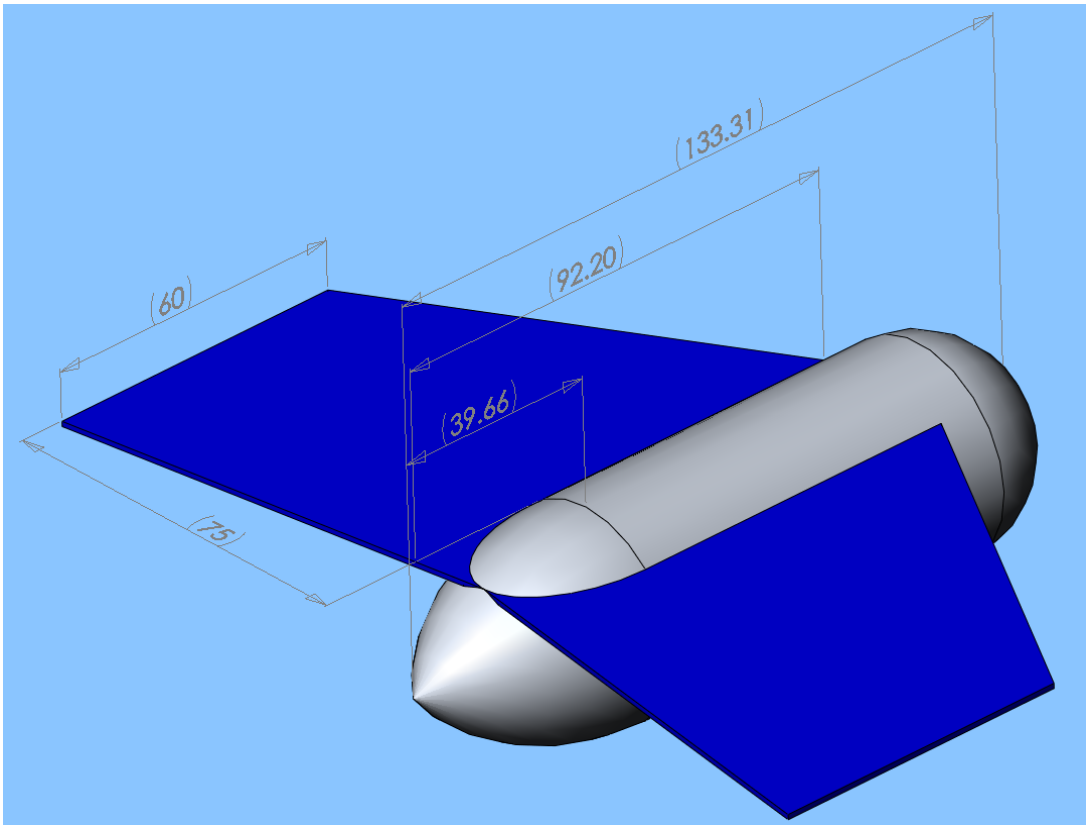

Figure 8-6: Long Endurance Concept, Dimensions in mm

Figure 8-7 and Figure 8-8 provide some detail of both the leaf spring and wrapped membrane structures for the larger wing area of this configuration. These designs are less certain as unforeseen manufacturing difficulties encountered in the prototyping of the high-speed variants will be more pronounced when applied to the larger wing. A final leaf spring system would require a thinner airfoil than the NACA 0009 used in the model presented.

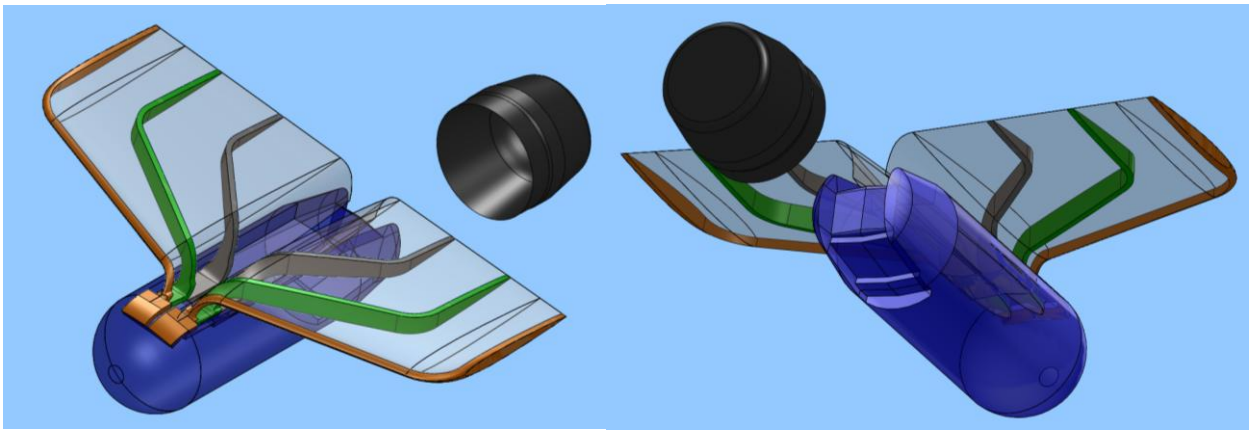

Figure 8-7: Long Endurance Configuration Leaf Spring Structure, Top Left Front Quarter (Left), Bottom Right Rear Quarter (Right)

Major modifications, of both the leaf spring and membrane wing structures, were necessary to stow the 467% increase in wing area. Collapsing the leafs directly aft would have caused the elements to run into one another. A gull-wing arrangement mounted to the top of the fuselage allowed the leaves to wrap from the upper to lower surfaces parallel to one another without conflict as shown on the right of Figure 8-7.

Storing the membrane wing unfortunately required the addition of a pair of thin shields covering the vast majority of the fuselage (grey components in Figure 8-8). These were necessary to protect the fragile exterior surface of the membrane from the launch tube. A long rear casing, a modification of that used for the high-speed version seemed more likely to jam during deployment. Fortunately the aspect ratio 2 wing has a span sufficiently short that the slot discussed in Section 3.1.2 to enable large wing spans was not required for this design. The inner-wrapped wing ends just short of the root chord of the outer wing wrap when stowed.

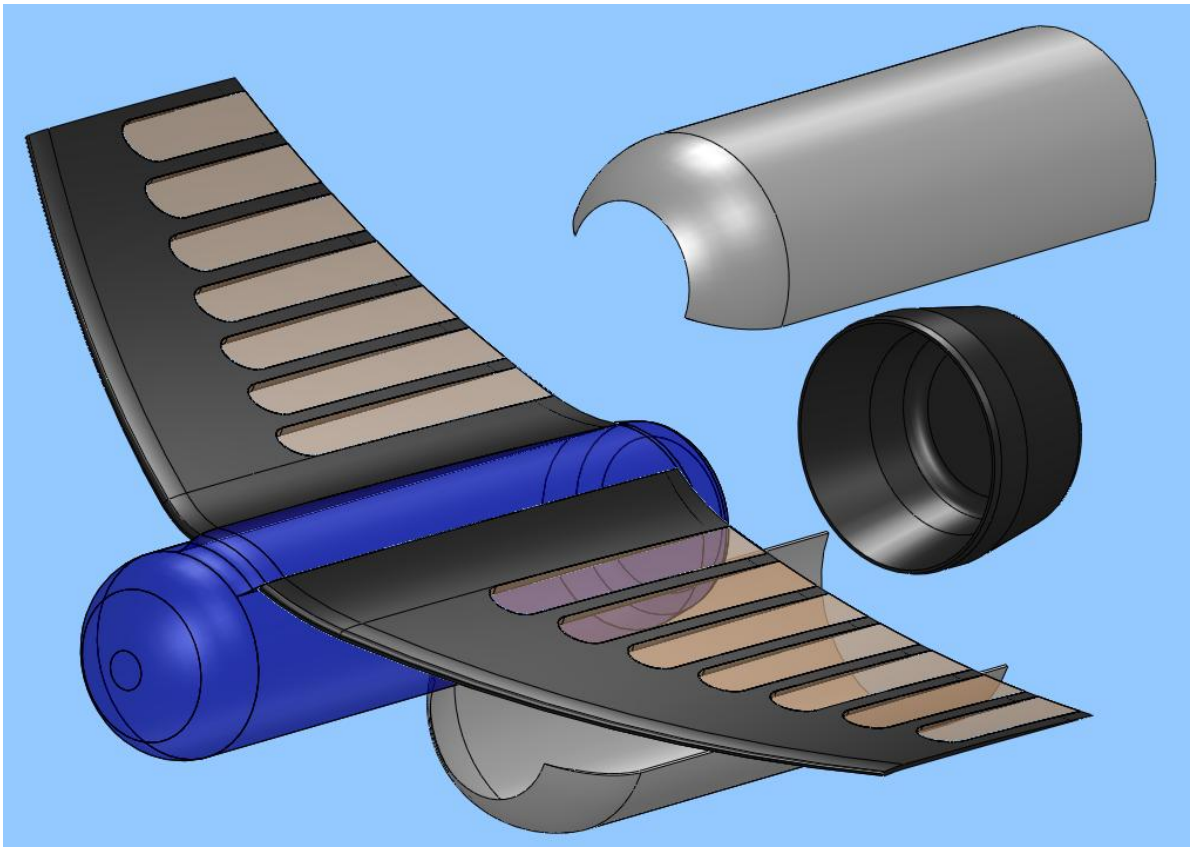

Figure 8-8: Long Endurance Configuration Wrapped Membrane Structure

Expected performance of this configuration is presented in Table 8-2. Again note that a 35% reduction in fuselage drag ratio only provides another 104 *m* of range, 6.6%. Figure 8-9 presents a schematic of the low speed cruise mission profile with an emphasis on moderate endurance over-the-hill surveillance.

Table 8-2: Sizes and Expected Performance of Long Endurance MAV

Launch Information			**Planform Information**			**Performance, $C_{do\ Fuse}$ = 0.155**			**Performance, $C_{do\ Fuse}$ = 0.100**		
Launch Angle	73	*deg*	Wing Loading	150	N/m^2	Main Wing α_{TRIM}	9.86	*deg*	Main Wing α_{TRIM}	9.86	*deg*
Apex Velocity	20	*m/s*	Wing Area	11,772	mm^2	Glideslope	8.4	*deg*	Glideslope	7.8	*deg*
Apex Altitude	212	*m*	LE Location	7.46	*mm*	Range	1,576	*m*	Range	1,680	*m*
Apex Range	132	*m*	Root Chord	102.3	*mm*	Gliding Time	73	*s*	Gliding Time	78	*s*
Ballistic Time	12.9	*s*	Tip Chord	51.1	*mm*	RE_{MAC}	108,930		RE_{MAC}	108,930	
$C_{D\ o\ Fuselage}$	0.155		Span	153.4	*mm*	L/D	6.8		L/D	7.3	

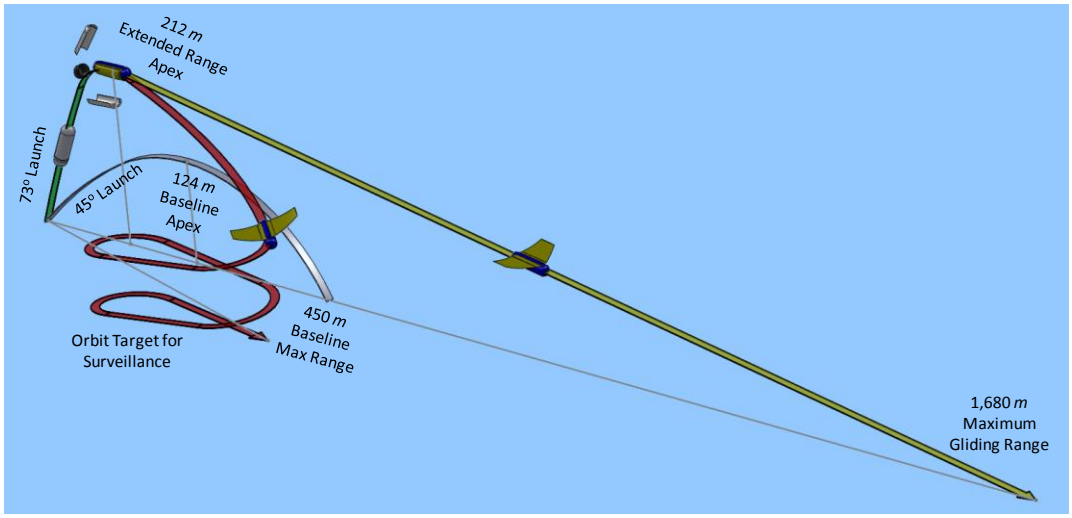

Figure 8-9: Schematic of Long Endurance Mission Profile

Chapter 9 Summary and Recommendations

This work has shown that an effective micro air vehicle can be stowed within a small, rugged, cylindrical volume. In addition the same MAV can perform a useful mission while gliding from the apex of a ballistic arc.

A survey of prior art showed that the projected flight regime of this aircraft would be well outside the usual MAV cruise performance envelope. This survey also indicated that power supplies, communication systems, actuators, and sensors have all been miniaturized sufficiently to enable the mission concept with the provided geometric constraints. Information collected on low Reynolds number aerodynamics indicated that flow separation and laminar-turbulent transition effects would be encountered, significantly increasing the difficulty of computational modeling and pushing the limits of classical aerodynamic theory. The two primary goals were verifying volumetric feasibility and obtaining reasonable performance predictions.

Digital solid modeling of a series of wing stowage concepts lead to the development of the Leaf Spring and membrane wing structures which enabled significantly greater wing areas and provided approximately 400% more fuselage volume than the sponsor's initial designs. In addition to these two novel structures several methods of control actuation have also been developed. Refinement of the thin curved-plate membrane wings used in earlier MAVS have enabled this structure to incorporate full thick airfoil profiles.

A fundamentally new "leaf spring" structure has also been proposed. This system uses a group of contoured "leaf elements" providing the structural function of both spars and ribs in a conventional wing while collapsing into an extremely small stowed volume. A film skin of Mylar, latex, or similar material would be bonded over the leaf elements to provide the outer surface. Multiple biomimetic morphing techniques could be applied to this structure including adaptive washout and variable sweep angle, wing area, angle of attack, and camber. Continuing work should now focus on physically prototyping both structural concepts and all control actuation methods. Material choice and subtle geometric permutations will be critical in obtaining optimum function and further progress will be extremely slow without physical models.

With the volumetric feasibility verified work progressed to performance estimation and optimization. The semi-empirical Missile DATCOM code developed by the USAF was used to rapidly calculate initial estimates of required stabilizer and wing areas. Initial simulations in Fluent showed that a low aspect ratio delta planform significantly outperformed conventional high aspect ratio wing and tail layouts.

An in-house MATLAB code was developed to calculate optimum delta wing surface areas and longitudinal positions for cruise flight conditions. These cruise conditions were the calculated apex altitude and velocity for a range of launch angles determined from launch data provided by the research sponsors. In addition to returning optimum wing areas, the in-house code calculated total range from ballistic launch, gliding range, total flight time, and gilding flight time as well as the Reynolds number at the mean aerodynamic chord.

CFD analyses of individual components was then conducted in preparation for future verification of the component build-up method at MAV scales. The tradeoff between fuselage drag and volume was determined by shaving the aft end into progressively longer Ogive conics. A 39% reduction in fuselage drag cost 28% of the stowed volume at the approximate point that diminishing returns began to take hold.

Developing a suite of mesh and solver settings capable of providing reasonable preliminary design performance predictions for two dimensional airfoils between Reynolds numbers of 60,000 and 300,000 consumed significant time. An examination of all Fluent 12 turbulence models was conducted. This provided a small subset of the 51 studied permutations capable of predicting the lift, drag, and lift-to-drag ratio of a NACA 0009 airfoil at 6^{o} angle of attack within $\pm$10%. Each of these models was then used to generate entire drag polars for the 0009. Finally the k-ω SST model was selected due to its simplicity of implementation, and speed of calculation. Future computational work should initially focus on improving flow modeling performance by modifying model constants of the k-ω SST model. Should this fail to improve results alternate low Reynolds transition models may need to be examined. Once that work is completed a second three dimensional planform study should be performed with the new mesh settings and turbulence model.

A three dimensional planform study was conducted prior to realizing the intricacies of modeling this transitional flow. Despite this the general trends obtained were very strong, and while specific values are likely not accurate the qualitative information obtained was extremely useful. The effects of varying wing loading, taper ratio, and sweep angle all followed the trends shown in classical theory. This was important since wing loading has a primary effect on optimum cruise while taper ratio directly effects planform efficiency and sweep angle is critical for obtaining longitudinal stability of a delta design. However, increasing aspect ratio did not follow the classical trend.

Over the range of aspect ratios studied: 2, 3, and 4, the lift-to-drag ratio actually fell as the aspect ratio was increased, which is contrary to classical wing theory. Calculating the mean aerodynamic chord Reynolds number for each case provided the explanation. At an aspect ratio of 2 the mean aerodynamic chord Reynolds number was 127,096 which fell to 89,870 as the aspect ratio was increased to 4. In this critical transitional region smooth airfoils are extremely sensitive to falling Reynolds numbers. Future work should implement the revised mesh and solver settings developed for the two dimensional work and study a larger range of aspect ratios, down to 0.5 or less, to find the point at which increasing induced drag outweighs the benefits of increasing chordwise Reynolds number. It would also be interesting to examine several airfoils to determine whether the aspect ratio / Reynolds number tradeoff point is profile dependent to any significant degree. Several alternate MAV planforms such as circular, elliptical, and trochoidal layouts should also be examined. Wing-body effects between the low aspect ratio planforms and large fuselage will also need investigated.

The primary conclusion of this work is that the initial concept is entirely practicable from volumetric and aerodynamic perspectives. However, the initial performance goals were not optimal from either of those engineering design viewpoints. Proposals for two more optimal designs have been made including a high-speed cruise variant capable of a 66% range extension, and a long-endurance configuration capable of gliding times greater than 60*s*. Much physical and computational work remains to be done prior to deploying a fully functional system but the initial groundwork has been completed and is very promising.

References

Appich, W. H., & Wittmeyer, R. E. (2001). Aerodynamic Effects of Body Slots on a Guided Projectile with Cruciform Surfaces. *Journal of Spacecraft , VOL. 17, NO. 6*, 522-528.

Blake, W. B. (1998). *Missile DATCOM User's Manual - 1997 FORTRAN 90 Revision.* Wright-Patterson Air Force Base: Air Force Research Laboratory, Air Vehicles Directorate.

Bourlett, S. P. (1997). *Patent No. 5,615,847.* United States.

Carlucci, D. E., & Jacobson, S. S. (2008). *Ballistics: Theory and Design of Guns and Ammunition.* Boca Raton, FL: CRC Press.

Davis, W. R., Kosicki, B. B., Boroson, D. M., & Kostishack, D. F. (1996). Micro Aerial Vehicles for Optical Surveillance. *The Lincoln Laboratory Journal , VOL. 9, NO. 2*, 194-214.

Fleming, G. A., Bartram, S. M., Waszak, M. R., & Jenkins, L. N. (2001). Projection Moire Interferometry Measurments of Micro Air Vehicle Wings. *Proceedings of the SPIE International Symposium on Optical Science and Technology.* San Diego, CA: SPIE.

Grabowsky, J. (2007). AeroVironment Future Solutions - ISR. *Pacific Theater Operational Science and Technology Conference.*

Guiler, R. W. (2007). *Control of a Swept Wing tailless Aircraft Through Wing Morphing.* Morgantown WV: West Virginia University.

Ifju, P. G., Ettinger, S., Jenkins, D., & Martinez, L. (2001). Composite Materials for Micro Air Vehicles. *Proceedings of the SAMPE Annual Conference* (pp. 7-12). Long Beach, CA: University of Florida Mechanics and Engineering Science Department.

Kellogg, J., Bovias, C., Dahlburg, J., Foch, R., Gardner, J., Gordon, D., et al. (2001). *The NRL MITE Air Vehicle.* US Naval Research Laboratory.

Kemp, I. (2007, February). The Infantry's Explosive Punch: 40 mm Grenades and Launchers. *Asian Military Review* , pp. 17-23.

Kim, D.-H., Yang, J.-H., Chang, J.-W., & Chung, J. (2009). Boundary Layer and Near-wake Measurments of NACA 00012 Airfoil at Low Reynolds Numbers. *47th AIAA Aerospace Sciences Meeting Including the New Horizons Forum and Aerospace Exposition.* Orlando, FL: AIAA.

Krashanitsa, R., Platanits, G., & Silin, D. (2006). Auopilot Integration into Micro Air Vehicles. In J. Schetz, *Introduction to the Design of Fixed-Wing Micro Air Vehicles* (pp. 109-149). Reston, VA: American Institute of Aeronautics and Astronautics, Inc.

Lian, Y., & Shyy, W. (2007). Laminar-Turbulent Transition of a Low Reynolds Number Rigid or Flexible Airfoil. *AIAA Journal , VOL. 45, NO. 7*, 1501-1513.

Lissman, P. B. (1983). Low-Reynolds Number Airfoils. *Annual Review of Fluid Mechanics , VOL. 15*, 223-239.

Lockheed Martin. (2010). *Hellfire II Missile*. Retrieved April 28, 2010, from Lockheed Martin: http://www.lockheedmartin.com/products/HellfireII/index.html

Lyon, D. H. (2003). *Mortar-Launched Recon-Targeting Programs.* Army Research Lab, Ballistics and Weapons Concepts Division.

Martorana, R. T., Anderson, J., Spearing, S. M., Kessler, S., Appleby, B., Bergmann, E., et al. (2003). *Patent No. 2003/0089820 A1.* United States.

Morris, S. J. (1997). *Design and Flight Test Results for Micro-Sized Fixed-Wing and VTOL Aircraft.* Palo Alto, CA: MLB Company.

Morris, S. J. (2000). *Design of Micro Air Vehicles and Flight Test Validation.* Palo Alto, CA: MLB Company.

Mueller, T. J. (1999). Aerodynamic Measurments at Low Reynolds Numbers for Fixed Wing Micro Air Vehicles. *Development and Operation of UAVs for Military and Civil Applications.* Belgium: University of Notre Dame.

Mueller, T. J., & Batill, S. (1982). Experimental Studies of Separation on a Two-Dimensional Airfoil at Low Reyolds Numbers. *AIAA Journal , VOL. 20, NO. 4*, 457-463.

Mueller, T. J., Torres, G. E., & Srull, D. W. (2006). Elements of Aerodynamics, Propulsion, and Design. In J. A. Schetz, *Introduction to the Design of Fixed-Wing Micro Air Vehicles* (pp. 39-107). Reston, VA: American Institute of Aeronautics and Astronautics, Inc.

Ott, J., & Biezad, D. (2004). Design of a Tube-Launched UAV. *Proceedings of the AIAA 3rd Unmanned Unlimited Conference* (pp. 540-550). Chicago, IL: AIAA.

Palmer, M. R. (2001). *Patent No. 6,260,797.* United States.

Pepper, W. B., & Fellerhoff, R. D. (1969). Parachute System to Recover Spinning Shell Subjected to 20,000 g's. *Journal of Spacecraft , VOL. 6, NO. 3*, 344-346.

Pornsin-sirirak, T. N., Tai, Y. C., & Ho, C. M. (2001). Titanium-alloy MEMS wing technology for a micro air vehicle aplication. *Sensors and Actuators , VOL. A 89*, 95-103.

Raymer, D. P. (2006). *Aircraft Design: A Conceptual Approach, Fourth Edition.* Reston, VA: American Institute of Aeronautics and Astronautics.

Raythoeon Corporation. (2009). *Raytheon Excalibur Datasheet.* Raytheon Corporation.

Roberts, W. B. (1980). Calculation of Laminar Separation Bubbles and Their Effect on Airfoil Performance. *AIAA Journal , VOL. 18, NO. 1*, 25-31.

Ruffier, F., Viollet, S., Amic, S., & Franeschini, N. (2003). Bio-Inspired Optical Flow Circuits for the Visual Guidance of Micro Air Vehciles. *Proceedings of the IEEE Symposium on Circuits and Systems* (pp. 846-849). Bangkok, Thiland: IEEE.

Sachs, G. (2007). Why Birds and Miniscale Airplanes Need No Vertical Tail. *Journal of Aircraft , VOL. 44, NO. 4*, 1159-1167.

Selig, M. S., Donovan, J. F., & Fraser, D. B. (1989). *Airfoils at Low Speeds.* Virginia Beach, VA: H. A. Stokely Publishing.

Shyy, W., Ifju, P., & Vieru, D. (2005). Membrane Wing-based Micro Air Vehicles. *Applied Mechanics Reviews* , 283-301.

Shyy, W., Lian, Y., Tang, J., Viieru, D., & Liu, H. (2008). *Aerodynamics of Low Reynolds Number Flyers.* New York, NY: Cambridge University Press.

Silton, S. I. (2005). Navier-Stokes Computations for a Spinning Projectile from Subsonic to Supersonic Speeds. *Journal of Spacecraft and Rockets , VOL. 42, NO. 2*, 223-231.

Silton, S. I., & Dinavahi, S. P. (2008). Base Drag Considerations on a 0.50-caliber Spinning Projectile. *Proceedings of the 26th AIAA Applied Aerodynamics Conference.* Honolulu, HI: AIAA.

Simons, M. (1999). *Model Aircraft Aerodynamics; Fourth Edition.* Poole, Dorset, UK: Special Interest Model Books Ltd.

Stanford, B., Abdulrahim, M., Lind, R., & Ifju, P. (2007). Investigation of Membrane Actuation for Roll Control of a Micro Air Vehicle. *Journal of Aircraft , VOL. 44, NO. 3*, 741-749.

Torres, G., & Mueller, T. J. (2001). *Micro Aerial Vehicla Development: Design, Components, Fabrication, and Flight Testing.* Notre Dame: University of Notre Dame.

US Army Armament Ballistic Research Laboratory. (1984). *Flight Data on Liquid-Filled Shell for Sipin-Up Instabilities.* US Army Armament Ballistic Research Laboratory.

Woodland, R. L. (2000). *Patent No. 6,056,237.* United States.

Appendix A Missile DATCOM Input and Output Files

Missile DATCOM Input File: Comments preceded by "<"

```
$FLTCON                                  < Begin specifying flight conditions
  NALPHA= 3.,                            < Number of angles of attack to be analyzed
  ALPHA= 0.,2.,4.,                       < Angles of attack in degrees
  NMACH=1.,                              < Number of Mach numbers to be analyzed
  MACH=0.131,                            < Mach numbers to be analyzed
  ALT=0.0,                               < Altitude to run analysis in meters
 $END                                    < End flight condition specification
 $REFQ                                   < Specify reference quantities
  SREF= 12.566,                          < Reference Area in square centimeters
  XCG=5.,                                < Center of gravity location
  ROUGH=0.000,                           < Surface roughness characteristic length
  LREF= 4.,$                             < Length
 $AXIBOD                                 < Define axisymmetric body (fuselage)
    TNOSE=OGIVE,                         < Type of nose = Ogive
    LNOSE=2.,                            < Length of nose = 2 cm
    DNOSE=4.,                            < Diameter of nose = 4 cm
    LCENTR=6.1,                          < Length of cylindrical center body = 6.1 cm
    TAFT=OGIVE,                          < Type of tail cone = Ogive
    LAFT=5.3,                            < Length of tail cone = 5.3 cm
    DAFT=0.001,                          < Diameter of aft end of tail cone = 0.001 cm
    DEXIT=0.,$                           < Close diameter = 0
$FINSET1                                 < First fin set in the axial direction
    SECTYP=NACA-1-4-0008                 < Airfoil section = NACA 0008
    SSPAN=2.0,14.5,CHORD=3.65,3.65,      < Semi-Span from axis and chord at specified locations
    XLE=6.25,SWEEP=0.0,STA=0.0,          < Leading edge location, sweep angle,
    NPANEL=2.,                           < Number of fins
    PHIF=90.,270.,$                      < Angle of fins around body from vertical
 $FINSET2                                < Second fin set
    SECTYP=NACA-1-4-0008                 < Airfoil section = NACA 0008
    SSPAN=2.0,6.,CHORD=2.92,2.92,        < Semi span from axis and chord at semi-span locations
    XLE=10.34,SWEEP=0.0,STA=0.0,         < Leading edge location and sweep angle
    NPANEL=4.,                           < Number of fins
    PHIF=45.,135.,225.,315.,$            < Angle of fins around body from vertical
$DEFLCT                                  < Fin deflection Angles
   DELTA1=1.,-1.0,                       < Main wings set to 1 degree angle of attack
   DELTA2=0.,0.,0.,0.                    < Tails set to no angle of attack
CASEID  CASE WVU                         < Case name
BUILD                                    < Build data
DERIV DEG                                < Report derivatives in degrees instead of radians
PART
DIM CM
SOSE
NO LAT
NEXT CASE
```

Missile DATCOM Output File, Important quantities in bold

```
1      ***** THE USAF AUTOMATED MISSILE DATCOM * REV 07/07 *****
           AERODYNAMIC METHODS FOR MISSILE CONFIGURATIONS

   CONERR - INPUT ERROR CHECKING

   ERROR CODES - N* DENOTES THE NUMBER OF OCCURENCES OF EACH ERROR
   A - UNKNOWN VARIABLE NAME
   B - MISSING EQUAL SIGN FOLLOWING VARIABLE NAME
   C - NON-ARRAY VARIABLE HAS AN ARRAY ELEMENT DESIGNATION - (N)
   D - NON-ARRAY VARIABLE HAS MULTIPLE VALUES ASSIGNED
   E - ASSIGNED VALUES EXCEED ARRAY DIMENSION
   F - SYNTAX ERROR

   ************************* INPUT DATA CARDS *************************

  1  $FLTCON
  2   NALPHA= 3.,
  3   ALPHA= 0.,2.,4.,
  4   NMACH=1.,
  5   MACH=0.131,
  6   ALT=0.0,
  7  $END
  8  $REFQ
  9   SREF= 12.566,
 10   XCG=6.65,
 11   ROUGH=0.000,
 12   LREF= 4.,$
 13  $AXIBOD
 14      TNOSE=OGIVE,
             ** SUBSTITUTING NUMERIC FOR NAME OGIVE
 15      LNOSE=2.,
 16      DNOSE=4.,
 17      LCENTR=6.1,
 18      TAFT=OGIVE,
             ** SUBSTITUTING NUMERIC FOR NAME OGIVE
 19      LAFT=5.3,
 20      DAFT=0.001,
 21      DEXIT=0.,$
 22 CASEID  CASE WVU
 23 BUILD
 24 DERIV RAD
 25 PART
 26 DIM CM
 27 SOSE
 28 NO LAT
 29 NEXT CASE
    30 ** BLANK CARD - IGNORED

1        ***** THE USAF AUTOMATED MISSILE DATCOM * REV 07/07 *****    CASE   1
             AERODYNAMIC METHODS FOR MISSILE CONFIGURATIONS         PAGE   1
   CASE INPUTS
   FOLLOWING ARE THE CARDS INPUT FOR THIS CASE

  $FLTCON
   NALPHA= 3.,
   ALPHA= 0.,2.,4.,
   NMACH=1.,
   MACH=0.131,
   ALT=0.0,
```

```
 $END
 $REFQ
  SREF= 12.566,
  XCG=6.65,
  ROUGH=0.000,
  LREF= 4.,$
 $AXIBOD
    TNOSE=1.,
    LNOSE=2.,
    DNOSE=4.,
    LCENTR=6.1,
    TAFT=1.,
    LAFT=5.3,
    DAFT=0.001,
    DEXIT=0.,$
CASEID  CASE WVU
BUILD
DERIV RAD
PART
DIM CM
SOSE
NO LAT
NEXT CASE
  * WARNING * CENTER SECTION DEFINED BUT BASE DIAMETER NOT INPUT
          CYLINDRICAL SECTION ASSUMED
  * WARNING * NOSE LENGTH EQUALS BASE RADIUS, SPHERICAL NOSE BLUNTNESS ASSUMED
  THE BOUNDARY LAYER IS ASSUMED TO BE TURBULENT
  THE INPUT UNITS ARE IN CENTIMETERS, THE SCALE FACTOR IS   1.0000
1       ***** THE USAF AUTOMATED MISSILE DATCOM * REV 07/07 *****    CASE   1
          AERODYNAMIC METHODS FOR MISSILE CONFIGURATIONS         PAGE   2
                        CASE WVU
                  AXISYMMETRIC BODY DEFINITION

                     NOSE   CENTERBODY     AFT BODY       TOTAL
  SHAPE              OGIVE     CYLINDER       OGIVE
  LENGTH              2.000       6.100       5.300      13.400  CM
  FINENESS RATIO      0.500       1.525       1.325       3.350
  PLANFORM AREA       6.281      24.400      14.529      45.210  CM**2
  AREA CENTROID       1.152       5.050      10.125       6.140  CM
  WETTED AREA        25.131      76.655      48.077     149.863  CM**2
  VOLUME             16.753      76.655      36.936     130.344  CM**3
  VOL. CENTROID       1.250       5.050       9.806       5.909  CM

  NOSE IS SPHERICALLY BLUNTED, BLUNTNESS RATIO =1.0000
                     MOLD LINE CONTOUR

   LONGITUDINAL STATIONS    0.0000    0.2000    0.4000    0.6000    0.8000
     1.0000    1.2000    1.4000    1.6000    1.8000    2.0000    2.6100
     3.2200    3.8300    4.4400    5.0500    5.6600    6.2700    6.8800
     7.4900    8.1000    8.6300    9.1600    9.6900   10.2200   10.7500
    11.2800   11.8100   12.3400   12.8700   13.4000

          Z-OFFSET    0.0000    0.0000    0.0000    0.0000    0.0000
     0.0000    0.0000    0.0000    0.0000    0.0000    0.0000    0.0000
     0.0000    0.0000    0.0000    0.0000    0.0000    0.0000    0.0000
     0.0000    0.0000    0.0000    0.0000    0.0000    0.0000    0.0000
     0.0000    0.0000    0.0000    0.0000    0.0000

         BODY RADII    0.0000    0.8718    1.2000    1.4283    1.6000
     1.7321    1.8330    1.9079    1.9596    1.9900    2.0000    2.0000
     2.0000    2.0000    2.0000    2.0000    2.0000    2.0000    2.0000
     2.0000    2.0000    1.9825    1.9297    1.8409    1.7149    1.5498
```

```
     1.3430    1.0908    0.7883    0.4283    0.0005
1       ***** THE USAF AUTOMATED MISSILE DATCOM * REV 07/07 *****    CASE   1
           AERODYNAMIC METHODS FOR MISSILE CONFIGURATIONS         PAGE   3
                        CASE WVU
                    BODY ALONE PARTIAL OUTPUT

     ******* FLIGHT CONDITIONS AND REFERENCE QUANTITIES *******
    MACH NO  =      0.13             REYNOLDS NO = 3.037E+06 /M
    ALTITUDE =       0.0 M        DYNAMIC PRESSURE =   1217.19 N/M**2
    SIDESLIP =      0.00 DEG              ROLL =      0.00 DEG
    REF AREA =     12.566 CM**2       MOMENT CENTER =     6.650 CM
    REF LENGTH =     4.00 CM         LAT REF LENGTH =     4.00 CM

     ALPHA    CA-FRIC  CA-PRES/WAVE CA-BASE    CA-PROT     CA-SEP     CA-ALP
      0.00     0.0642     0.1173     0.0000                0.0000
      2.00     0.0641     0.1172     0.0000                0.0003
      4.00     0.0639     0.1168     0.0000                0.0013

              CROSS FLOW DRAG PROPORTIONALITY FACTOR = 0.61239

     ALPHA    CN-POTEN  CN-VISC   CN-SEP    CM-POTEN  CM-VISC   CM-SEP    CDC
      0.00     0.000     0.000             0.000     0.000           0.740
      2.00     0.000     0.002             0.181     0.000           0.743
      4.00     0.000     0.008             0.361     0.001           0.746
1       ***** THE USAF AUTOMATED MISSILE DATCOM * REV 07/07 *****    CASE   1
           AERODYNAMIC METHODS FOR MISSILE CONFIGURATIONS         PAGE   4
                        CASE WVU
                  STATIC AERODYNAMICS FOR BODY ALONE

     ******* FLIGHT CONDITIONS AND REFERENCE QUANTITIES *******
    MACH NO  =      0.13             REYNOLDS NO = 3.037E+06 /M
    ALTITUDE =       0.0 M        DYNAMIC PRESSURE =   1217.19 N/M**2
    SIDESLIP =      0.00 DEG              ROLL =      0.00 DEG
    REF AREA =     12.566 CM**2       MOMENT CENTER =     6.650 CM
    REF LENGTH =     4.00 CM         LAT REF LENGTH =     4.00 CM

              ----- LONGITUDINAL -----     -- LATERAL DIRECTIONAL --
       ALPHA      CN       CM       CA       CY      CLN      CLL

        0.00     0.000    0.000    0.182    0.000    0.000    0.000
        2.00     0.002    0.181    0.182    0.000    0.000    0.000
        4.00     0.008    0.362    0.182    0.000    0.000    0.000

       ALPHA      CL       CD      CL/CD     X-C.P.

        0.00     0.000    0.182    0.000-17931.443
        2.00    -0.004    0.182   -0.024    90.858
        4.00    -0.005    0.182   -0.026    45.247

    X-C.P. MEAS. FROM MOMENT CENTER IN REF. LENGTHS, NEG. AFT OF MOMENT CENTER
1       ***** THE USAF AUTOMATED MISSILE DATCOM * REV 07/07 *****    CASE   1
           AERODYNAMIC METHODS FOR MISSILE CONFIGURATIONS         PAGE   5
                        CASE WVU
                  STATIC AERODYNAMICS FOR BODY ALONE

     ******* FLIGHT CONDITIONS AND REFERENCE QUANTITIES *******
    MACH NO  =      0.13             REYNOLDS NO = 3.037E+06 /M
    ALTITUDE =       0.0 M        DYNAMIC PRESSURE =   1217.19 N/M**2
    SIDESLIP =      0.00 DEG              ROLL =      0.00 DEG
    REF AREA =     12.566 CM**2       MOMENT CENTER =     6.650 CM
    REF LENGTH =     4.00 CM         LAT REF LENGTH =     4.00 CM
```

---------- DERIVATIVES (PER RADIAN) ----------

ALPHA	CNA	CMA	CYB	CLNB	CLLB
0.00	-0.0003	5.1961			
2.00	0.1145	5.1808			
4.00	0.2293	5.1655			

*** END OF JOB ***

Appendix B Grid Generation Details

Fuselage Mesh Independence Settings

	Mesh 1	Mesh 2	Mesh 3
Surface Mesh			
Nodes Around Nose Cone	6	12	20
Nodes Around Body	25	75	125
Nodes Along Body	10	20	40
Nodes Around Tailcone	6	8	20
Surface Geometric Growth Rate From Tail	1.25	1.1	1.05
Maximum Cell Size from Tail	4	2	1
Prismatic Cells			
First Prism Height	1.05	1.05	1.05
Number of Layers	10	10	10
Prism Growthrate	1.05	1.05	1.05
Inner Refinement Region			
Growth Rate	1.01	1.01	1.01
X center	180	180	180
X length	240	240	240
Y length	80	80	80
Z length	80	80	80
Max Volume	10	5	2
Middle Refinement Region			
Growth Rate	1.05	1.05	1.05
X center	250	250	250
X length	600	600	600
Y length	120	120	120
Z length	120	120	120
Max Volume	100	50	25
Outer Refinement Region			
Growth Rate	1.1	1.1	1.1
X center	500	500	500
X length	1500	1500	1500
Y length	300	300	300
Z length	300	300	300
Max Volume	1000	1000	1000
Volume Growth Rate	1.2	1.2	1.2
Cell Count	568,795	749,333	1,460,495
Average Cell Size	19,800	14,489	7,433
Cell Shrink Rate		0.732	0.513
Drag Coefficient	**0.12**	**0.1**	**0.096**
% Change		-16.67%	-4.00%

Two Dimensional NACA 0009 Mesh Independence Settings

Surface Mesh	**Mesh 5**	**Mesh 4**	**Mesh 3**	**Mesh 3 MOD**	**Mesh 2**	**Mesh 1**
Tip & Tail Spacing	0.004C (0.002C	0.002C	0.001C	0.001C (0.00033C	0.0005C	0.00025C
Average Cell Spacing	0.02C	.01C	.005C	.005C	.0025C	.00125C
Prismatic Layer	Last AR	Last AR	Last AR	Last AR	Last AR	Last AR
First Cell Height	0.00005C	0.00005C	0.00005C	0.00005C	0.00005C	0.00005C
Number of Layers	25	25	25	25	40	40
Aspect / Growth Rate	50%	50%	50%	200%	50%	50%
Tetrahedral Domain						
Domain Growth Rate	1.3	1.3	1.3	1.3	1.3	1.3
Refine Growth Rate	1.01	1.01	1.01	1.005	1.01	1.01
Refine X_{center}	2C	2C	2C	2C	2C	2C
Refine X_{length}	7C	7C	7C	7C	7C	7C
Refine Y_{length}	3C	3C	3C	3C	3C	3C
Refine Vol_{max}	400	200	100	50	100	100
Mesh Statistics	Last AR	Last AR	Last AR	Last AR	Last AR	Last AR
Skewness	0.78	0.71	0.72	0.74	0.77	0.75
Average Volume	1,709	1,061	509	358	263	98
Number of Cells	5,266	8,480	17,664	25,110	34,176	91,634
Results						
Angle of Attack	0.08					
C_L	0.0000	0.0000	0.0000	0.0000	0.0000	0.0000
C_D	0.0228	0.0303	0.0301	0.0298	0.0301	0.0301
L/D	0.00	0.00	0.00	0.00	0.00	0.00
Angle of Attack	2.14					
C_L	0.2021	0.1956	0.1955	0.1951	0.1958	0.1949
C_D	0.0234	0.0310	0.0308	0.0306	0.0308	0.0308
L/D	8.65	6.31	6.35	6.38	6.36	6.32
Angle of Attack	4.19					
C_L	0.3990	0.3872	0.3866	0.3856	0.3866	0.3864
C_D	0.0255	0.0335	0.0332	0.0328	0.0332	0.0332
L/D	15.64	11.55	11.65	11.75	11.65	11.63
Angle of Attack	6.22					
C_L	0.5837	0.5683	0.5680	0.5651	0.5680	0.5691
C_D	0.0302	0.0379	0.0377	0.0372	0.0376	0.0377
L/D	19.34	14.98	15.06	15.21	15.09	15.10
Angle of Attack	8.25					
C_L	0.7402	0.7292	0.7312	0.7255	0.7320	0.7322
C_D	0.0403	0.0462	0.0457	0.0449	0.0456	0.0456
L/D	18.38	15.78	16.01	16.14	16.04	16.04

Three Dimensional Main Wing Mesh Independence Settings

Mesh Settings Surface Mesh	Mesh 1	Mesh 2	Mesh 3
LE Cell Spacing	1.35	0.84	0.65
TE Cell Spacing	1.35	0.84	0.65
Tip Cell Count	40	60	75
Tip First Length	0.2	0.2	0.2
Tip Last Length	0.2	0.2	0.2
LE / Te Surface Step Down			
First Row	-	-	-
Growt Rate	-	-	-
Layers	-	-	-
Transition Pattern	-	-	-
Prismatic Layer			
First Cell Height	0.6	0.6	0.6
Number of Layers	5	5	5
Geometric Growth Rate	1	1	1
Pyramid Layer			
Option	Skewness	Skewness	Skewness
Fill Cap	Yes	Yes	Yes
Face Angle	120	120	120
Tetrahedral			
Refinement Growth Rate	1.01	1.01	1.01
Xc	200	200	200
XL	600	600	600
YL	150	150	150
ZL	300	300	300
Vmax	250	100	50
Outer Region Growth Rate	1.2	1.2	1.2
Cell Count	694,639	1,442,986	2,384,412
Max Skewness	0.884	0.869	0.882
Cl	1.708	1.501	1.522
% Change CL	-	12.11%	1.40%
Cd	0.616	0.239	0.268
% Change CD	-	61.18%	12.13%
L/D	2.774	6.280	5.679
% Change L/D	-	126.38%	9.57%

Appendix C Analysis Program Code

Code used to calculate trajectory based on back-calculated launch velocity, drag coefficient, and mass:

```
% Baseline Shell

clear
clc

Range = 450;
CD = 0.133;
d = 0.04006;
gamma = 70.6;
rho = 1.225;
dt = 0.005;
Vl = 71.32;
m = 0.18;
g=9.81;

R = 0;
Y = 0.01;
i = 1;

S = pi/4*d^2;

while Y(i) > 0
   if R == 0
      Vy(i) = Vl*sin(gamma*pi/180);
      Vx(i) = Vl*cos(gamma*pi/180);
   end
   Y(i+1)=Y(i)+Vy(i)*dt;
   R(i+1)=R(i)+Vx(i)*dt;
   if Vy > 0
      Vy(i+1)=Vy(i)-[g+0.5*CD*sin(atan(Vy(i)/Vx(i)))*rho*Vy(i)^2*S/m]*dt;
   else
      Vy(i+1)=Vy(i)-[g-0.5*CD*sin(atan(Vy(i)/Vx(i)))*rho*Vy(i)^2*S/m]*dt;
   end
   Vx(i+1)=Vx(i)-0.5*CD*cos(atan(Vy(i)/Vx(i)))*rho*Vx(i)^2/m*S*dt;
   i=i+1;
end

t = dt*i

subplot(2,1,1),plot(R,Y),xlabel('Range (m)'),ylabel('Altitude (m)')
subplot(2,1,2),plot(R,Vx,R,Vy),xlabel('Range (m)'),ylabel('Velicity (m/s)'),legend('X-Velocity','Y-
Velocity')

for n = 1:1:i-1
```

```
   if Y(n+1)>Y(n)
      Ymax=Y(n+1);
      lmax = n+1;
      Vxcr = Vx(n+1);
   end
end

disp('The apogee altitude is: (m)')
disp(Ymax)
disp('The apogee range is: (m)')
disp(R(lmax))
disp('The apogee velocity is: (m/s)')
disp(Vxcr)

% Ylift = Ymax;
% Vylift = Vy(lmax);
% Vxlift = Vx(lmax);
% Rlift = R(lmax);
% Vtop = Vx(lmax);
% LD = 8.5;
% i=1;
%
% while Ylift(i)>0
%     Ylift(i+1) = Ylift(i)+Vylift(i)*dt;
%     Rlift(i+1) = Rlift(i)+Vxlift(i)*dt;
%     Ax = 0.5*CD*cos(atan(Vylift(i)/Vxlift(i)))*rho*Vxlift(i)^2/m*S;
%     Ay = LD*Ax;
%     Vylift(i+1) = Vylift(i)-(g-Ay)*dt;
%     Vxlift(i+1) = Vxlift(i)-Ax*dt;
%     i=i+1;
% end
```

Classical Aerodynamics Optimization Code

Program Integration Portion:

```
%   Hybrid Projectile Performance Analysis
%   Sub-program: Program Integration
%   By: Shanti Hamburg, 5/27/2009, for Ruggedized Stowable MAV Design Study
%.....

% Clear variables and command window
clear
clc

% Call atmospheric and performance input data
Atmosphere_and_Performance_Input

AR = [2.5];

ARcount = 1;
while ARcount <= max(size(AR))
   AR_M = AR(ARcount);

   Vopt = 1;
   count = 0;
   WS = 25;
   while Vopt < Vcr && count < 100000

      WS = WS+25;

      % Call main wing input data
      Main_Wing_Input
      if count >= 1
         CbarCG = CbarCG_old;
      end
      S_H = -0.0001;
      count2 = 0;
      while S_H/S_M < 0.005 && count2 < 100000000
         % Call horizontal tail input data
         H_Tail_Input

         % Call fuselage performance calculation
%           Fuselage_Performance

         % Call main wing performance calculation
         Main_Wing_Performance

         % Call longitudinal stability and horizontal tail sizing
         Longitude_Stability

         CbarCG = CbarCG-0.00001;

         HM = S_H/S_M;
```

```
        count2 = count2+1;
        if count2 == 100000000
           disp('Error in tal area calculation');
        end
      end
      CbarCG_old = CbarCG;
      S_H_store = S_H;

      % Call combided performance calculation
      Hybrid_Performance
      count = count+1;
      if count == 50000
         disp('Problem with wing loading estimation.');
      end
   end

   S_Mdisp = S_M*100*100;

%    disp('The length from the nose to the center of gravity is: (m)');
%    disp(Xcg)
    Xcgst(ARcount) = Xcg;
%      disp('The main wing area is: (cm^2)');
%      disp(S_Mdisp)
   S_Mst(ARcount) = S_Mdisp;
%    disp('The main wing area is: (cm^2)');
%    disp(S_Mdisp)
%    disp('The main wing aspect ratio is:');
%    disp(AR_M)
%    disp('The design wingloading is: (N/m^2)');
%    disp(WS)
   WSst(ARcount) = WS;

   % Output results
%    disp('The maximum lift-to-drag ratio is:');
%    disp(LDopt);
   LDst(ARcount) = LDopt;
%    disp('The velocity for maximum lift-to-drag ratio is: (m/s)');
%    disp(Vopt);
%    disp('The range from launch altitude at optimum glide is: (m)');
%    disp(Range);
   Rst(ARcount) = Range;
   Tgl = (Range-Ropen)/Vcr
   disp('The time of flight is: (s)');
   disp(t);
%    disp('The Reynolds number at the main wing MAC is:')
%    disp(Recbar_Mopt)
   Rest(ARcount) = Recbar_Mopt;
%    disp('The main wing trimmed angle of attack is: (deg)')
%    disp(Atr)
%
   Xcrst(ARcount) = Xcr_M;
```

```
   crst(ARcount) = cr_M;
   ctst(ARcount) = ct_M;
   bst(ARcount) = b_M;
%    plot(V,LD),xlabel('Velocity (m/s)'),ylabel('Lift-to-drag Ratio'),%legend('Induced Drag','Parasitic
Drag'),axis([10 100 0 max(DI)])
%
%
%     disp('Paused for examination of current results. Press any key to continue.');
%     pause


   ARsave = num2str(AR(ARcount));
   ARsave = ['LD for AR' ARsave '.txt'];
   save (ARsave, 'LD', '-ASCII')
   ARcount
   ARcount = ARcount +1;
   WS
   Range
end
%
% disp('Aspect Ratio')
% disp(AR)
% disp('Main wing leading edge location from nose: (m)')
% disp(Xcrst)
% disp('Root chord length: (m)');
% disp(crst)
% disp('Tip chord length: (m)');
% disp(ctst)
% disp('Main wing span: (m)');
% disp(bst)
% disp('Wing area: (cm^2)');
% disp(S_Mst)
% disp('Wing loading: (N/m^2)');
% disp(WSst)
% disp('Lift-to-drag ratio');
% disp(LDst)
% disp('Range: (m)');
% disp(Rst)
% disp('MAC Reynolds number:');
% disp(Rest)
% LDwing = CLcr/(CDcr-Cd0_F)
% Atr
```

Atmosphere and Performance Input Section

```
%   Hybrid Projectile Performance Analysis
%   Sub-program: Atmosphere and Performance Data Input
%   By: Shanti Hamburg, 5/27/2009, for Ruggedized Stowable MAV Design Study
%.....................................................................

% Aircraft Weight [(kg m)/s^2]
W = 0.18*9.81;

% Launch velocity (m/s)
Vcr = 28;

% disp('The design cruise velocity is: (m/s)');
% disp(Vcr)

% Launch Altitude (m)
Hl = 193.8;

% Range to opening point (m)
Ropen = 181.2;

% Speed of Sound (m/s)
a = 340;
% Air Density (kg/m^3)
rho = 1.225;
% Air Viscosity [kg/(m s)]
mu = 1.7894*10^-5;

% Cruise Mach number
Mi = Vcr/a;
```

Main Wing Input Section

```
%   Hybrid Projectile Performance Analysis
%   Sub-program: Main Wing Data Input & geometry calculation
%   By: Shanti Hamburg, 5/27/2009, for Ruggedized Stowable MAV Design Study
%.....................................................................

% Wing loading (N/m^2)
%WS = 200;

% Aspect Ratio
%AR_M = 2.5;

% Center of gravity, distance forward of wing Xac as a ratio of mean
% aerodynamic chord
CbarCG = .4;

% Leading edge sweep angle (deg)
GLE_M = 0;

% Taper ratio
LA_M = 1;

% Root Chord Leading Edge Location (m)
%Xcr_M = .05;

% Chord location of maximum airfoil thickness (decimal of chord length)
Xtc_M = 0.4;

% Maximum airfoil thickness to chord ratio
TC_M = 0.1;

% Zero lift angle of attack (deg)
A0L_M = -3;

%%%%%%%%% END MAIN WING INPUT DATA
%%%%%%%%%%%%%%%%%%%%%%%%%%%%%%%%%%%%%%%%%%%%%%%%%%%%%%%%%%%%%%%%%%%%%%%%

% Wing area (m^2)
S_M = W/WS;

% Wingspan (m)
b_M = (S_M*AR_M)^0.5;

% Root chord (m)
cr_M = 2*b_M/(AR_M*(1+LA_M));

% Tip chord length (m)
ct_M = LA_M*cr_M;

% Mean aerodynamic chord (m)
```

```
cbar_M = 2/3*cr_M*(1+LA_M+LA_M^2)/(1+LA_M);

% Mean aerodynamic chord span location (m)
ybar_M = b_M/6*(1+2*LA_M)/(1+LA_M);

% Xac location (m)
%XAC_M = Xcr_M+ybar_M*tan(GLE_M*pi/180)+0.25*cbar_M;

% Quarter chord sweep angle (deg)
G25c_M = 180/pi*atan(tan(GLE_M*pi/180)-0.25*cr_M/b_M*(1-LA_M));

% Maximum thickness sweep angle (deg)
Gtc_M = 180/pi*atan(tan(GLE_M*pi/180)-TC_M*cr_M/b_M*(1-LA_M));
```

Horizontal Tail Input Section

```
%   Hybrid Projectile Performance Analysis
%   Sub-program: Horizontal Tail Input Data
%   By: Shanti Hamburg, 5/27/2009, for Ruggedized Stowable MAV Design Study
%.....................................................................

% Design Cm_alpha (based on main wing area and mean aerodynamic chord
% length here, final values will be corrected to fuselage frontal area and
% diameter)
CmAd = -0.5;

% Dynamic pressure ratio
N_H = 0.8;

% Downwash effect on angle of attack
DH_DA = 0.6;

% Leading edge sweep angle (deg)
GLE_H = 0;

% Aspect ratio
AR_H = AR_M - 0.5;

% Taper ratio
LA_H = 1;

% Location of tail aerodynamic center (m)
XAC_H = 0.12;

% Thickness to chord ratio
TC_H = 0.1;

% Thickness to chord location
Xtc_H = 0.3;
```

Fuselage Performance Section

```
%   Hybrid Projectile Performance Analysis
%   Sub-program: Fuselage Performance
%   By: Shanti Hamburg, 5/27/2009, for Ruggedized Stowable MAV Design Study
%.....................................................................

% Calculate fuselage pitching moment with angle of attack
CmAf = 0.2143*((Xcr_M+0.25*cr_M)/max(Lf))^2-0.0123*((Xcr_M+0.25*cr_M)/max(Lf))+0.0108;
CmAf = CmAf*(max(Df))^2*max(Lf)/(cbar_M*S_M);
```

Main Wing Performance Section

```
%   Hybrid Projectile Performance Analysis
%   Sub-program: Wing Performance
%   By: Shanti Hamburg, 5/27/2009, for Hybrid Projectile Project / Micro
%   Tube Launched UAV Design Study
%.....................................................................

% Oswald efficiency calculation
e = 0.98*(1-(max(Df)/b_M)^2);
k_M = 1/(pi*AR_M*e);

% Effective leading edge Mach number
Me = Mi*cos(GLE_M*pi/180);
B_M = (1-Me^2)^0.5;

% Lift curve slope
CLA_M = 2*pi*AR_M/(2+(4+(AR_M*B_M)^2*(1-(tan(Gtc_M*pi/180))^2/B_M^2))^0.5);

% Alpha = 0 lift coefficient
CLA0 = -CLA_M*pi/180*A0L_M;

% Design lift coefficient
CLd = W/(0.5*rho*Vcr^2*S_M);

% Maximum lift coefficient
CLM_M = -2*10^-4*(Gtc_M*pi/180)^2-7*10^-4*(Gtc_M*pi/180)+1.5;

% Wetted area
Swet_M = S_M*(1.977+0.52*TC_M);

% Form factor
F_M = (1+0.6/Xtc_M*TC_M+100*TC_M^4)*(1.34*Me^0.18*(cos(Gtc_M*pi/180))^0.28);
```

Longitudinal Stability Section

```
%   Hybrid Projectile Performance Analysis
%   Sub-program: Longitudinal Stability and Horizontal Tail Sizing
%   By: Shanti Hamburg, 5/28/2009, for Ruggedized Stowable MAV Design Study
%.....................................................................

% Effective leading edge Mach number
Me = Mi*cos(GLE_H*pi/180);
B_H = (1-Me^2)^0.5;

% Horizontal tail lift curve slope
CLA_H = 2*pi*AR_H/(2+(4+(AR_H*B_H)^2)^0.5);

% Xcg location
Xcg = 0.08;

XAC_M = Xcg+CbarCG*cbar_M;

Xcr_M = XAC_M-0.25*cbar_M-ybar_M*tan(GLE_M*pi/180);

% Calculate fuselage pitching moment with angle of attack
CmAf = 0.2143*((Xcr_M+0.25*cr_M)/max(Lf))^2-0.0123*((Xcr_M+0.25*cr_M)/max(Lf))+0.0108;
CmAf = CmAf*(max(Df))^2*max(Lf)/(cbar_M*S_M);

% Horizontal tail area
S_H = (CLA_M*(Xcg-XAC_M)/cbar_M-CmAd)/(N_H*CLA_H*DH_DA*(XAC_H-Xcg)/cbar_M);

% Pitching moment with respect to angle of attack, normalized to fuselage
% frontal area and diameter
CmAd_ref = CmAd*S_M*cbar_M/(Sref*max(Df));

%%%% HORIZONTAL TAIL GEOMETRY AND DRAG CALCULAITON %%%%%%%%%

% Horizontal tail span
b_H = (S_H*AR_H)^0.5;

% Horizontal tail root chord
cr_H = 2*b_H/(AR_H*(1+LA_H));

% Horizontal tail tip chord
ct_H = LA_H*cr_H;

% Horizontal tail mean aerodynamic chord
cbar_H = 2/3*cr_H*(1+LA_H+LA_H^2)/(1+LA_H);

% Mean aerodynamic chord span location
ybar_H = b_H/6*(1+2*LA_H)/(1+LA_H);

% Horizontal tail Oswald efficiency factor
k_H = 0.98*(1-(max(Df)/b_H)^2);
k_H = 1/(pi*AR_H*k_H);
```

```
% Wetted area
Swet_H = S_H*(1.977+0.52*TC_H);

% Form factor (assumes that Xtc sweep angle = 0)
F_H = (1+0.6/Xtc_H*TC_H+100*TC_H^4)*(1.34*Me^0.18*1^0.28);
```

Hybrid Performance Calculation Section

```
%   Hybrid Projectile Performance Analysis
%   Sub-program: Hybrid Performance
%   By: Shanti Hamburg, 5/28/2009, for Ruggedized Stowable MAV Design Study
%.....................................................................

% Calculate lift-to-drag ratio throughtout flight
LDopt = 0;
for i = 5:1:100
   % Fuselage parasitic drag calculations
      % Reynolds number at each fuselage station
      Cfx = zeros(size(Lf));
      for p = 1:1:max(size(Lf))
         if p == 1
            Cfx(p) = 0;
         elseif Df(p) < max(Df)
            Cfx(p) = rho*i/mu*(Lf(p));
            Cfx(p) = 1.328/Cfx(p)^0.5*1.16;
         else
           Cfx(p) = rho*i/mu*(Lf(p));
            Cfx(p) = 1.328/Cfx(p)^0.5;
         end
      end
      % Calculate fuselage drag coefficient
      Cdo_F = 0;
      SwfT = 0;
      for p = 1:1:max(size(Lf))
         Cdo_F = F*Cfx(p)*Swf(p)+Cdo_F;
         SwfT = Swf(p)+SwfT;
      end
      Cd0_F = Cdo_F*SwfT/Sref;
      %Testing changed Cd0 to CFD value
       Cd0_F = 0.10;

   % Main wing parasitic drag calculations
      % Mean aerodynamic chord Reynolds number
      Recbar_M = rho*i/mu*cbar_M;
      % Friction coefficient
      cf_M = 1.328/Recbar_M^0.5;
      % Drag coefficient
      Cd0_M = cf_M*F_M*Swet_M/S_M;
      % Correct drag coefficient to reference area
      Cd0_M = Cd0_M*S_M/Sref;

   % Horizontal tail parasitic drag calculations
      % Mean aerodynamic chord Reynolds number
      Recbar_H = rho*i*cbar_H/mu;
      % Friction coefficient
      cf_H = 1.328/(Recbar_H)^0.5;
      % Drag coefficient
      Cd0_H = cf_H*F_H*Swet_H/S_H;
```

```
        % Correct drag coefficient to reference area
        Cd0_H = Cd0_H*S_H/Sref;

%     % Vertical tail parasitic drag calculations
%         % Mean aerodynamic chord Reynolds number
%         Recbar_V = rho*i*cbar_V/mu;
%         % Friction coefficient
%         cf_V = 1.328/(Recbar_V)^0.5;
%         % Drag coefficient
%         Cd0_V = cf_V*F_V*Swet_V/S_V;
%         % Correct drag coefficient to reference area
%         Cd0_V = Cd0_V*S_V/Sref;

    Cd0 = Cd0_F+Cd0_M+Cd0_H;%+Cd0_V;
    CL(i) = W/(0.5*rho*i^2*S_M);
    DI(i) = k_M*CL(i)^2*S_M*0.5*rho*i^2;
    DP(i) = Cd0*0.5*rho*i^2*Sref;
    V(i) = i;
    L(i) = W;
    D(i) = DP(i)+DI(i);
    CD(i) = D(i)/(Sref*0.5*rho*i^2);
    LD(i) = L(i)/D(i);
    GS(i) = atan(1/LD(i));
    Lg(i) = D(i)*sin(GS(i))+W*cos(GS(i));
    Tg(i) = W*sin(GS(i))-D(i)*cos(GS(i));
    if i > 1
        if LD(i) > LD(i-1)
            Vopt = i;
            LDopt = LD(i);
            Recbar_Mopt = Recbar_M;
            Atr = (CL(i)-CLA0)/CLA_M*180/pi;
        end
    end
    if i == Vcr
        LDcr = LD(i);
        Recbar_Mcr = Recbar_M;
        Atrcr = (CL(i)-CLA0)/CLA_M*180/pi;
        CLcr = CL(i)*S_M/Sref;
        CDcr = CD(i);
        Cd0cr = Cd0_M;
        GScr = 180/pi*atan(1/LDcr);
        Rcr = Hl/tan(GScr*pi/180);
        tcr = Rcr/(Vcr*cos(GScr*pi/180));
        Cd0Fcr = Cd0_F;
    end
end

% Optimum glideslope
GSopt = 180/pi*atan(1/LDopt);

% Maximum range
```

```
Range = Hl/tan(GSopt*pi/180)+Ropen;

% Time of flight
t = Range/(Vopt*cos(GSopt*pi/180));
```

Appendix D Fluent Configuration Details

Fluent 12.4.1 Launcher Settings		
Category	**Option**	**Setting**
Dimension	2D / 3D	As Appropriate
Options	Double Precision	YES
	Use Job Scheduler	NO
	Use Remote Linux Nodes	NO
Display Options	Display Mesh After Reading	YES
	Embed Graphics Windows	NO
	Workbench Color Scheme	YES
Processing Options	Serial	NO
	Parallel (Local Machine)	YES
	Number of Processors	4
Version	12.1.4	
Parallel Settings	Interconnects	Default
	MPI Types	Default
	Run Types	Shared on Local

Fluent 12.4.1 Solver Settings, Problem Setup, General	
Mesh	
Scale	Convert milimeter mesh *to* meters
Check	Check for grid problems
Report Quality	Check skewness < 0.9
Solver	
Type	Pressure-Based
Velocity Formulation	Absolute
Time	As Appropriate
Gravity	NO
Units	Default

Fluent 12.4.1 Solver Settings, Problem Setup, Models	
Multiphase	Off
Energy	Off
Viscous	As discussed
Radiation	Off
Heat Exchanger	Off
Species	Off
Discrete Phase	Off
Solidification & Melting	Off
Acoustics	Off

Fluent 12.4.1 Solver Settings, Problem Setup, Materials	
Fluid	Air
Solid	Aluminum

Fluent 12.4.1 Solver Settings, Problem Setup, Cell Zone Conditions	
All Cells	Fluid
Oprating Conditions	
Operating Pressure (N/m^2)	101325
Reference Pressure Location	X = -0.9
	Y = 0
	Z = 0

Fluent 12.4.1 Solver Settings, Problem Setup, Boundary Conditions	
Inlet	Velocity Inlet
Outlet	Pressure Outlet
Surface	Default Wall
Interior	Interior
Interface	Interior

Fluent 12.4.1 Solver Settings, Problem Setup, Reference Values	
Area (m^2)	0.001266
Density (kg/m^3)	1.225
Length (1)	1
Temperature (K)	288.16
Velocity (m/s)	As Appropriate
Viscosity ($kg/(m\ s)$)	1.7894×10^{-5}
Ratio of Specific Heats	1.4

Fluent 12.4.1 Solver Settings, Solution, Solution Methods	
Scheme	SIMPLE
Gradient	Green-Gauss node Based
Pressure	Second Order
All Others	Second Order Upwind

Fluent 12.4.1 Solver Settings, Solution, Solution Controls	
Under-Relaxation Factors	Default
Solution Limits	Default

Fluent 12.4.1 Solver Settings, Solution, Monitors	
Residual Monitor	
Print to Console	Yes
Plot	Yes
Convergence Criterion	None
Equations to Monitor	Continuity
	X-Velocity
	Y-Velocity
	Z-Velocity
	Turbulence Model Parameters
Drag Monitor	
Print to Console	Yes
Plot	Yes
Force Vector	(X = 1) (Y = 0) (Z = 0)
Axis Limits	X Axis (Auto Range)
	Y Axis (0.0 - 0.2)
Drag Monitor	
Print to Console	Yes
Plot	Yes
Force Vector	(X = 0) (Y = 1) (Z = 0)
Axis Limits	X Axis (Auto Range)
	Y Axis (0.0 - 0.2)

Fluent 12.4.1 Solver Settings, Solution, Solution Initialization	
Gauge Pressure (N/m^2)	0
X Velocity (m/s)	0
Y Velocity (m/s)	0
Z Velocity (m/s)	0
Turbulence Parameters	(Problem Dependent, Defaults Used)

Fluent 12.4.1 Solver Settings, Solution, Calculation Activities	
Autosave Every (Iterations)	500
When Data File Saved Save Case	If Modifified
Retain Only Most Recent Files	YES
Maximum Number of Data Files	2
File Name	As Appropriate

Fluent 12.4.1 Solver Settings, Solution, Run Calculation	
Check Case	YES
Number of Iterations	Problem Dependent
Reporting Interval	1
Profile Update Interval	1

Appendix E Curriculum Vitae

Shanti D. Hamburg

884 TREMONT ST. • MORGANTOWN, WEST VIRGINIA • 26505

(304) 290-2628 • SHAMBURG@GMAIL.COM

EDUCATION

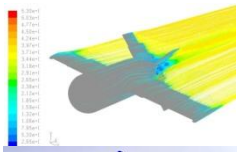

August 2007 - August 2010 — West Virginia University CEMR
MS, Aerospace Engineering — Morgantown, West Virginia

- Thesis Title: Conceptual and Preliminary Design of a Ruggedized Stowable Micro Air Vehicle

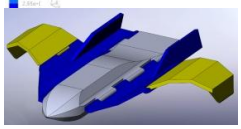

August 2002 - May 2007 — West Virginia University CEMR
BS, Aerospace Engineering, BS, Mechanical Engineering — Morgantown, West Virginia

- Grade Point Average: 3.1

RELEVANT TECHNICAL ELECTIVES

Flight Controls • Flight Simulation • Fundamentals of Computational Fluid Dynamics • Guided Missile Systems • Hybrid Vehicle Design • Mechanics of Composite Materials • Professional Engineering CAD • Structural Finite Element Analysis • Turbulent Fluid Flow • Unmanned Aerial Vehicle Design

WORK EXPERIENCE

August 2006 - August 2009 — West Virginia University CEMR
Teaching Assistant for UAV Design Team — Morgantown, West Virginia

- Team organization, grading, and project schedule management
- Program financial management, college, alumni, and corporate fund raising
- Instructing and aiding students in small aircraft design and composite manufacturing

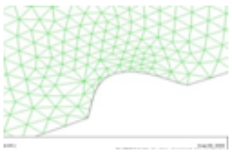

June 2008 - September 2008 — West Virginia University CEMR
Research Assistant — Morgantown, West Virginia

- Assisted in the design and execution of Fluent CFD models of dynamic roughness elements on airfoils at high angles of attack

May 2007 - June 2007 — West Virginia University CEMR
Research Assistant — Morgantown, West Virginia

- Assisted in the design and construction of a 7 *ft* span tailless flying wing with functional morphing control surfaces

August 2006 - May 2007 — West Virginia University CEMR
Co-Capitan of Challenge X Hybrid Vehicle Design Team — Morgantown, West Virginia

- Assisted with team organization and community outreach.
- Facilitated cooperation between IC engine, software controls, and hybrid system sub-teams
- Arranged component and equipment sponsorships
- Modeled hybrid system components and assemblies in Pro/Engineer

SHANTI D. HAMBURG

WORK EXPERIENCE (CONTINUED)

October 2005 - January 2006 — West Virginia University CEMR
Research Assistant — Morgantown, West Virginia

- Developed structure and built wind tunnel models
- Studied the performance of small scale, low aspect ratio ground effect aircraft for personal use

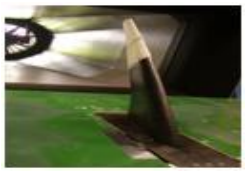

March 2005 - May 2005 — West Virginia University CEMR
Research Assistant — Morgantown, West Virginia

- Constructed wind tunnel models
- Studied the benefits of an active aeroelastic (morphing) control system compared to a conventional flapped system as applied to a Horten-type tailless flying wing

December 2002 - January 2003 — Snowshoe Ski Resort
Ski Instructor — Snowshoe, West Virginia

- Taught three to twelve year old children the basic techniques and safety measures involved with the sport of skiing
- Gained interpersonal skills in instruction and customer relations

EXTRACURICCULAR ACTIVITIES

- Team Leader, WVU Unmanned Aerial Vehicle Design Team, August 2005 - May 2006
- Co-Capitan of WVU Challenge X diesel-electric hybrid vehicle design & construction team, August 2006 - May 2007
- Secretary and Public Relations Officer for WVU American Institute of Aeronautics and Astronautics student chapter, August 2004 - May 2007
- Member, WVU Habitat for Humanity student chapter, January 2004 - December 2006
- Member, WVU Unmanned Aerial Vehicle Design Team, August 2003 - May 2005

RELEVANT SKILLS

- Experience with the Fluent CFD Package
- Experience with Missile DATCOM semi-empirical projectile analysis code
- Experience with basic composite mold and component fabrication
- Experience with basic operation of D-Six and FDC flight simulator packages
- Experience with MATLAB and Simulink mathematics and control packages
- Experience with ANSYS structural analysis
- Experience with Pro/Engineer and SolidWorks solid modeling packages
- Experience with rapid 3D printer and laser cutter rapid prototyping equipment
- Experience with computer system construction, networking, and troubleshooting
- Experience with all standard digital office applications

REFERENCES

Provided upon request

John H. Hagen
Digitally signed by John H. Hagen
DN: cn=John H. Hagen, o=West Virginia University Libraries, ou=Acquisitions Department, email=John.Hagen@mail.wvu.edu, c=US
Date: 2010.07.23 16:47:41 -04'00'